University College London

Department of Physics and Astronomy

Doctoral Thesis

Electronic coupling calculations for modelling charge transport in organic semiconductors

Author:
Fruzsina Gajdos

Supervisor:
Prof. Jochen Blumberger

A thesis submitted in fulfillment of the requirements

for the degree of Doctor of Philosophy

from

University College London

September, 2016

Declaration of Authenticity

I, Fruzsina Gajdos, confirm that the work presented in this thesis is my own. Where information has been derived from other sources, I confirm that this has been properly indicated in the thesis.

Abstract

Charge transport in organic semiconductors (OSCs) depends on a number of molecular properties, one of which is the electronic coupling matrix element for charge transfer between the molecules forming the material. They are the off-diagonal elements of the electronic Hamiltonian in the charge-localised (or diabatic) basis. The focus of this work is on the development of a method for a fast calculation of these matrix elements for OSCs. After addressing the different methods of their calculation, I present a program to estimate the off-diagonal elements of the Hamiltonian with a fast yet accurate semi-empirical method. This model approximates the off-diagonal elements of the Hamiltonian to be proportional to the overlap between the orbitals of the molecules, which are projected onto a very small basis set. The analytical results are in a reasonable agreement with accurate *ab initio* and fragment orbital DFT calculations and the speed-up is up to six orders of magnitude compared to DFT calculations. Following on from this, the analytic overlap method was implemented in two programs for charge carrier propagation, one based on Kinetic Monte Carlo simulation of charge carrier hopping (presented here), the other on surface hopping non-adiabatic molecular dynamics. I also show that the analytic overlap method can be used to estimate non-adiabatic coupling vectors very efficiently, which is an important quantity in surface hopping simulations.

Acknowledgments

First and foremost, I would like to thank my supervisor Prof. Jochen Blumberger for his help and support. He provided guidance and encouragement throughout my project, and his resilient attitude towards prioritising his students even in busy periods was invaluable during my PhD. I am also grateful to my past and present colleagues: Dr. Adam Kubas, Dr. Marian Breuer, Jacob Spencer, Felix Hoffmann, Dr. Po-hung Wang, Dr. Varomyalin Tipmanee, Dr. Harald Oberhofer, Guido Falk von Rudorff, Karina Chan, Hui Yang, Dr. Ehesan Ali, Bastian Burger, Benjamin Rousseau, Siim Valner, Felix Hummel, Jamie Sage, Marco Montefiori, Laura Scalfi, Dr. Antoine Carof and Xiuyun Jiang for their collaboration and all the discussions which helped in progressing this project. I would also like to thank Prof. Marcus Elstner, Prof. Aurélien de la Lande, Dr. Natacha Gillet, Dr. Laura Berstis, Alexander Heck and Xiaojing Wu for their collaboration. I would also like to thank Dr. Michel Dupuis, from Pacific Northwestern National Laboratory, for his support. This work was made possible by a joint sponsorship provided by the IMPACT studentship from University College London and Pacific Northwestern National Laboratory.

I would like to thank the Materials Chemistry Consortium for providing access to high performance computing facilities: HECToR and ARCHER managed by UoE HPCx Ltd at the University of Edinburgh, Cray Inc and NAG Ltd, and funded by the Office of Science and Technology through the High End Computing Programme of EPSRC and the UCL Legion High Performance Computing Facility.

I would also like to thank my friends and family near and far for their love and support. Finally, I am grateful to Dr. Ashley Shields and Thomas Beales Ferguson who are not just brilliant friends but also helped me by commenting and proofreading this thesis.

List of publications

The work discussed here has been published in the following papers:

[1] F. Gajdos, H. Oberhofer, M. Dupuis and J. Blumberger. On the inapplicability of electron-hopping models for the organic semiconductor phenyl-C61-butyric acid methyl ester (PCBM), *Journal of Physical Chemistry Letters* **4**(6):1012-1017, 2013.

[2] F. Gajdos, S. Valner, F. Hoffmann, J. Spencer, M. Breuer, A. Kubas, M. Dupuis, and J. Blumberger. Ultrafast Estimation of Electronic Couplings for Electron Transfer between π-conjugated Organic Molecules, *Journal of Chemical Theory and Computations* **10**(10):4653-4660, 2014.

[3] A. Kubas, F. Gajdos, A. Heck, H. Oberhofer, M. Elstner and J. Blumberger. Electronic couplings for molecular charge transfer: benchmarking CDFT, FODFT and FODFTB against high-level ab initio calculations. II., *Physical Chemistry Chemical Physics* **17**(22):14342-14354, 2015.

[4] J. Spencer, F. Gajdos, and J. Blumberger. FOB-SH: Fragment orbital-based surface hopping for charge carrier transport in organic and biological molecules and materials. *The Journal of Chemical Physics* **145**(6):064102, 2016.

[5] N. Gillet, L. Berstis, X. Wu, F. Gajdos, A. Heck, A. de la Lande, J. Blumberger, and M. Elstner. Electronic Coupling Calculations for Bridge-Mediated Charge Transfer Using CDFT and Effective Hamiltonian approaches at DFT and FODFTB level. *Journal of Chemical Theory and Computations* accepted, 2016.

Contents

List of Figures

List of Tables

1 Overview

Due to their numerous favourable characteristics - for example their light weight and low fabrication costs - organic semiconductors (OSCs) are becoming an increasingly prominent part of the semiconductor industry. However, low efficiency, which partly arises from low charge mobility, means that organic devices cannot compete with their inorganic counterparts. One of the key issues in current OSC devices is that little is known about their actual charge transfer mechanism. Commonly applied theoretical methods often assume either completely delocalised band-like transport or completely localised electron hopping transport. However, both experimental and theoretical results show that neither of the models above are applicable in many cases. Furthermore, both models underestimate the role of thermal fluctuations which create dynamic disorder in these materials. Although several generic quantum models have been suggested to tackle this issue, most of them can only be solved for small systems which cannot represent disordered media. Non-adiabatic molecular dynamics provides a possible solution which omits any assumptions with respect to localisation. In order to be able to apply it in large systems, the efficient calculation of the electronic Hamiltonian matrix elements and the non-adiabatic coupling vectors is crucial.

The aim of this work is to discuss charge transport in organic semiconductors and to provide the tools to enable fast and accurate charge transport modelling. In Chapter 2, a brief summary of the role of organic semiconductors (OSCs) in industry is followed by a description of the defining characteristics and structure of OSCs. This thesis describes the limitations of different theoretical transport models with an

emphasis on the most common current techniques and analysing their applicability in Chapter 3. Firstly, the two most popular transport models in organic semiconductors, band transport and hopping, are presented. As neither of these models describes charge transport in organic semiconductors generally and satisfactorily, a possible alternative, the mixed quantum-classical molecular dynamics model, is presented. While mixed quantum classical molecular dynamics is a versatile tool, it is also pointed out that it is computationally intensive. In particular, it requires the fast and accurate calculation of electronic Hamiltonian coupling matrix elements, the overlap matrix, and non-adiabatic coupling vectors. The importance of calculating accurate electronic Hamiltonian off-diagonals is underlined. In Chapter 4, a detailed analysis of different coupling calculation methods is discussed for a wide range of organic molecules in the reduced state. To this end, a selection of coupling calculation methods of different quantum levels are compared and analysed with respect to accuracy and computational demands on a broad range of organic molecules. Finding a less computationally intensive alternative to the presented methods led to the development of a fast yet accurate method for the calculation of off-diagonal Hamiltonian elements. Chapter 5 presents the analytic overlap method and discusses theory and application, accuracy, and statistics on the computational demand which enable the application of otherwise costly mixed quantum-classical molecular dynamics on systems large enough to capture the behaviour of realistic organic semiconductors. The method is also implemented into a Monte Carlo code, which assumes hopping of localised charge carriers. Details of these calculations are presented in Chapter 6. After concluding this work in Chapter 7, further avenues of investigation are also outlined.

2 Introduction

The following chapter provides a basic introduction to the increasing prevalence of organic semiconductors in the semiconductor industry and outlines the most fundamental differences between organic and inorganic semiconducting devices. Following this, a brief summary of the most common semiconducting devices is presented along with a few recent results on promising new materials. The chapter is concluded with discussing the structure of organic semiconductors and the issues arising from it with regard to the analysis of charge transport in these materials.

2.1 Background & motivation

There is a clear demand for ever lighter and cheaper electronic devices. According to the Business Insider, between 2007 and 2015 the number of smartphones sold grew from 120 million to 1.4 billion units, the lifespan of an average phone is less than 5 years and 99% of the disposed mobile phones end up in landfill. Adjusting to consumer preferences, manufacturers are decreasing the thickness of these devices which brings new materials into scope. Organic semiconductors offer a cheaper and more versatile alternative to inorganic counterparts. They are made from fairly inexpensive materials, their production demands fewer resources than silicon counterparts, their fabrication process is simpler and linear and a high proportion of the devices are biodegradable [1].

The theoretical limit of electron mobility in organic semiconductors is less than the the typical mobilities of 1000 cm^2/Vs in pure silicon single crystals, therefore it is unlikely they will replace devices where such high mobility and a highly ordered envi-

ronment are essential. However, in recent years high mobility organic semiconductors were shown to have mobilities which are comparable to electronics grade amorphous and polycrystalline silicon (a-Si and poly-Si with typical mobilities of≈1 cm^2/Vs and ≈100 cm^2/Vs respectively). Therefore currently, organic semiconductors are regarded as an alternative to a-Si and poly-Si devices: organic field effect transistors (OFETs) which can be used in organic light emitting displays [2] and radio frequency identification (RFID) tags [3], organic light-emitting diodes (OLED)[4], and organic photovoltaic devices (OPV) [5]. OLED displays are currently used by many companies in wearable devices as they are thinner and lighter than inorganic devices. Furthermore, the active matrix display does not require background lighting as the thin film is light emitting on its own which creates a preferable black contrast and makes them more energy efficient on mostly black screenshots despite lower overall efficiency. Similarly, OFETs are also used to make large curved displays. Although organic photovoltaics are less efficient than their silicon counterparts (mobilities of ≈0.1-1 cm^2/Vs), their cheap fabrication facilitates large area production. In addition, the low cost of manufacturing also means a lower energy payback time, which makes OPVs an appealing area for research. Even though nowadays the focus has shifted towards perovskite photovoltaics, another promising cheap and efficient alternative to amorphous and polycrystalline Si devices, OPVs can compete in large area applications as they do not contain heavy metals such as Pb making them a safer option.

2.2 Comparison to Si devices

2.2.1 Manufacturing

While Si processing requires high temperatures and vacuum even with highly efficient plasma enhanced chemical vapour deposition, around 150-500 °C [6], single

crystal organic semiconductors can be fabricated at temperatures as low as 90 °C [5]. Ambient temperatures can also be used when the OSCs are produced with drop casting [7], dip casting [8] and spin casting [9]. Furthermore, devices can be produced from solution using specialised ink jet printers [10]. A great added advantage of the ambient processing temperature is that it allows OSC devices to be processed on flexible substrates [11, 12].

2.2.2 Organic semiconducting materials

The variety of available materials which can be used as organic semiconductors presents a wide range of charge mobility and band gap values. While inorganic *n*-type and *p*-type semiconductors are usually created by doping, in the organic case it is often the material itself which has a large electron affinity or a low ionisation potential [13].

p-type organic semiconductors

A wide variety of *p*-type materials are available including small molecule single crystals consisting of acenes or rubrene and polymers like poly(2,5-bis(3-hexadecylthiophen-2-yl)thieno[3,2-b]thiophene (PBTTT), poly(3-hexylthiophene-2,5-diyl (P3HT), and diketopyrrolopyrrole (DPP), all three of which are commonly used in bulk heterojunction photovoltaics [14, 15, 16]. In some materials rather high mobilities were measured: in air stable rubrene single crystals mobilities exceeding 10 cm^2/Vs were measured [17], while mobilities exceeded 40 cm^2/Vs for highly aligned meta-stable structure of 2,7-dioctyl[1]benzothieno[3,2-b][1]benzothiophene (C8-BTBT) according to Ref [13]. Polymers mostly have lower mobilities of around a few cm^2/Vs due to their partial disorder, however there is evidence for mobility values as high as 10.5 cm^2/Vs in highly ordered DPP [16].

n-type organic semiconductors

There are far fewer known *n*-type organic semiconductors than *p*-types and many *n*-type OSCs are ambipolar carrying electrons and holes equally well which leads to inefficient power usage. The mobility in *n*-type semiconductors is also generally lower. Nevertheless, there is an increasing demand for *n*-type and ambipolar organic semiconductors for OPVs. One way of creating *n*-type semiconductors is introducing electron withdrawing groups to otherwise *p*-type semiconductors like in the case of perylene-diimide, naphthalene-diimide and fluorinated rubrene. The typical electron mobility for these materials ranges between 1 to 4 cm^2/Vs, an order of magnitude smaller than what is achievable in *p*-type organic semiconductors [18]. The best performance so far has been achieved in C_{60} single crystal needles where mobilities as high as 11 cm^2/Vs were measured [13].

2.3 The structure of organic semiconductors

The principle behind the application of π-conjugated molecular systems as semiconductors is that the p orbitals of sp^2 hybridised carbon atoms form delocalised, energetically closely spaced states where the energy difference between the highest occupied level and the lowest unoccupied level is similar but slightly larger than that of inorganic semiconductor crystals [9]. Despite their higher band gap these materials behave like semiconductors when charge carriers are injected through electrodes. Although this similarity inspired the first successful experiments on OSC devices, the charge transport processes in these devices seem to be fundamentally different from those in inorganic systems.

The microstructure of small molecule organic semiconductors depends on the fabrication process and the materials used, and it ranges from amorphous to poly- and semicrystalline to single crystalline [19, 20, 21, 22]. However, all organic semiconducting materials share the common feature of being held together by weak van

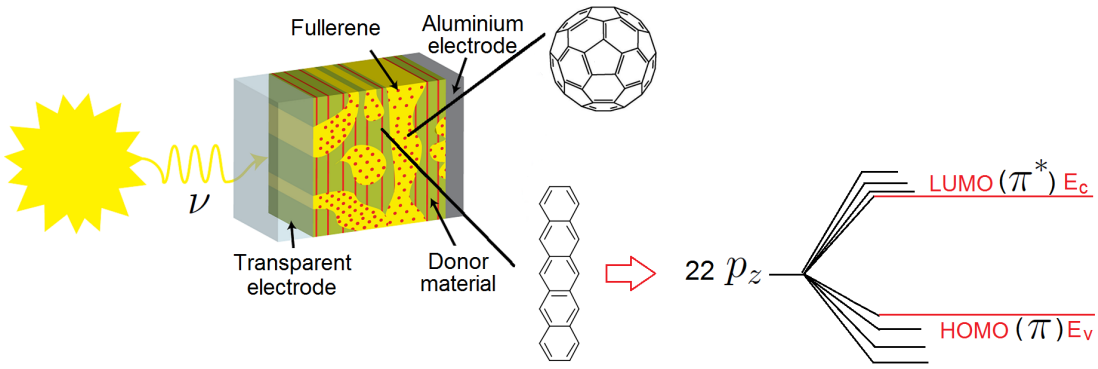

Figure 2.1: Device setup for a pentacene–C_{60} heterojunction solar cell and a schematic diagram of how the 22 p_z orbitals mix into molecular orbitals creating energetically close states around the HOMO and the LUMO creating a band structure

der Waals interaction, whereas inorganic semiconductors are fully covalent systems. This leads to two very important consequences. Firstly, the electronic coupling between the molecules is much weaker compared to the coupling between the atomic orbitals of inorganic semiconductors. Secondly, the nuclear motion has a much more prominent role than in their inorganic counterparts. The weak coupling and the strong nuclear motion leads to a very strong electron-phonon coupling: comparable to the electronic coupling between the molecules. This is not present in inorganic semiconductors where the covalent bonds between the atoms provide a rigid structure and strong coupling between the atomic orbitals. These effects are the main reason behind the lower charge carrier mobility in OSCs.

An example of a molecular OSC is C_{60}. Fullerenes are widely used acceptor materials in OFETs and OPVs because of their unique electronic structure which makes them the highest mobility n-type organic semiconductor currently known [23]. At room temperature, crystalline C_{60} forms a face-centred cubic (fcc) structure and the molecules rotate freely around their lattice sites. The rotational correlation time was measured to be around $\tau = 12$ ps [21]. Cooling below 255 K, the crystal goes through a first order phase transition and the molecules no longer rotate freely , the symmetry is lowered and the C_{60} molecules form a simple cubic (SC) crystal with 4 molecules per unit cell [21]. Below 100 K, a second-order phase transition happens

and the rotation stops [24].

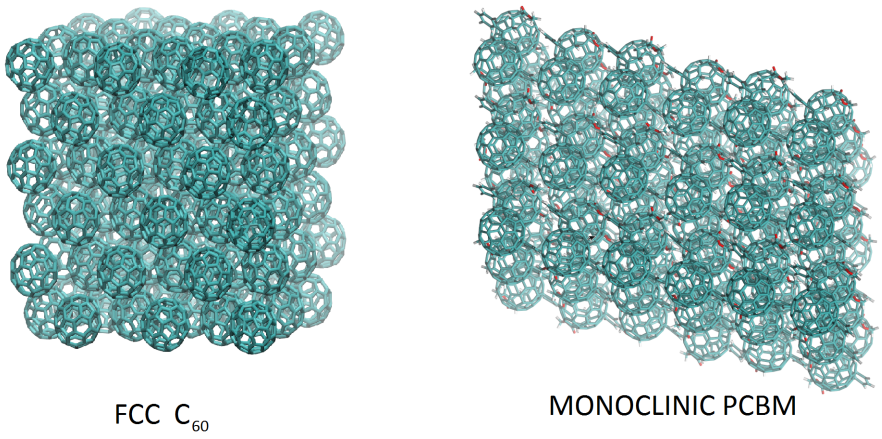

Figure 2.2: Crystal structure of C_{60} and PCBM. C_{60} crystallises in an FCC structure. PCBM has many different crystalline phases, here a monoclinic phase is shown. As it can be seen, the packing is different from C_{60}.

Although C_{60} has many favourable characteristics [23], there are limited ways of processing them and for this reason they are often functionalised by adding polar groups. For example, phenyl-C_{61} butyric acid methyl ester (PCBM) is a derivative of C_{60} with an added polar side chain (Fig 2.3). This makes the fullerenes soluble in chlorobenzene and dichlorobenzene which facilitates their solvent casting [5, 7]. Although these functional groups do not affect the electronic structure of the molecules dramatically, as can be seen in Fig. 2.3, they lead to a significant change in the crystal packing (Fig. 2.2). For example, PCBM is known to form triclinic [5], monoclinic [5, 7] and hexagonal [25] structures. Although currently there is no known experimental data on mobility in single crystal PCBM it is expected to be similar to that of C_{60} but that is dependent on the stacking in the given crystal structure.

It is also interesting to consider how the side chains change the dynamics in the crystal and affect the dynamic disorder. As free rotations of the C_{60} cages are prevented by the polar groups, this is expected to change the nature of the thermal fluctuations and to have an effect on the charge transport [7].

Due to their numerous interesting characteristics and popularity, fullerenes will play an important role in this piece of work.

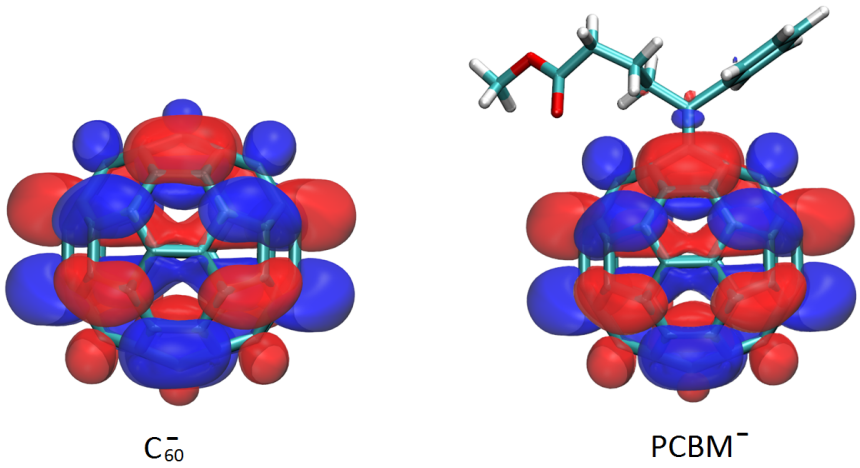

Figure 2.3: The highest occupied molecular orbital of C_{60}^- and $PCBM^-$. The orbital shapes are not very different: the side chain of the PCBM only causes a slight perturbation in the orbital shape.

2.4 Challenges of organic semiconductors

As mentioned, despite their positive characteristics, organic compounds cannot completely overtake the semiconductor market due to their significantly lower efficiency in which low electron mobility is a major factor [26]. Whilst the charge mobility in inorganic semiconductors is in the order of 1000 cm^2/Vs, the upper limit in organic molecular crystals is two orders of magnitude smaller even in highly purified single crystalline samples. In fact, even the basic question of whether the charge carriers exhibit a wavelike behaviour, delocalised over the sample, or whether they are localised on one (or a few) molecules and maintain their particle behaviour during the transport, remains unanswered. The particle/wave like behaviour of the excess charge affects the charge recombination mechanisms in these materials which is one of the main sources of lower efficiency in organic semiconducting devices. Experimental evidence seems to support both theories. In high purity samples experimental results show that at low temperatures the electron mobility decreases with increasing temperature which suggests non-thermally-activated charge transport. The Hall-effect [20, 27] has also been measured in organic crystals. These both suggest wave

like behaviour. On the other hand, electron spin resonance (ESR) results show localised charge carriers in similar samples [28]. These controversial results call into question the applicability of models that make assumptions on the localisation or delocalisation of the charge carrier.

In order to improve the efficiency of OSCs, it is crucial to have a general understanding of charge transport which is applicable to a wide range of materials, regardless of whether the system is crystalline, polycrystalline or amorphous [26, 29, 30, 31]. Such a model should be able to account for both the static and dynamic disorder introduced by the relatively weak interaction and should also be feasible in large system sizes in order to get a better description of realistic OSC materials.

3 Charge transport models in organic semiconductors

In the previous chapter, it was briefly mentioned that the major challenges of simulating electron transport in organic semiconductors arise from the many non-negligible energy terms which have to be included in the Hamiltonian. Furthermore, accurate modelling requires large system sizes in order to fully understand the structural characteristics. In this chapter, several approximations are presented for assessing the charge transport in organic semiconductors. First, a model Hamiltonian is introduced for organic semiconductors. Then, the two most common charge transport approximation methods are discussed: band transport, and small polaron hopping. Finally, other more general but computationally intensive methods such as non-local electron-phonon coupling and non-adiabatic molecular dynamics are presented, which can offer a method for tackling the issues of charge transport in organic semiconductors where the two previous methods fail.

3.1 The Holstein Hamiltonian

A commonly used model Hamiltonian is the Holstein Hamiltonian [32]. It describes the polaron—the combination of an excess charge and the associated deformation—and is used by Troisi [33], Brédas [34], and Sirringhaus [35]. It can be written in the following form

$$H = H_{\text{el}-\text{el}} + H_{\text{nuc}-\text{nuc}} + H_{\text{el}-\text{nuc}}. \tag{3.1}$$

The operator H consists of an electronic part $H_{\mathrm{el-el}}$, a nuclear part $H_{\mathrm{nuc-nuc}}$, and the term that expresses the relationship between them, including the electron phonon coupling $H_{\mathrm{el-nuc}}$. The weak intermolecular interaction between the molecules means that the couplings (0.1 to 100 meV) are most of the time an order of magnitude smaller than the energy gap between the orbitals (1 eV). As a consequence, the orbitals of the individual molecules are only slightly perturbed in the condensed phase. This means that the wavefunction of a charge carrier can be well represented by linear combinations of the orbitals of the isolated diabatic states. Consequently, the electronic part of the Hamiltonian can be approximated by localised diabatic states on site i, denoted as $|i\rangle$. Therefore, the electronic Hamiltonian may be written in the form of

$$H_{\mathrm{el-el}} = \sum_i H_i |i\rangle\langle i| + \sum_j H_{ij} |i\rangle\langle j| \tag{3.2}$$

where H_i is the on-site energy, and H_{ij} is the electronic coupling between the states localised on the different sites. Now, as mentioned before, the coupling between the sites is rather weak and even the second nearest neighbour term is often orders of magnitude smaller than the nearest neighbour contribution. Thus, usually only the nearest neighbour terms are kept. It is also worth mentioning that the large difference between the orbital energy gap and the coupling is often used as a reason to use approximate fragment orbital methods so that the diabatic state is replaced by highest occupied molecular orbitals (HOMOs) of the molecules (which are also called as singly occupied molecular orbitals, or SOMOs, in case of open-shell systems). The nuclear motion is approximated as a sum of harmonic oscillators:

$$H_{\mathrm{nuc-nuc}} = \sum_{\mathbf{k},i} \frac{\hbar\Omega_{\mathbf{k},i}}{2} (a^+_{\mathbf{k},i} a_{\mathbf{k},i} + \frac{1}{2}), \tag{3.3}$$

where $a^+_{\mathbf{k},i}$ and $a_{\mathbf{k},i}$ are the creation and annihilation operators of the phonon described by the angular frequency $\Omega_{\mathbf{k},i}$ and $\mathbf{k}$ is the wave vector. The expression for $H_{\mathrm{nuc-nuc}}$ can be simplified like in the case of the works by Coropceanu *et al.* [36]

where only the dominant normal mode is chosen. In this case, the nuclear motion is to be described with a single classical harmonic oscillator

$$H_{\mathrm{nuc-nuc}} = \sum_i \frac{\hbar\Omega}{2}(p_i^2 + q_i^2), \tag{3.4}$$

where q_i is the nuclear deformation along the chosen phonon mode, p_i is the associated canonical momentum and Ω is the frequency of the dominant optical phonon. The third term is the electron-phonon coupling value. In this semi-classical interpretation the electron phonon coupling is expected to be weak and thus only the linear component is kept. The expression is as below

$$H_{\mathrm{el-nuc}} = g\hbar\Omega q_i |i\rangle\langle i| \tag{3.5}$$

where g is the coupling strength of the local electron-phonon coupling [37].

3.2 Band transport

In the low-temperature limit ($h\Omega >> k\mathrm{B}T$), the nuclear motion is negligible and the charge carrier and associated deformation remain delocalised forming the polaronic band [32]. Assuming that the electron phonon coupling is negligible, this expression can be simplified by thermally averaging over the different H_{ij} values in the form of

$$H_{\mathrm{band}} = \sum_i H'_i |i\rangle\langle i| + H'_{ij} |i\rangle\langle j|, \tag{3.6}$$

where $H'_{ij} = H_{ij} \exp\left(-\frac{1}{2}g^2\left(N_\Omega + \frac{1}{2}\right)\right)$ and the term N_Ω has a non-trivial temperature dependence

$$N_\Omega = \left(\exp\left(\frac{\hbar\Omega}{k_{\mathrm{B}}T}\right) - 1\right)^{-1} \tag{3.7}$$

increasing as the temperature increases [32]. For this Hamiltonian, the Boltzmann equation can be used to acquire mobility values [22].

The mobility can be calculated as

$$\mu = \frac{-et_s}{m^*} \tag{3.8}$$

where the relaxation time between collisions t_s can be calculated from the auto-correlation function of the velocity of the electrons obtained from the first velocity moment of the distribution function [38].

$$\langle v(0)v(t)\rangle = \langle v^2\rangle \exp\left(-\frac{t}{t_s}\right) \tag{3.9}$$

The effective mass tensor can be calculated as

$$m^{*-1}_{lm} = \frac{1}{\hbar^2}\frac{\partial^2 E}{\partial k_l \partial k_m} \tag{3.10}$$

where k_l and k_m are reciprocal space vector components and E is the full energy expression according to Eq. (3.6). Using the example of a homogeneous one-dimensional chain by Troisi [26], the effective mass tensor simplifies to the following scalar:

$$m^* = \frac{\hbar^2}{2a^2|H_{ij}|} \tag{3.11}$$

where a is the lattice constant in the one dimensional chain. As expected, the higher the coupling, the lower the effective mass. Strong couplings imply nearly deloclised states with large mobilities and therefore small effective mass values. One can see that in Eq. (3.6), $H'_{ij} < H_{ij}$ for $T > 0$ K, therefore the effective mass increases as the temperature increases causing the mobilities calculated with the Boltzmann-equation to decrease.

As predicted above, high mobility values were observed in highly purified naphthalene and perylene samples [39] and Hall-effect was measured in rubrene [27]. Furthermore, in the low temperature limit the temperature dependence becomes

$\mu \propto T^{-n}$, similar to inorganic semiconductors. However, as the temperature increases the nuclear motion becomes more significant and band theory breaks down as the electron-phonon coupling becomes more relevant. Indeed localisation has been observed in ESR [28] and CMS [40] spectroscopy. This observed localisation prompted the idea of using other transport models, such as activated hopping.

3.3 Transport via activated hopping

In the limit of high-temperature and small electronic coupling, the charge carrier and the associated deformation become localised on one molecule and form a small polaron which remains localised during the transport. This limit can be treated with localised charge hopping theory which has been used to assess the rate of oxidation and reduction in solutions [41]. In this case, the electron is localised on one site. In order to move, the electron has to overcome an energy barrier which is an infrequent Markovian process and can be treated using transition state theory with semi-classical reaction rates [42, 43]. The localised transport can be explained by showing the potential energy surfaces of the transport presented in Fig. 3.1.

When H_{ab} is small compared to the reorganisation energy λ of the molecules and the surroundings, the transition occurs on the diabatic surface (Panel 1 Fig. 3.1). This falls under the Marcus theory which has been used to describe charge transport in solutions [42]. The rate of the transition is given by

$$k_{\mathrm{na}} = \frac{2\pi}{\hbar}|H_{ab}|^2 \frac{1}{\sqrt{4\pi\lambda k_{\mathrm{B}}T}} \exp\left(-\frac{(\Delta A + \lambda)^2}{4\lambda k_{\mathrm{B}}T}\right) \tag{3.12}$$

where $\Delta A = A_a - A_b$ is the potential energy difference between the two energy minima on the diabatic surfaces. For large electron couplings, electron transfer occurs on the adiabatic potential energy surfaces (shown in red in Fig. 3.1). Here, the electronic Hamiltonian is diagonalised and the energy barrier is lowered by the

coupling value (Panel 2 Fig. 3.1) [44]. The transition rate is calculated as

$$k_{\mathrm{ad}} = \frac{\omega}{2\pi} \exp\left(-\left(\frac{\Delta A^{\dagger}}{k_{\mathrm{B}}T}\right)\right). \tag{3.13}$$

Here, $\Delta E^{\dagger}$ is the activation energy expressed in Eq. (3.14).

$$\Delta A^{\dagger} \approx (\Delta A^{\ddagger} - \Delta) \tag{3.14}$$

where $\Delta E^{\ddagger}$ is the non-adiabatic activation energy and Δ is the adiabatic correction

$$\Delta A^{\ddagger} = \frac{(\Delta A + \lambda)^2}{4\lambda} \tag{3.15a}$$

$$\Delta = |H_{ab}| + \frac{\lambda + \Delta A}{2} + \sqrt{\frac{(\lambda + \Delta A)^2}{4} + |H_{ab}|^2} \tag{3.15b}$$

The adiabatic correction Δ assumes that the position of the minimum of the adiabatic surface coincides with the minimum of the diabatic surface, which is not exactly the case for large H_{ab}. For this reason Eq. (3.14) predicts a vanishing activation energy ($\Delta A^{\dagger} = 0$) at $H_{ab} = 3/8\ \lambda$ instead of the exact relation $H_{ab} = 1/2\ \lambda$ for $\Delta E = 0$. Unfortunately, this is not an exact analytic expression for $\Delta A^{\dagger}$ for general ΔA, yet Eq. (3.14) gives a good enough approximation in the majority of cases.

A general expression for the transfer rate that can provide an interpolation between the diabatic and the adiabatic regime is given by Oberhofer *et al.* [45] as

$$k = \kappa_{el} \nu_n \Gamma \exp(-(1/k_{\mathrm{B}}T)\Delta A^{\dagger}) \tag{3.16}$$

where is the nuclear tunnelling factor is $\Gamma = 1$, $\nu_n = \omega/2\pi$ is the nuclear frequency along the reaction coordinate and κ_{el} is the thermally averaged electronic transmission coefficient [45]. κ_{el} determines the adiabaticity of the charge transfer:

$$\kappa_{el} = \frac{2P_{LZ}}{1 + P_{LZ}}. \tag{3.17}$$

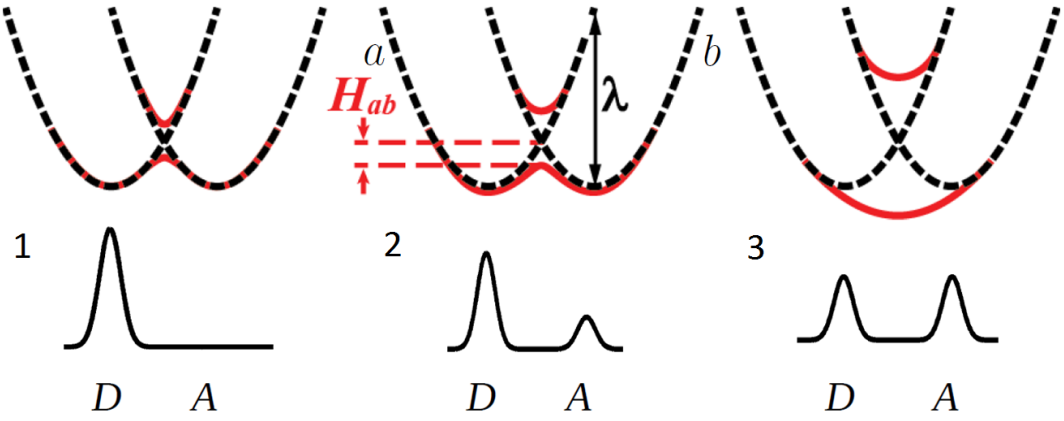

Figure 3.1: Electronic coupling values and their effect on the energy barrier of the localised electronic transport. The dashed line represents the diabatic surface representing an electronic state which remains unchanged throughout the deformation of the ionic structure. The continuous red line is the adiabatic surface representing an electronic state which obeys strictly the Born-Oppenheimer approximation and the electronic structure follows the ionic movements continuously and instantaneously. The reorganisation energy is marked on the plot with λ. Panel 1 shows the small-coupling case where the wavefunction is completely localised and transition happens on the diabatic surface. Panel 2 shows a larger coupling where the wavefunction is more spread out and the transition happens on the adiabatic surface. Panel 3 shows the case when the rate equation model is beyond applicability. The figures underneath illustrate schematically the density for each state.

Here P_{LZ} is the Landau–Zeener probability [44]

$$P_{LZ} = 1 - e^{-2\pi\gamma} \tag{3.18}$$

and

$$2\pi\gamma = \frac{\pi^{2/3}|H_{ab}|^2}{h\nu_n\sqrt{\lambda k_{\mathrm{B}}T}}. \tag{3.19}$$

If $2\pi\gamma >> 1$ the expression for k according to Eq. (3.16) takes the form of the adiabatic rate equation Eq. (3.13). In the other limit, Δ is negligible and therefore can be omitted and the expression Eq. (3.16) can be expanded as a function of H_{ab} into a Taylor-series around $H_{ab} = 0$. Truncating it at the first order term, the obtained rate expression is proportional to $|H_{ab}|^2$ and the non-adiabatic rate equation Eq. (3.12) can be retrieved [42, 44].

In the hopping regime, the electron transport can be modelled using the master equation or kinetic Monte Carlo (KMC) approach [30, 46] with rates obtained

according to Eqs. (3.13), (3.12) or (3.16).

Indeed, charge carrier localisation was observed in organic semiconductors with CMS [40] and ESR spectra [28]. However, it is often the case that the deformation and the dipole reorganisation of the surroundings cannot localise the charge on a single molecule and the model becomes invalid [35]. Troisi also points out that localised charge carrier transport certainly cannot be the case in high mobility organic semiconductors. If rate equations are used, the maximum possible mobility is limited by the largest possible rate which is permitted by the hopping theory. Such a rate still requires a positive energy barrier between the localised states. However, the maximum rate in a system with known reorganisation energy is limited. Therefore, rates which would be needed in high mobility semiconductors violate the localised transport theory [47].

3.4 Applicability of transport models

Most π-conjugated organic molecules have small reorganisation energies; for example fullerenes have less than 0.2 eV. Reorganisation energies in solids, in general, are less significant than in solutions where the dipoles around charge transfer system have to reorganise. In solids, the relatively rigid environment means a smaller outer sphere contribution. The inner sphere contributions are usually slightly larger but generally below 1 meV as charge transport does not mean significant change in the nuclear arrangement of the charge transfer system. Electronic couplings between the molecules, while on average an order of magnitude smaller, can become just as large as the reorganisation energy for thermally accessible configurations [35, 48, 49]. Hence, the situation is similar to case 3 shown in Figure 3.1: in many thermally accessible configurations a localised charge carrier will not form. On the other hand, band transport is not expected to give a satisfactory description either, because this theory does not adequately account for the strong thermal nuclear motions that cou-

ple to the charge transport as, even at room temperature, the coupling variance is comparable to the mean coupling and there is a certain level of localisation. Sirringhaus *et al.* [35] describes the electron motion as percolation motion. Here, two models are discussed which do not assume complete localisation or delocalisation.

3.4.1 Non-local electron phonon coupling

The Holstein Hamiltonian can be expanded with the non-local electron phonon coupling component [36, 50]. This model is called the Holstein-Peierls Hamiltonian and it has been used by multiple groups [26, 51, 52]. In the aforementioned one dimensional chain it takes the form of

$$H_{i,i+1}(t) = G\hbar\omega(q_i - q_{i+1})(|i\rangle\langle i+1| + |i+1\rangle\langle i|) \tag{3.20}$$

where G is the strength of the non-local electron-phonon coupling representing the role of nuclear motion in the electronic energy terms.

If the non-local electron phonon coupling is negligible the Holstein Hamiltonian can be reobtained and this Hamiltonian gives back the band transport and hopping models in special cases, demonstrated above. However, when the non-local electron-phonon coupling is included the observed effects in organic semiconductors can be described better. Troisi provides a system where rather than trying to identify the non-local electron-phonon coupling factor G, the electron coupling was divided into time-independent and time-dependent parts. In this model, the time-independent part was described as the average of the electronic coupling values and the time-dependent part as the fluctuation observed during a molecular dynamics simulations in rubrene [26]. This showed similar trends to observed behaviour where the charge carrier, despite being initialised on a single site, eventually spreads in the system and

the electron mobility reduces with increasing temperature. The numerical evaluation of the time dependency of the coupling has the great advantage that the expression is not simplified to having a single optical phonon mode governing the charge transport but includes the non-negligible effects of the acoustic modes as well. These acoustic modes cause a change in the intermolecular distance which modulates the electronic coupling. Realising the importance of this, also offers another possible method to discuss the charge transport in organic semiconductors.

3.4.2 Mixed quantum-classical molecular dynamics

First-principles methods do not require assumptions of electronic wavefunction localisation and it is not necessary to identify a single harmonic nuclear frequency. The electronic Hamiltonian in mixed quantum-classical molecular dynamics is similar to the previously discussed $H_{\mathrm{el-el}}$ in Eq.(3.2). However, the values of the electronic Hamiltonian depend on the nuclear coordinates and thus become time dependent through the dynamics. Treating the nuclei classically, the time-dependent Schrödinger for the excess charge in the system reads:

$$i\hbar\frac{\partial}{\partial t}|\Psi\rangle = \hat{H}|\Psi\rangle \tag{3.21}$$

The charge carrier wavefunction $|\Psi\rangle$ is expanded in a set of basis functions

$$|\Psi\rangle = \sum_i c_i|\phi_i\rangle \tag{3.22}$$

where $c_i = c_i(t)$ are time-dependent expansion coefficients. As discussed previously, the molecular orbitals of the isolated molecules are slightly perturbed by the condensed phase, therefore localised diabatic states provide a good basis set for this problem. Hence, the basis functions depend on time due to the molecular motion

$\phi = \phi(\mathbf{R}(t))$. By inserting the expression (3.22) into Eq. (3.21) we get

$$i\hbar \frac{\mathrm{d}c_k}{\mathrm{d}t} = \sum_j \left(H_{kj} - \langle \phi_k | \frac{\mathrm{d}\phi_j}{\mathrm{d}t} \rangle \right) c_j \tag{3.23}$$

Eq. (3.23) can be solved numerically using, for example, the Runge–Kutta algorithm from which the $c(t)$ values can be obtained.

Adiabatic dynamics (Born–Oppenheimer or Carr–Parinello) are often used and are standardly available in several quantum chemistry program packages. However, it uses the assumption that the electronic system remains in the same adiabatic electronic state throughout the dynamics. As mentioned in the previous section, this is not necessarily true in organic semiconductors as some coupling values are small. Therefore, the energy gap between different electronic surfaces is small and transitions between electronic states need to be incorporated during the dynamics. Hence, a non-adiabatic molecular dynamics (NAMD) treatment is required.

The simplest NAMD method is to use the classical path method, where the electron dynamics is done on a previously computed molecular dynamics trajectory. In this approach, any possible effect of the electron dynamics on the nuclear motion is completely ignored. However, omitting the feedback from the electron dynamics to the nuclear structure dissociates the charge from the associated deformation and give erroneous results. For example, in crystalline semiconductors, the classical path method may overdelocalise the charge, preventing the formation of a small polaron in special cases. Therefore, different approaches had to be considered [53].

In the Ehrenfest method, multiple potential energy surfaces are taken into account. The molecular dynamics happens on a mean field surface that is an average of these potential energy surfaces with weights proportional to the square of the expansion coefficient for each electronic state. However, if the potential energy surfaces refer to very different physical processes the dynamics can fail as the mean field can represent an unphysical state [54].

Surface hopping avoids the problem of mean field approximation. Similarly to the previous case, there are multiple potential energy surfaces. The nuclear subsystem is evolving on only one of these potential energy surfaces at a time and the forces calculated from the charge propagation are fed back to the system. At each molecular time step, it is checked whether the system has undergone a state switch, in which case the molecular dynamics continues on another potential energy surface. In this case, it is a key issue to define such potential surfaces that can adequately describe the charge carrier transport [55]. While the risk of unphysical states is mitigated in surface hopping, unlike in the Ehrenfest method, the energy is not automatically conserved and the energy has to be rescaled at each surface hopping event.

3.5 Conclusion of charge transport methods and thesis statement

Several charge transport model have been presented here which are used to model charge transport in organic semiconductors. The band transport and the localised charge transport methods offer a reasonably simple solution which can be tackled with the calculation of only a few computationally intensive values, albeit they use assumptions of localisation and delocalisation which often break down in realistic systems due to dynamic disorder. The non-local electron-phonon coupling model and non-adiabatic molecular dynamics do not use any assumptions of localisation or delocalisation, hence they appear to be more suitable for discussing organic semiconductors at room temperature. Non-adiabatic molecular dynamics has the added benefit that the dynamic and static disorder can be both represented in the diagonal and off-diagonal elements of the Hamiltonian, hence it is expected to be general and applicable even in the special case of fullerenes, where the free rotation of the molecules at room temperature strongly modulates the coupling, and can be applied to any general organic semiconducting material. However, using non-adiabatic dy-

namic requires the fast evaluation of numerous quantum mechanical properties in large systems which makes it a computationally intensive method.

Taking the example of fcc C_{60} where the unit cell contains 4 molecules and taking a supercell of $3\times3\times3$ for a 1 ns trajectory can give some insight about the behaviour of the system. Such simulation requires a time resolution finer than the largest frequency in the system. For example, in the case of describing a C=C stretch this has to be around 1 fs. Assuming that only nearest neighbours are included there are 108 diagonal and $(12\times108)/2$ non-zero off-diagonal elements in the Hamiltonian and the same number in the overlap matrix elements. Furthermore, the non-adiabatic coupling vector also needs to be calculated for 10^6 snapshots. Whilst the diagonals of the Hamiltonians can be approximated using a classical approximation by taking the vertical ionisation energy in the MD, this is not possible for the electronic coupling matrix elements, the non-adiabatic coupling vector, and the overlap.

The aim of this project is to provide a toolkit for supporting charge transport models in π-conjugated systems which scales favourably with system size. To this end, the focus is on the off-diagonal elements of the Hamiltonian, the overlap matrix, and the non-adiabatic coupling vectors calculated in an appropriately chosen basis set. In Chapter 5 of this thesis, I will present an efficient method that I have developed for this purpose. In the following chapter I will present explicit electronic structure methods for the calculation of electronic coupling that will be used for calibration of the more cost-effective calculations presented in Chapter 5.

4 Benchmark study on the accuracy of coupling calculation methods

As was mentioned in Chapters 2 and 3, the accurate calculation of electronic couplings has an important role in the understanding of charge transport in organic semiconductors, even more so when the electronic coupling matrix elements are of a similar order of magnitude as the reorganisation energy. Unlike the diagonal elements of the Hamiltonian, they cannot be approximated with classical models and their calculation is often time consuming and therefore size limiting.

Motivated by building accurate transport models, this chapter focuses on the comparative analysis of different coupling calculation methods which were calculated within our group and in collaboration with other groups [56]. The results are compared to reference values obtained using high level *ab initio* methods in combination with generalised Mulliken–Hush theory (GMHT). The electronic coupling values are calculated with density functional theory methods: constrained density functional theory (CDFT), and fragment orbital density functional theory (FODFT). Furthermore, approximate fragment orbital density functional tight binding (FODFTB) is also compared to these methods.

There are several other models which are not presented here. Time dependent density functional theory can be used to calculate electronic coupling values. Difley *et al* argues that while for the exact density functional the ground state is adiabatic commonly used approximate functionals often produce diabatic states which can be

tested with attachment/detachment analysis [57]. Other methods such as Zerner's intermediate neglect of differential overlaps (ZINDO) method has also be used to calculate the coupling values [46].

The chapter starts with a brief introduction of the underlying theory of each method and their limitations. Then, a set of systems are introduced which aim to capture the basic characteristics of organic semiconductors for which the coupling values are calculated with the listed coupling calculation methods.

The results presented here offer an insight into the varying accuracy and computational demands of the different methods. The calculations were performed on organic molecules with increasing numbers of heavy atoms, which enabled an analysis of the feasibility of the different techniques. Alongside the size limitations, the effect of heteroatoms and the influence of the orientation of the molecules on the coupling is also tested. The chapter is concluded with the comparison of the computational demands of the methods presented.

4.1 Introduction to electronic coupling calculation methods

It is worth emphasising the difference between adiabatic and diabatic surfaces which both have a key role in electronic transitions. Adiabatic states and potential energy surfaces are created by rigorous application of the Born-Oppenheimer approximation thus the electronic structure is always smooth and the adiabatic states diagnolise the Hamiltonian matrix. Diabatic states are localised, chemically intuitive electronic states which play an important role in charge transport theory. In contrast to the adiabatic states, in the diabatic case the electronic density does not follow continuously the reaction coordinate of the charge transition. Instead, they preserve their electronic character uniformly as the nuclear structure changes along the reaction

coordinate: a covalent system remains covalent and an ionic system remains ionic throughout. In the non-adiabatic case the charge transition happens suddenly when the diabatic states get close to one another, for example when the adiabats show an avoided crossing (See Panel A Fig 3.1). The diabats do not diagonalise the Hamiltonian. The electronic coupling matrix elements can be calculated by taking the diabatic wavefunctions ψ_a^{diab} and ψ_b^{diab} at the crossing of state a and state b and calculating

$$H_{ab} = \langle \psi_a^{\text{diab}} | H | \psi_b^{\text{diab}} \rangle. \tag{4.1}$$

There are various ways to construct diabats. Van Voorhis *et al.* [58] distinguishes between deductive and constructive methods for obtaining ψ_a^{diab} and ψ_b^{diab}. Deductive methods use adiabats to construct diabatic states.

4.1.1 Generalised Mulliken–Hush theory

Generalised Mulliken–Hush theory (GMHT) is one of the deductive ways for obtaining diabatic states using only adiabatic quantities to describe the adiabatic states [59, 60, 61]. A generalised derivation can be seen in the works of Creutz *et al* [62]. The method for the two-state system assumes an orthonormal system in which the adiabatic wavefunctions are denoted as ψ_1 and ψ_2 ground state and first excited state respectively. The diabatic localised states are denoted as ϕ_a, for the initial state, and ϕ_b, for the final state. The adiabatic states can be described as a linear combination of the diabatic states

$$\psi_1 = c_a \phi_a + c_b \phi_b \tag{4.2a}$$

$$\psi_2 = -c_b \phi_a + c_a \phi_b \tag{4.2b}$$

as the adiabatic states diagonalise the Hamiltonian and the overlap between the two diabatic states is 0 one can see that

$$c_a c_b = \frac{H_{ab}}{\Delta E_{12}} \tag{4.3}$$

where ΔE_{12} is the vertical energy gap between the adiabatic ground state and first excited state and $H_{ab} = \langle \phi_a | \hat{H} | \phi_b \rangle$ is the electronic coupling between states a and b. The dipole moment between the ground state and the first excited state, μ_{12}, can be written as

$$\mu_{12} = \langle \psi_1 | \mathbf{r} | \psi_1 \rangle \tag{4.4}$$

It is possible to express μ_{12} in the diabatic basis set by substituting the expressions from Eq. (4.2) into Eq. (4.4). The diabats are defined so that the dipole moment vanishes between the two diabatic states ($\mu_{ab} = \langle \phi_a | \mathbf{r} | \phi_b \rangle = 0$)

$$\mu_{12} = c_a c_b (\mu_{bb} - \mu_{aa}) \tag{4.5}$$

where $\mu_a a = \langle \phi_a | \mathbf{r} | \phi_a \rangle$ and $\mu_b b = \langle \phi_b | \mathbf{r} | \phi_b \rangle$ are the dipole moments in the diabatic states. Using Eq. (4.3) the Eq. (4.5) becomes

$$\mu_{12} = \frac{H_{ab}}{\Delta E_{12}} (\mu_{bb} - \mu_{aa}) \tag{4.6}$$

Now $(\mu_{bb} - \mu_{aa})$ can be expressed in the adiabatic basis set by using Eqs. (4.2)

$$\mu_{12} = \frac{H_{ab}}{\Delta E_{12}} \sqrt{(\mu_{11} - \mu_{22})^2 + 4\mu_{12}^2} \tag{4.7}$$

Thus the electronic coupling according to GMHT is given by

$$|H_{ab}| = \frac{|\mu_{12}| \Delta E_{12}}{\sqrt{(\mu_{11} - \mu_{22})^2 + 4\mu_{12}^2}} \tag{4.8}$$

In special cases, when the initial and final states are symmetric the adiabatic dipole moment is $\mu_{11} = \mu_{22}$. Therefore, the equation is simplified to:

$$|H_{ab}| = \frac{1}{2}\Delta E_{12}. \tag{4.9}$$

In summary, this method obtains the diabatic coupling as half of the energy difference between the ground state and the first excited state ΔE_{12}. Therefore, the matrix that diagonalises the dipole matrix in the adiabatic basis set can be used to transform the adiabatic Hamiltonian to the diabatic Hamiltonian. This can be further generalised to more than two states [63, 64]. The accuracy of the GMHT results depends on the method which is used to calculate the adiabatic states. High level *ab initio* methods (multi-reference and post-Hartree-Fock methods) can be used to calculate diabatic coupling values by applying the generalised Mulliken–Hush theory (GMHT) of vanishing transition dipole moments. For example, for small molecules the adiabatic ground and the first excited states can be calculated with multi-reference configuration interaction (MRCI) [65] and n-electron valence state perturbation theory (NEVPT2) [66, 67]. After calculating the dipole matrix between those states, GMHT can be used to calculate the coupling values [68]. The method was generalised for multiple sites and can include bulk behaviour [63, 69]. Although these calculations give very accurate results, the drawback is that their computational costs grow extremely fast with system size. Nevertheless, GMHT is a useful tool for calculating the coupling and can be used in cases where the polarisation effects are significant such as donor-bridge-acceptor systems [70] and to evaluate experimental spectra [71].

4.1.2 Charge Constrained DFT

While GMHT calculates the coupling deductively from the adiabatic states, there are several methods to construct the diabatic states directly. For example, constrained

DFT (CDFT) obtains the diabatic states by introducing a constraint on the charge of the donor and the acceptor [58, 72]. In a CDFT calculation, the KS energy is minimised under the constraint that the charge difference between donor and acceptor is equal to a specified value (usually +1 or -1 for transfer of a full electron from donor to acceptor). The restriction is introduced by multiplying the density $\rho(\mathbf{r})$ with a weight function $w(\mathbf{r})$ which creates a charge difference between the region where the charge is to be localised and the rest of the space as

$$N_c = \int w(\mathbf{r})\rho(\mathbf{r})\mathrm{d}\mathbf{r} \tag{4.10}$$

where N_c is the charge difference between the restriction space and the rest of the space; in this case the donor and the acceptor. Therefore, the task is to minimse $E[\rho]$ subject to the normalised constraint

$$0 = \int w(\mathbf{r})\rho(\mathbf{r})\mathrm{d}\mathbf{r} - N_c \tag{4.11}$$

The constraint is added to the energy expression multiplied by a Lagrange multiplier:

$$W[\rho, V_c] = E[\rho] + V_c \left(\int w(\mathbf{r})\rho(\mathbf{r})\mathrm{d}\mathbf{r} - N_c \right) \tag{4.12}$$

The Kohn–Sham equations then become

$$\left(-\frac{1}{2}\Delta + \int \frac{\rho(\mathbf{r}')}{|\mathbf{r} - \mathbf{r}'|}\mathrm{d}\mathbf{r}' + v_{xc}(\mathbf{r}) + V w(\mathbf{r}) \right) \psi_i = \varepsilon_i \psi_i \tag{4.13}$$

where $v_{xc}(\mathbf{r})$ is the exchange-correlation functional and ψ_i are the Kohn–Sham orbitals. The expression W is minimised for given values of V and V is varied iteratively until the density $\rho = \sum_i |\psi_i|^2$ satisfies Eq. (4.10). Hence, the charge localised (or diabatic) states obtained from CDFT are adiabatic ground state energies of a KS Hamiltonian with a modified external potential.

The weight function depends on the definition of charge population. In this work, $w(\mathbf{r})$ is based on the Hirshfeld charge difference [73] between the donor D and the acceptor A

$$w(\mathbf{r}) = \frac{\sum_{i\in D} \rho_i(\mathbf{r} - \mathbf{R}_i) - \sum_{i\in A} \rho_i(\mathbf{r} - \mathbf{R}_i)}{\sum_{i=1}^{N} \rho_i(\mathbf{r} - \mathbf{R}_i)} \tag{4.14}$$

where N is the number of atoms in the system. $\rho_i(\mathbf{r} - \mathbf{R}_i)$ is the unperturbed electron density on atom i summed over all Kohn–Sham orbitals and weighted with the corresponding occupation number n_j

$$\rho_i(\mathbf{r} - \mathbf{R}_i) = \sum_j n_j |\psi_j(\mathbf{r} - \mathbf{R}_i)|^2 \tag{4.15}$$

In a dimer system, after obtaining Ψ_A where the charge is localised on the donor, Ψ_B where the charge is localised on the acceptor can be obtained by changing the constraint $N_b = -N_c$. Using the constructed diabatic states, the electronic coupling matrix element can be calculated as $H_{AB} = \langle \Psi_A | \mathcal{H} | \Psi_B \rangle$, where the Hamiltonian is replaced by the Kohn–Sham Hamiltonian constructed from the orbitals of state A and state B

$$\mathbb{H}'' = \begin{bmatrix} E_A & H_{AB} \\ H_{BA} & E_B \end{bmatrix} \tag{4.16}$$

where $E_A = \langle \Psi_A | \mathcal{H}_A^{\mathrm{KS}} | \Psi_A \rangle$ and $E_B = \langle \Psi_B | \mathcal{H}_B^{\mathrm{KS}} | \Psi_B \rangle$ are the energies in the diabatic states A and B. The off-diagonal elements are

$$H_{AB} = \langle \Psi_A | \mathcal{H}_B^{\mathrm{KS}} | \Psi_B \rangle \tag{4.17a}$$

$$H_{BA} = \langle \Psi_B | \mathcal{H}_A^{\mathrm{KS}} | \Psi_A \rangle \tag{4.17b}$$

Using the fact that the Ψ_A is the eigenfunction of $\mathcal{H}_A^{\mathrm{KS}}$, the equations can be trans-

formed by adding and subtracting $V_A \sum_{i=1}^{n} w_i(\mathbf{r}_i)$

$$H_{AB} = S_{AB}\langle\Psi_B|\mathcal{H}_B^{\mathrm{KS}} + V_B \sum_{i=1}^{n} w_i(\mathbf{r}_i)|\Psi_B\rangle - V_B\langle\Psi_A| \sum_{i=1}^{n} w_i(\mathbf{r}_i)|\Psi_B\rangle \tag{4.18a}$$

$$H_{BA} = S_{BA}\langle\Psi_A|\mathcal{H}_A^{\mathrm{KS}} + V_A \sum_{i=1}^{n} w_i(\mathbf{r}_i)|\Psi_A\rangle - V_A\langle\Psi_B| \sum_{i=1}^{n} w_i(\mathbf{r}_i)|\Psi_A\rangle \tag{4.18b}$$

where $S_{AB} = S_{BA}*$ is the off-diagonal element of the overlap matrix between the two diabatic states. By defining the weight matrix and using its off-diagonal elements $W_{AB} = W_{BA}*$, the expressions in Eq. (4.18) become

$$H_{AB} = S_{AB}\langle\Psi_B|\mathcal{H}_B^{\mathrm{KS}} + V_B \sum_{i=1}^{n} w_i(\mathbf{r}_i)|\Psi_B\rangle - V_B W_{AB} \tag{4.19a}$$

$$H_{BA} = S_{BA}\langle\Psi_A|\mathcal{H}_A^{\mathrm{KS}} + V_A \sum_{i=1}^{n} w_i(\mathbf{r}_i)|\Psi_A\rangle - V_A W_{BA} \tag{4.19b}$$

In general, $\mathbb{H}''$ is not Hermitian, $H_{AB} \neq H_{BA}*$, only when the two diabatic states are degenerate $\langle\Psi_B|\mathcal{H}_B^{\mathrm{KS}} + V_B \sum_{i=1}^{n} w_i(\mathbf{r}_i)|\Psi_B\rangle = \langle\Psi_A|\mathcal{H}_A^{\mathrm{KS}} + V_A \sum_{i=1}^{n} w_i(\mathbf{r}_i)|\Psi_A\rangle$ and $V_B = V_A$. This is almost never true in practice because of the approximate nature of the Kohn–Sham Hamiltonian. The off-diagonal element can be approximated by taking the average off-diagonal value, $\frac{1}{2}(H_{AB} + H_{BA})$. Another option is to describe the coupling value as the off-diagonal element of the diabatic orthogonal Hamiltonian $\mathbb{H}$. To this end, Ψ_A and Ψ_B can be orthogonalised by being transformed to Ψ_a and Ψ_b which are the eigenfunctions of the weight matrix. The generalised eigenvalue equation is

$$\mathbb{W}\mathbb{V} = \mathbb{S}\mathbb{V}\mathbb{L} \tag{4.20}$$

Here, $\mathbb{W}$ is the weight matrix, $\mathbb{L}$ is the diagonal matrix of the eigenvalues of $\mathbb{W}$ and the rows of $\mathbb{V}$ are the generalised eigenstates of $\mathbb{W}$, which are very similar to the states which diagonlise the transition dipole moment vector in generalised Mulliken–Hush theory but not identical. Once $\mathbb{V}$ is calculated, the orthogonal diabatic Hamiltonian

can be obtained as

$$\mathbb{H} = \mathbb{V}^{\dagger}\mathbb{H}''\mathbb{V} \tag{4.21}$$

and the coupling can be obtained as the off-diagonal element of $\mathbb{H}$. CDFT has been implemented into plane wave [74] and Gaussian codes [75]. The great benefit of this method is that it can include interaction with the surroundings [76, 77, 78]. Although constrained DFT is less computationally demanding than high level *ab initio* calculations, obtaining converged diabatic states can be computationally costly due to the possible slow convergence of the Lagrange multiplier [56]. Spin contamination is also common problem in the CDFT approach.

4.1.3 Fragment orbital DFT

The issues arising from spin contamination and the slow convergence of the Lagrange multiplier can be avoided when another way of directly constructing localised diabatic electronic state, fragment orbital density functional theory (FODFT), is used. In this case, the diabatic electronic states are constructed from the Kohn–Sham orbitals coming from isolated unconstrained DFT calculation on the isolated donor and acceptor molecules. The separation prevents spurious delocalisation of the electron which arises from the self-interaction error.

Taking the example of electron transport in a reduced dimer system, let us model the charge transition from the donor molecule to the acceptor molecule. The initial state (a) is a charged donor and a neutral acceptor $[D^{-} + A]$. After the transfer, the final state b is a charged acceptor and a neutral donor $[D + A^{-}]$. The coupling matrix element is calculated by taking the transfer integral between the two states a and b as

$$H_{ab} = \langle \psi_a | \hat{H} | \psi_b \rangle. \tag{4.22}$$

where ψ_a and ψ_b are the wavefunctions of diabatic states a and b. Similarly to the CDFT method, the exact Hamiltonian is replaced with the Kohn–Sham Hamiltonian

constructed from either state a or state b.

$$H_{ab} = \langle\psi_a|\hat{H}|\psi_b\rangle \approx \langle\psi_a|\hat{H}_b^{KS}|\psi_b\rangle. \tag{4.23}$$

or

$$H_{ba} = \langle\psi_a|\hat{H}|\psi_b\rangle \approx \langle\psi_a|\hat{H}_a^{KS}|\psi_b\rangle. \tag{4.24}$$

It is important to note that, while H_{ab} is approximately the same as H_{ba} for homodimer systems, the difference can be quite significant if the acceptor and the donor are different molecules. The states a and b are constructed the following way: assuming N electrons on the neutral monomers, each diabatic state representing the dimer can be regarded as a $2N+1$ electron system. These are expressed as a determinant built from the Kohn–Sham orbitals of the monomers D^- ($\{\phi_1^D, \dots \phi_{N+1}^D\}$) and A^- ($\{\phi_1^A, \dots \phi_{N+1}^A\}$. In practice, the orbitals calculated on the isolated monomers are concatenated and orthogonalised according to Löwdin and the aforementioned orbital subsets are used to construct the diabatic states. An illustration of this can be seen in Fig. 4.1.

$$\psi_a = \frac{1}{\sqrt{2N+1!}} \det(\phi_1^a, \dots, \phi_{2N+1}^a) = \frac{1}{\sqrt{2N+1!}} \det(\phi_1^D, \dots, \phi_{N+1}^D, \phi_1^A, \dots, \phi_N^A), \tag{4.25a}$$

$$\psi_b = \frac{1}{\sqrt{2N+1!}} \det(\phi_1^b, \dots, \phi_{2N+1}^b) = \frac{1}{\sqrt{2N+1!}} \det(\phi_1^D, \dots, \phi_N^D, \phi_1^A, \dots, \phi_{N+1}^A). \tag{4.25b}$$

Using the fragment orbital wavefunctions from Eq. (4.25a)

$$H_{ab} \approx \langle\psi_a|\hat{H}_b^{KS}|\psi_b\rangle \approx \langle\psi_a^{FO}|\hat{H}_b^{KS}|\psi_b^{FO}\rangle. \tag{4.26}$$

The expression can be simplified further by taking only the relevant orbitals into

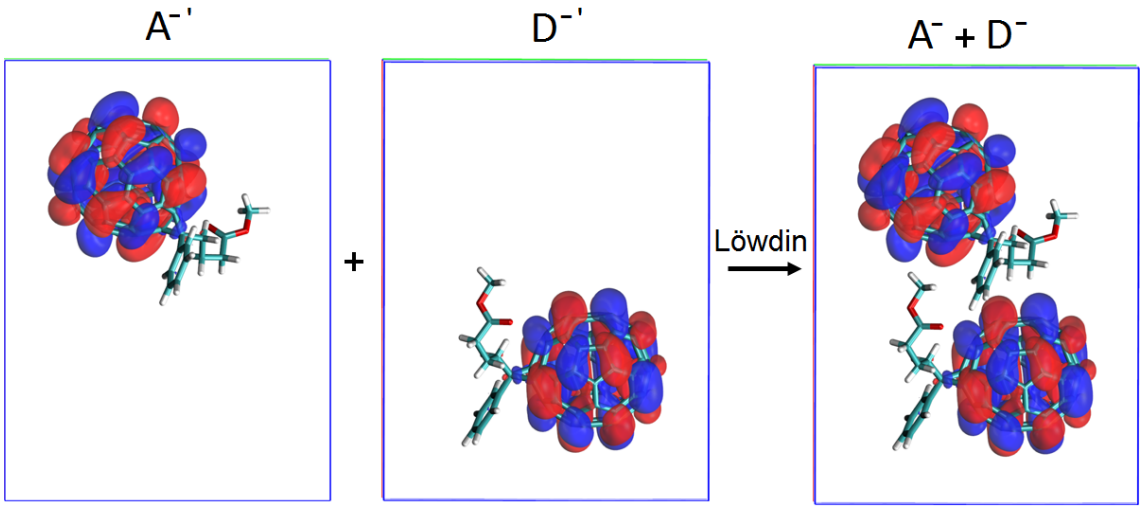

Figure 4.1: This figure illustrates the steps of obtaining orbitals for FODFT wavefunction construction. The wavefunctions are minimised on the charged isolated donor and acceptor monomers. Then, the obtained Kohn-Sham orbitals are concatenated and orthogonalised.

account

$$H_{ab} \approx \langle \psi_a^{\mathrm{FO}} | \hat{H}_b^{KS} | \psi_b^{\mathrm{FO}} \rangle = \langle \phi_{N+1}^{D} | \hat{H}_b^{KS} | \phi_{N+1}^{A} \rangle. \tag{4.27}$$

In summary, when using FODFT the following assumptions are made:

- **Only the HOMOs contribute to the electronic coupling**: Any contribution from any other part of the wavefunction is omitted.
- **The other orbitals are unaffected by the ionisation of the molecule**: Adding or removing an electron alters the electron density and may have an effect on the other Kohn–Sham orbitals. During the construction of the diabatic states and Kohn–Sham Hamiltonians, these relaxation effects on the orbitals are neglected.

- **All polarisation effects are neglected between the D and A molecules**: The donor and acceptor molecules are separated during the wavefunction optimisation. In the bulk, or in a dimer system (*e.g.* with CDFT), the SCF optimisation may be affected by the charge and the multipole moments of the donor. This completely omitted here.

FODFT has been successfully used to analyse C_{60} [45] and PCBM [49] systems as well as for biological cofactors [79, 80].

4.1.4 Density functional tight-binding

Density functional tight-binding (DFTB) offers a fast approximate way to calculate the electronic coupling matrix element. A reference density is obtained as the superposition of neutral atomic densities. The reference density is then expanded as a Taylor-series and the level of DFTB depends on the maximum order of the Taylor-series components. If only the first order components are used (DFTB1) there is no deviation from the reference density; therefore this method is not used. The most common levels of theory are DFTB2 [81] and DFTB3 [82]. If one describes the Kohn–Sham equations as

$$h_0\varphi_i = \left[-\frac{1}{2}\Delta + V_{\text{eff}}\right]\varphi_i = \varepsilon_i\varphi_i \tag{4.28}$$

where the effective potential is

$$V_{\text{eff}} = V_{\text{ext}} + V_{\text{ee}} + V_{\text{xc}} \tag{4.29}$$

and its components are the electron-nuclei interaction V_{ext}, the electron-electron interaction V_{ee}, and the exchange-correlation interaction V_{xc}.

These are described as

$$V_{\text{ext}} = -\sum_{j=1}^{N} \frac{Z_j}{|\mathbf{r} - \mathbf{R}_j|}\mathbf{r} \tag{4.30a}$$

$$V_{\text{ee}} = \int \frac{\rho(\mathbf{r}')}{|\mathbf{r} - \mathbf{r}'|}\mathrm{d}\mathbf{r}' \tag{4.30b}$$

$$V_{\text{xc}} = \frac{\delta E_{\text{xc}}}{\delta \rho} \tag{4.30c}$$

Here, $\rho = \sum_{i=1}^{n} \varphi_i^* \varphi_i$ is the electron density, n is the number of electrons; $\mathbf{R}_j$, Z_j and N are the position, the charge and the total number of the nuclei respectively; and $E_{xc}[\rho]$ is the exchange-correlation energy. The total energy expression is thus

$$E_{\text{tot}} = \sum_{i}^{n} \langle \varphi_i | h_0 | \varphi_i \rangle - \int V_{\text{ee}} \rho \mathrm{d}\mathbf{r} + E_{\text{xc}}[\rho] - \int \frac{\delta E_{\text{xc}}}{\delta \rho} \rho \mathrm{d}\mathbf{r} + E_{\text{nn}} \tag{4.31}$$

where E_{nn} is the nuclear repulsive interaction $E_{\text{nn}} = \sum_{j>l} \frac{Z_j Z_l}{R_{jl}}$ and $R_{jl} = |\mathbf{R}_j - \mathbf{R}_l|$. If Eq. (4.31) is expanded into a Taylor-series around a reference density ρ^0 where $\tilde{\rho} = \rho^0 + \delta\rho$ the first order terms vanish. The second order terms are non-zero for two components $E_{\text{xc}}[\rho]$ and $\int V_{\text{ee}} \rho \mathrm{d}\mathbf{r}$.

$$\begin{aligned} E_{\text{tot}} = \sum_{i}^{n} \langle \varphi_i | h_0 | \varphi_i \rangle - \int V_{\text{ee}} \rho^0 \mathrm{d}\mathbf{r} + E_{\text{xc}}[\rho^0] - \int \frac{\delta E_{\text{xc}}}{\delta \rho}\Big|_{\rho^0} \rho^0 \mathrm{d}\mathbf{r} + E_{\text{nn}} \\ + \int\int \left(\frac{1}{|\mathbf{r} - \mathbf{r}'|} + \frac{\delta^2 E_{xc}}{\delta\rho\delta\rho'}\Big|_{\rho^0} \right) \delta\rho\delta\rho' \mathrm{d}\mathbf{r}\mathrm{d}\mathbf{r}' \end{aligned} \tag{4.32}$$

where the zeroth order components are often summarised in the repulsive potential V_{rep} [83]:

$$V_{\text{rep}} = \int V_{\text{ee}} \rho^0 \mathrm{d}\mathbf{r} + E_{\text{xc}}[\rho^0] - \int \frac{\delta E_{\text{xc}}}{\delta \rho}\Big|_{\rho^0} \rho^0 \mathrm{d}\mathbf{r} + E_{\text{nn}} \tag{4.33}$$

The reference density ρ_0 can be written as a superposition of atomic densities $\rho^0(\mathbf{r}) = \sum_i^N \rho_i^0(\mathbf{r})$ and the potentials can be written as the superposition of atomic potentials $V_{\text{ee}}(\mathbf{r}) = \sum_i^N V_{\text{ee}i}(\mathbf{r})$. The second order energy term is usually approximated with

the monopole elements of a multipole expansion

$$\int\int\left(\frac{1}{|\mathbf{r}-\mathbf{r}'|}+\frac{\delta^2 E_{xc}}{\delta\rho\delta\rho'}\Big|_{\rho^0}\right)\delta\rho\delta\rho'\mathrm{d}\mathbf{r}\mathrm{d}\mathbf{r}'\approx\frac{1}{2}\sum_{j,l}\gamma_{lj}(R_{lj})\Delta q_j\Delta q_l \tag{4.34}$$

where Δq_j is a fragment charge localised on atom j such as $\delta\rho=\sum_j\Delta q_j\delta\rho_j$ [83]. The value of $\gamma_{l,j}$ depends on the second derivative of the Hartree and the exchange correlation contributions. In the linear combination of atomic orbitals method, the Kohn–Sham orbitals can be written as a linear combination of non-spin polarised spherical pseudo-atomic orbitals obtained by solving

$$\left[-\frac{1}{2}\Delta+V^0_{\mathrm{eff,j}}+\left(\frac{r_j}{r_0}\right)^2\right]\phi_m=\epsilon_m\phi_m \tag{4.35}$$

where j is the atomic index and r_0 is the confinement radius which is often set as 1.85 times the covalent radius [84] but is chosen to be larger in this case in order to describe the long range behaviour of the orbitals. DFTB methods, just like regular DFT, can be combined with charge constrained (CDFTB) and fragment orbital (FODFTB) methods to calculate electronic coupling values. The main difference compared to full density functional theory is that FODFTB is heavily dependent on parameterisation [82, 85]. DFTB is a popular method for calculating electronic couplings in large systems as it scales favourably with size and can be used in systems as large as peptides [86], DNA base pairs [87, 88] and in polymers [19].

4.2 Systems

The molecules used to illustrate the characteristics of these techniques are all π-conjugated homo-dimers. The molecules were chosen to represent the most fundamental characteristics of organic semiconducting materials as well as biological charge transfer systems.

The primary aim was to sample a broad variety of molecules. The effects of the

number of double bonds and the various sizes and shapes of π-conjugated molecules were considered, as well as the effects of heteroatoms in the system and deviation from perfect stacking.

The size of the molecules range from small to medium sized. The minimum size was set by the criterion that the molecule had to form a stable anion. To this end, the individual monomers had to have a positive vertical electron attachment (VEA) energy when tested with PBE [89] and aug-cc-pVTZ basis set [90]. Although the general idea was to use high level *ab initio* calculations as reference such as MRCI+Q, the lower limit of stable anions eliminated small molecules such as ethylene and benzene, therefore other reference methods had to be chosen.

The upper limit of the size of the molecules was set by the feasibility of high-level *ab initio* calculations. In Ref [68], the relatively small size of the molecule (ranging in size from acetylene to benzene) permitted the application of multi-reference configuration interaction (MRCI) and n-electron valence state perturbation theory (NEVPT2). Due to the relatively large size of the molecules, the spin component scaled approximate coupled cluster method (SCS-CC2) was chosen as the reference calculation method. The set consisted of a series of acenes, and perylene which were used to test the effect of the increasing conjugation length in pure hydrocarbons. The acenes ranged from anthracene to pentacene as neither benzene nor naphthalene formed a stable anion. In fact, the smallest acene to bind an electron (VEA=0.64 eV) was anthracene (See Fig. 4.2). The effect of the heteroatoms in the system was tested with medium sized molecules including perfluorinated anthracene, where all hydrogens are replaced with fluorine atoms, porphin, and perylene-diimide. These D_{2h} molecules form the **HAB7-** data set.

Three further molecules were considered to be included in the comparison: coronene (D_{6h}), triphenylene (D_{3h}), and the smallest fullerene C_{20} (D_{2h} due to Jahn–Teller distortion). While coronene and tripheylene have degenerate LUMO and LUMO+1, C_{20} has quasi-degenerate LUMO and LUMO+1. These degenerate states cannot be

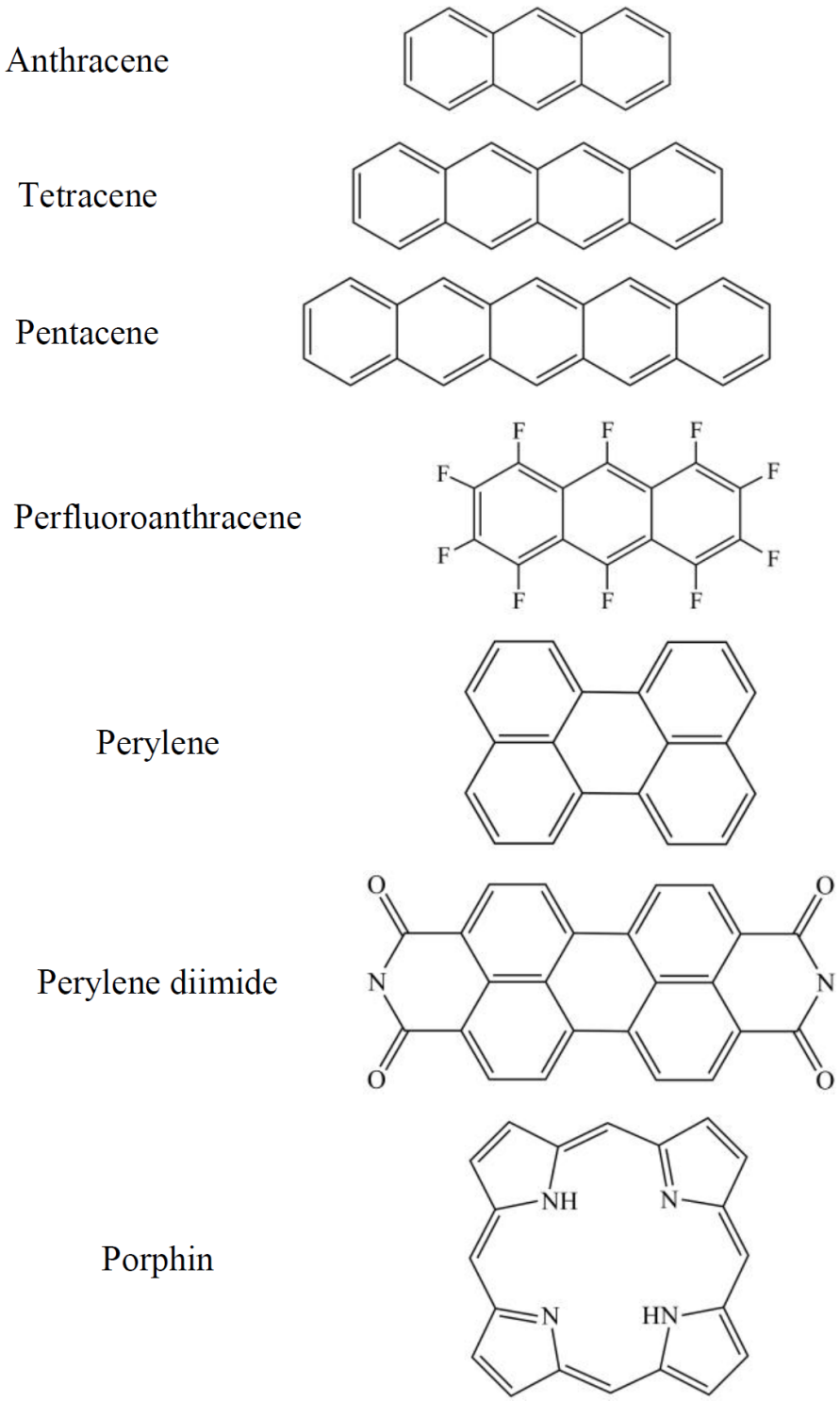

Figure 4.2: The seven molecules which were stacked to assess the accuracy of CDFT/X, FODFT, FODFTB coupling calculation methods against GMHT+SCS-CC2 at distances ranging from 3.5 to 5.0 Å. In addition, six randomly oriented anthracene pairs were also used to assess the effects of random orientation on the coupling values.

treated with ROHF+SCS-CC2 and these molecules are too large for multi-reference methods. Although quasi-degenerate C_{20} was converged with ROHF the $\mathcal{T}_1$ amplitudes [91] were much larger than for the rest of the systems (0.035). The same state could not be obtained with CDFT, FODFT, and FODFTB, with CDFT having serious convergence issues when only generalised gradient approximation (GGA) exchange was used [89].

The effects of the relative orientation were tested with randomly orientated anthracene dimers. These were the only systems which were not perfectly symmetric. Although the method is fully applicable for hetero-dimers symmetry was crucial for the computationally intensive reference method and combining anthracene with another molecule would have been computationally even more intensive.

4.3 Simulation details

The coordinates for the coupling calculation were constructed in the following way. The neutral monomer structures were optimised using standard DFT calculations with the BP86 functional [92, 93], in def2-TZVP basis set [94, 95] and resolution of identity approximation [96, 97] with the Turbomole package [98]. The SCF energies were converged to 10^{-7} a.u. while the electronic gradient convergence criterion was set to 10^{-4} a.u. An enlarged DFT integration grid (m4) was used. After minimisation the frequency calculations (of the same level of theory as the energy optimisation) showed that all normal modes were positive. The symmetric dimer constructions were done by replicating the optimised monomer structure along the axis perpendicular to the plane of conjugation.

As it is mentioned in our publication [56], reference value calculations were calculated in our group by Adam Kubas using the generalised Mulliken–Hush theory. All systems except for the randomly oriented anthracene pairs consisted of symmetric homo-dimers hence Eq. (4.9) was used. In the randomly oriented anthracene

cases, the more general Eq. (4.8) was used. The ground and the first excited state were calculated with the spin component scaled approximate coupled cluster method [99, 100] based on orbitals calculated with restricted open-shell Hartree–Fock method (ROHF). The ROHF calculations helped to prevent spurious spin-contamination which was present in UHF calculations. The $\mathcal{T}_1$ tests [91] showed values of $|\mathbf{t}_1|/\sqrt{N}$ smaller than 0.02 for most systems and smaller than 0.025 for all systems. Some of these values were slightly larger than the rule of thumb (0.02) as reported in Ref. [101]. However, this was not a problem in Ref [68] where the $\mathcal{T}_1$ diagnostic results for the UHF/SCS-CC2 results for the systems in Ref [68] gave values between 0.02 and 0.03 while still approximating the MRCI+Q results well. In order to improve performance, the spin component scaling was done by using the same ($c_{\mathrm{ss}} = 1/3$) and opposite spin-component factors ($c_{\mathrm{os}} = 6/5$) on the spin components of the Jacobian matrix used for calculating the excitation [102]. Resolution of identity approximation was used with an auxiliary basis set according to Ref [103]. The basis set for heavy atoms was aug-cc-pVTZ [90] and the for hydrogen was cc-pVDZ [104], similarly to those in Ref [68].

I contributed CDFT and FODFT calculations to this benchmark study. The calculations were done using the CPMD plane wave package [105]. The simulation details were identical to those in Ref. [68]. In the CDFT calculations, the Lagrange multiplier was optimised until the Hirshfeld charge difference between the donor and the acceptor monomers was 1e to within a tolerance of 5×10^{-5} e. All atoms of the donor and acceptor monomers were included. All CDFT calculations were done *in vacuo* using the PBE functional [89]. The influence of exact exchange was tested by partially replacing the GGA exchange with different percentages of (exact) Hartree–Fock exchange (HFX). These calculations are labelled as "CDFT/X", where X denotes the percentage of HFX. Since the code uses a plane wave basis set in isolated system calculations, the effect of the images has to be decoupled from the system. It is also important that the chosen unit cell (box size) is large

enough to allow the wavefunction to converge to zero at the box boundaries. A minimum vacuum gap of 4 Å on each side of the molecule proved to be enough; further increment of the box size (and the vacuum gap) did not change the coupling values by more than 0.2 meV. Troullier–Martins pseudopotentials [106] were used to replace core electrons. Therefore, in addition to the 4 Å vacuum gap, the box was also ensured to be larger than twice the system size (approximating the size with the van der Waals radius). The basis set was terminated at 80 Ry reciprocal space plane wave cut-off for the Kohn–Sham orbitals in order to fulfill the size criteria for the Martyna–Tuckerman Poisson solver [107]. A decreased cut-off was used for exact exchange density calculations. The dimers were centred in a rectangular box. FODFT(2N + 1) calculations were performed with the same parameters as CDFT, using the unmodified PBE functional. The orbitals were orthogonalised using the Löwdin orthogonalisation method. The coupling values were calculated with both possible Kohn–Sham Hamiltonians, $\hat{H}_b^{KS}$ (H_{ab}) and $\hat{H}_a^{KS}$ (H_{ba}), depending on which orbital is excluded when constructing the operator (see Fig 4.1). Finally, the obtained couplings H_{ab} and H_{ba} were averaged.

FODFTB calculations were performed by our collaborators using their custom written code. To capture the intermolecular interactions, in addition to the halorg-0-1 DFTB parameters [81, 108] a second less confined parameter set was used as in Ref [68] with additional parameters for fluorine. The calculations were done with a total energy convergence criterion of 10^{-7} a.u. The basis set was an effective double-zeta description [81], the confinement in Eq. (4.35) was 8 a.u. for the wavefunction and ∞ for the density for all atoms.

While GMHT and FODFTB values were calculated in a Gaussian basis, set CDFT and FODFT values were calculated in plane wave basis set. The basis set, however, does not have a significant effect on the coupling Kubas *et al* compared the methods with different basis set in Ref [68]. Moreover Gaussian basis set CDFT code implemented in the deMon2k program package and the plane wave CDFT code

implemented into CPMD gave very similar results for donor-bridge-acceptor systems [109].

4.4 Results

The results obtained with fragment orbital and charge constrained DFT methods are compared to the SCS-CC2 reference values by calculating the mean relative unsigned error (MRUE), the mean unsigned error (MUE), the mean relative signed error (MRSE), and the maximum error (MAXERR) according to equations (4.36).

$$\mathrm{MRUE} = \frac{1}{N}\sum_{i=1}^{N}\left|\frac{H_{ab}^{\mathrm{ref}} - H_{ab}^{\mathrm{calc}}}{H_{ab}^{\mathrm{ref}}}\right|_i, \tag{4.36a}$$

$$\mathrm{MUE} = \frac{1}{N}\sum_{i=1}^{N}\left|H_{ab}^{\mathrm{ref}} - H_{ab}^{\mathrm{calc}}\right|_i, \tag{4.36b}$$

$$\mathrm{MRSE} = \frac{1}{N}\sum_{i=1}^{N}\left(\frac{H_{ab}^{\mathrm{ref}} - H_{ab}^{\mathrm{calc}}}{H_{ab}^{\mathrm{ref}}}\right)_i, \tag{4.36c}$$

$$\mathrm{MAXERR} = \max\left|H_{ab}^{\mathrm{ref}} - H_{ab}^{\mathrm{calc}}\right|_i. \tag{4.36d}$$

4.4.1 Stacked systems

All CDFT, FODFT, and FODFTB results for the stacked systems compared with the reference values can be seen in Table 4.1. The reference SCS-CC2 calculations revealed that intermolecular distance had the most significant effect on the coupling values, outweighing the effect of any other structural difference between the molecules. At 3.5 Å separation the couplings ranged between 311 and 424 meV, while as the intermolecular distance increased to 5.0 Å the coupling values decreased to 24 and 63 meV, showing a greater variance at larger separations. There were two other characteristics which had a major effect on the coupling values. Increasing conjugation length resulted in smaller coupling values as can be seen in the example of the acenes, where anthracene has the highest coupling values and pentacene has

the lowest when compared at the same distance. This phenomenon becomes more prominent as the separation increases. Even more significant coupling reduction can be introduced through electron withdrawing groups: perfluorinated anthracene had 26% smaller coupling at 3.5 Å and 55% smaller at 5.0 Å compared to anthracene. Similarly, perylene-diimide had 12% smaller coupling than perylene. It is assumed that both the electron withdrawing groups and the increased conjugation length reduces the couplings by introducing a more stable anion.

Inclusion of exact exchange proved to be crucial in CDFT calculations. Without Hartree–Fock exchange, this approximation is often subject to spin contamination and hybrid functionals are needed to aid the localisation of the diabatic states [68]. As expected, CDFT/0 overestimated the coupling significantly (MRUE 60.8%), however increasing the percentage of Hartree–Fock exchange decreased the coupling. Introducing 25% exact exchange improved the results but the list value of the error was still large. Interestingly, using range-separated HSE06 functional did not have any advantage and the obtained errors were very similar to PBE0 which also contains 25% exact-exchange. The best estimate for the coupling values was given by CDFT with 50% Hartree–Fock exchange with a MRUE of only 8.2%.

Although FODFT and FODFTB are more approximate than CDFT as they omit polarisation effects between the donor and the acceptor, they gave slightly better results than CDFT/0 with PBE. This clearly shows that in the case of CDFT/0, over-delocalisation outweighs the advantage of higher level theory. In fact, in terms of MRUE the FODFT results are closer to the CDFT/25 results. FODFTB gives larger errors than FODFT with 53.5 % MRUE.

Linear scaling improved the results significantly for all presented methods. The scaled errors can be seen in Table 4.2 and on Panel B of Fig 4.3 the scaled results are marked with the 's' prefix. The lines were fitted with the least squares method and the R^2 values were 0.9990, 0.9996, 0.9988, 0.9997, 0.9985, and 0.9879 for CDFT/0, CDFT/25, CDFT/50, HSE06, FODFT, and FODFTB respectively.

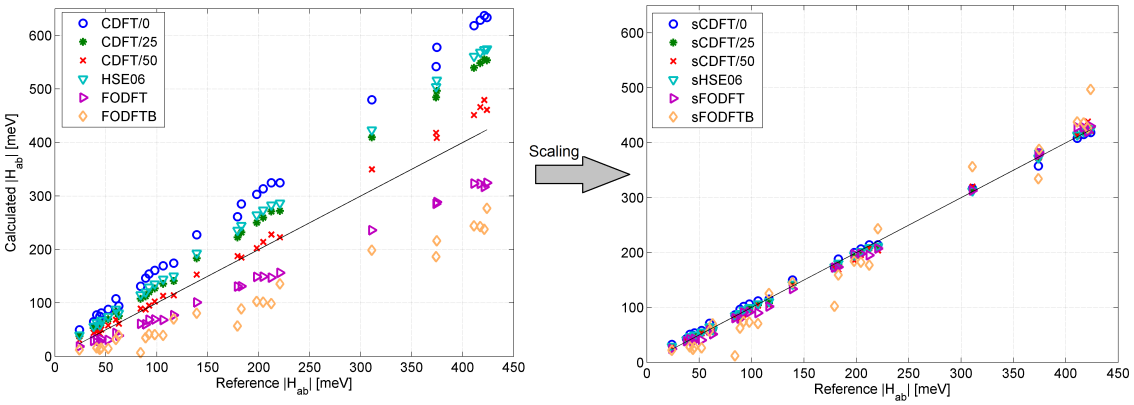

Figure 4.3: Different electronic coupling calculation method results on the stacked systems of anthracene, tetracene, pentacene, perfluoro-anthracene, perylene diimide, perylene and porphin compared to SCS-CC2 results depicted in a solid black line. The second panel clearly shows the advantages of the uniform linear scaling for all methods.

Again CDFT/50 gives results which can even be used without a correction factor for stacked systems. FODFT also proved to be a valuable method as well, as it is computationally inexpensive providing a good approximation for high-level *ab initio* calculations, after a correction factor of 1.3 is applied to the results. These values are expected to be fairly general for stacked π-conjugated molecules. In fact, the ones derived for positively charged systems in Ref [68] were very similar especially for CDFT/50 and FODFT.

The distance dependence of the stacked systems was also assessed and the results are presented in Table 4.3. The β parameters were calculated by fitting (4.37) to the coupling values obtained at various separation length for each molecule with each method.

$$H_{ab}(r) = H_{ab}^{0} \exp\left(-\frac{\beta}{2} r\right) \tag{4.37}$$

The relative error had very little distance dependence for CDFT/25, CDFT/50 and CDFT with HSE06 functional as well as FODFT. On the other hand CDFT/0 and FODFTB methods showed that the MRUE increases with the dimer separation. In the CDFT/0 case, the issue originates, again, from the over-delocalisation of the excess electron due to the pure GGA functional. For FODFTB, the error is

due to the minimal basis set used for the calculations, which fails to fully describe the more diffuse singly occupied molecular orbitals of the anions despite special optimisation. Furthermore, the coupled orbitals were virtual orbitals and therefore distance dependency could not be reproduced. As a consequence, the FODFTB electronic couplings decrease too quickly with dimer separation which results in a β parameter which overestimates the *ab initio* results by 26%.

4.4.2 Randomly oriented anthracene molecules

As shown for the stacked systems, although there are small differences between the equidistant coupling values for different molecules, they are in general rather similar. To test the effect of broken symmetry, a few randomly oriented dimers were used. Since the reduction of symmetry from D_{2h} to C_1 increased the computational demands significantly, the smallest possible system: a dimer of anthracene molecules was chosen for this study. Even then, out of the fifteen possible conformations only six dimers converged as the system size was too large to converge into a shallow minimum within a reasonable computational time. The SCS-CC2 reference calculations were compared to CDFT/50, CDFT/0, FODFT and FODFTB results. The scaled results, corrected with the factors from Table 4.2, are presented in Table 4.4. Just like in the stacked case, the separation of the nearest atoms of the two monomers r had a significant effect on the couplings, which decreased with increasing interatomic distance. However, intermolecular distance is not the only factor which affects the coupling values. As large π-conjugated molecules have a complicated nodal structure, imperfectly stacked structures have radically reduced coupling values as was shown in Ref [49]. This also arises partly from the fact that perfectly stacked systems have the lowest overall distance. A similar effect can be observed in the work of Breuer *et al.* where the main factor affecting the coupling values is the type of stacking [79]. This is why configurations 2 to 4 have couplings which are an order of magnitude smaller than their perfectly stacked counterparts at 5 Å (See Fig. 4.4).

Even for the last two entries in Table 4.4 where the shortest interatomic distance is

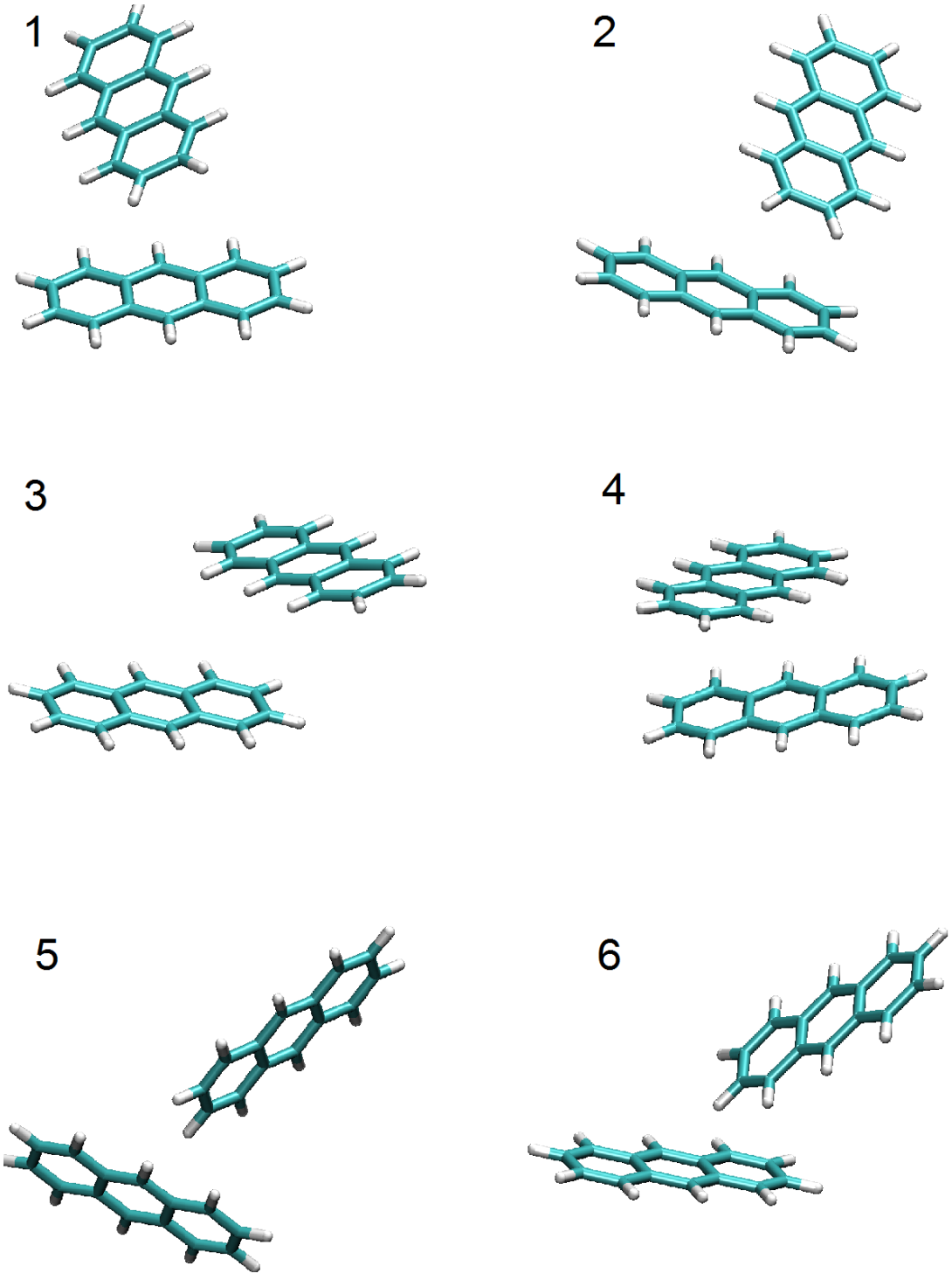

Figure 4.4: Randomly oriented anthracene pairs used for testing the effect of orientation. These structures are quite different from the perfectly stacked systems presented above. The numbers next to the panels refer to the ID numbers presented in Table 4.4.

much less than 3.5 Å the overlap is around the same order of magnitude as it was for the 5 Å separation perfectly stacked anthracenes. This also puts the accuracy of the methods to question for these rotated structures as couplings below 5 meV are subject to significant numeric noise. Nevertheless, despite the relatively large noise the trends of the coupling values for different methods are preserved. Also, similarly to the stacked cases for dimer 5 and 6, FODFT underestimates H_{ab} while CDFT overestimates it. It is interesting to see that the errors with CDFT/50 are larger than in the stacked case (200 meV while reference is 91 meV). This is probably due to the very short carbon-hydrogen interatomic distance where the over-delocalisation is a more significant issue which can be remedied with increased percentage of HFX. At such small distances, the weighting function can also have an effect on the CDFT results [72, 74].

4.5 Computational demands

Several different methods were presented in the previous section which gave different errors and it was shown that CDFT/50 approximates the reference values best. However, it is interesting to see how the computational demands compare to the errors. As mentioned earlier, the coupling calculation can act as a bottleneck when charge transport models are used for extended systems. Fig. 4.5 shows the CPU time with different methods on different stacked systems and the corresponding error.

The size limitation of SCS-CC2 has been discussed earlier and it is not applicable for any system larger than a dimer. While CDFT with 50% exact exchange gives very good results and can be applied to larger molecules than SCS-CC2, it is still not feasible for systems as large as a C_{60} dimer. Furthermore, while couplings for a single dimer consisting of small molecule organic semiconductors such as rubrene or pentacene are possible, a statistically significant system of several molecules would be impossible with CDFT and HFX. FODFT requires less computational time and

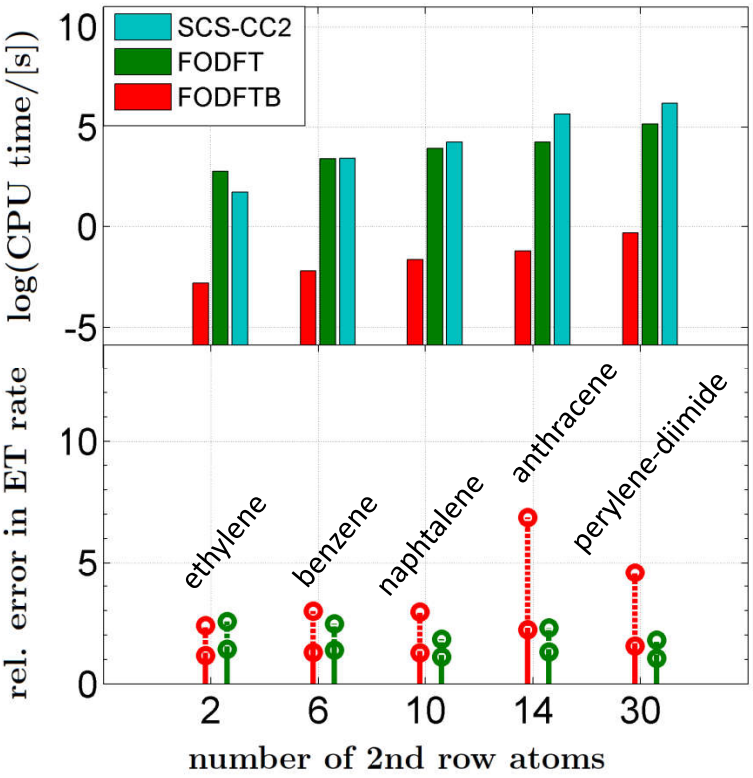

Figure 4.5: CPU time of different coupling calculation methods for different molecules and the error bar compared to the high precision GMHT with SCS-CC2 method. The stems refer to the mean unsigned relative error according to Eq. (4.36); the solid stems show the scaled errors using the scaling factors from Table 4.2 while the dashed stems show the actual relative error of different methods.

without scaling the errors are similar to that of CDFT/25; with scaling the errors reduce further. The fastest method presented here is FODFTB which is feasible even for NAMD, but the error is rather large due to the minimum basis set applied.

4.6 Conclusion

In this chapter, coupling values for seven π-conjugated negatively charged molecules were presented with different coupling calculation methods. The couplings were calculated between perfectly stacked dimers with a separation of 3.5 Å, 4.0 Å, 4.5 Å, and 5.0 Å. The coupling calculation methods were compared to SCS-CC2 reference results. The methods with which the couplings were calculated were charge

constrained density functional theory with different exchange correlation functionals, fragment orbital DFT, and fragment orbital density functional tight-binding. CDFT with 50% exact exchange had the smallest relative error compared to the reference values, while decreasing proportion of exact exchange increased the errors significantly. In fact, the errors for CDFT/0 were much larger (MRUE= 60.8%) than in the positively charged case [68] (MRUE= 38.7%) which is due to the more prominent over-delocalisation in the anionic system. Since CDFT with 50% exact exchange proved to be the best approach for both oxidised [68] and reduced example molecules it is expected to be transferable to other π-conjugated systems. Nevertheless, further generalisation should be avoided as the recommended HFX percentage may vary for different systems. McKenna *et al.* found that 25% exchange worked best for electron tunneling between lattice defects in MgO [76, 77]. Interestingly, range separation offered no clear advantage for these systems: the HSE06 functional yielded very similar results to to CDFT/25 (PBE0).

Slightly faster than CDFT+PBE, FODFT+PBE also matched the reference values better as over-delocalisation was prevented by the separation of dimers. The relative error improved further when uniform scaling factors were applied to the results. For FODFT the scaling factor was very similar in both the reduced and oxidised cases (around 1.3) [68] and the MRUE was reduced from 27.9% to 5.9% overall. The scaled FODFT+PBE results gave similar errors to CDFT/50 at the fraction of the computational cost. FODFTB was clearly the fastest listed method but the errors were also larger compared to other methods. This is due to the minimal basis set and the virtual orbitals used to construct the LUMO for the coupling calculation. Yet, a uniform scaling factor improves the errors significantly.

Finally, the results for the randomly oriented anthracene dimers suggest that all approximate methods should be used with caution when small coupling values are calculated. Couplings lower than 5 meV were not reproduced as well as higher coupling values and the methods show larger variance when compared with the

randomly oriented thiophenes [68].

Although the data set was small, the transferability of the method is expected to be good. For example, removing any molecule type from the set causes the MRSE to change by 1% or less. The error is arguably better represented in the context of the non-adiabatic electron transfer rate. Taking the example of using coupling values with Marcus theory, the electronic coupling is an external factor in the rate expression $k \propto H_{ab}^2$. Hence, if the MRUE of the coupling is 20% the MRUE of the rate is 40% provided that the activation energy can be obtained accurately. This means that all methods predict the Marcus rate with less than 60% relative error. Of course the accuracy of the rate is subject to the accurate calculation of the reorganisation energy and the driving force.

Table 4.1: Electronic coupling matrix element values for the negatively charged symmetric perfectly stacked dimers of anthracene, tetracene, pentacene, perfluoro-anthracene, perylene-diimide, perylene and porphin at d separation calculated with SCS-CC2+GMHT, CDFT/X, FODFT, and FODFTB methods for the HAB7- set, where X denotes the percentage of Hartree–Fock exchange. All coupling values are in meV. The error values for each method were calculated according to Eqs. (4.36) using SCS-CC2+GMHT results as reference values.

System	d [Å]	Ref	CDFT/0	CDFT/25	CDFT/50	HSE06	FODFT	FODFTB
anthracene	3.5	421.1	637.0	555.4	479.2	573.1	316.9	237.8
	4.0	212.3	324.5	256.6	227.8	282.8	147.3	98.8
	4.5	106.1	169.4	129.5	113.1	144.1	68.0	39.4
	5.0	52.3	87.9	65.8	58.0	74.5	30.7	14.8
tetracene	3.5	417.2	628.8	548.3	466.0	568.2	322.9	242.9
	4.0	204.3	313.1	259.4	213.8	273.3	149.2	101.6
	4.5	97.9	160.8	127.1	102.4	135.4	69.2	40.8
	5.0	45.4	81.5	62.5	50.4	67.5	32.5	15.5
pentacene	3.5	411.0	618.3	539.4	451.3	560.6	323.2	243.9
	4.0	198.0	303.0	250.1	202.4	264.2	148.5	102.7
	4.5	92.4	154.0	120.1	95.1	129.3	68.5	41.4
	5.0	41.0	77.7	58.2	45.7	63.1	32.0	15.8
perfluoro-anthracene	3.5	310.9	479.6	409.5	349.7	423.0	236.1	198.4
	4.0	139.1	227.2	183.4	152.7	192.7	101.0	80.9
	4.5	59.9	107.9	83.3	68.5	87.9	44.0	31.9
	5.0	24.0	49.6	37.5	30.6	39.6	18.7	12.4
perylene-diimide	3.5	373.8	541.8	484.0	417.7	504.1	285.1	227.0
	4.0	179.2	261.0	222.7	187.4	235.4	130.5	94.1
	4.5	84.1	131.2	107.9	89.2	115.1	60.9	37.5
	5.0	38.0	65.1	52.8	44.0	56.1	29.1	14.4
perylene	3.5	423.7	633.7	553.7	460.7	574.7	324.6	236.3
	4.0	220.7	324.5	272.1	222.7	286.2	156.4	98.5
	4.5	116.6	174.0	140.8	114.1	149.8	77.0	39.3
	5.0	62.8	94.4	75.4	61.1	80.6	39.0	15.0
porphin	3.5	374.5	577.7	496.3	408.5	516.4	288.5	216.0
	4.0	182.9	285.0	231.7	184.8	244.3	131.1	88.7
	4.5	89.0	146.2	111.9	87.3	119.7	59.8	34.7
	5.0	44.1	74.7	55.1	42.7	58.7	28.1	13.2
				Errors				
MUE [meV]			96.7	53.3	15.0	64.2	46.5	85.3
MAXERR [meV]			215.9	134.3	58.1	152.0	104.2	187.4
MRSE [%]			60.8	30.7	7.5	38.1	-27.9	-53.5
MRUE [%]			60.8	30.7	8.2	38.1	27.9	53.5

Table 4.2: Revisited H_{ab} errors after uniform linear scaling is applied to all approximate coupling values compared to SCS-CC2 reference values for the stacked systems. The prefix 's' refers to the scaled values.

Method	Scaling factor	MUE [meV]	MRSE [%]	MRUE [%]	MAX [meV]
sCDFT/0	0.660(0.004)	5.9	6.1	7.3	16.2
sCDFT/25	0.768(0.003)	3.9	0.4	3.8	11.7
sCDFT/50	0.915(0.006)	6.2	-1.7	4.9	17.3
sHSE06	0.738(0.002)	3.2	1.9	3.8	9.6
sFODFT	1.325(0.010)	7.0	-4.4	5.9	17.2
sFODFTB	1.795(0.038)	21.6	-15.4	19.5	47.7

Table 4.3: Distance dependence of the coupling values according to Eq. (4.37) with the different coupling calculation methods. All β values are in $\mathrm{\AA}^{-1}$. The error values with respect to SCS-CC2+GMHT reference values were calculated with Eqs. (4.36).

System	Ref	CDFT/0	CDFT/25	CDFT/50	HSE06	FODFT	FODFTB
anthracene	2.78	2.64	2.77	2.81	2.72	3.11	3.70
tetracene	2.96	2.72	2.90	2.97	2.84	3.07	3.67
pentacene	3.07	2.76	2.96	3.05	2.91	3.08	3.65
perfluoro-anthracene	3.41	3.02	3.18	3.24	3.15	3.38	3.70
perylene-diimide	2.55	2.54	2.66	2.70	2.62	2.83	3.68
perylene	3.05	2.82	2.95	3.00	2.92	3.05	3.69
porphin	2.85	2.72	2.93	3.01	2.89	3.10	3.72
			Errors				
MUE [$\mathrm{\AA}^{-1}$]		0.21	0.10	0.08	0.12	0.15	0.74
MAXERR [$\mathrm{\AA}^{-1}$]		0.39	0.23	0.17	0.26	0.33	1.13
MRSE [%]		-6.8	-1.3	0.8	-2.7	5.0	25.8
MRUE [%]		6.8	3.3	2.9	3.9	5.3	25.8

Table 4.4: Coupling results for the randomly oriented anthracene dimers. d marks the closest C-C distance between the dimers. All coupling values are in meV. The mean unsigned error is calculated according to Eq. (4.36) using the SCS-CC2 coupling values as reference.

Dimer ID	d [Å]	Ref	sCDFT/0	sCDFT/50	sFODFT	sFODFTB
1	5.46	0.0	0.9	0.7	1.3	0.1
2	4.79	2.6	8.7	5.3	5.7	3.3
3	4.59	1.7	6.0	4.6	5.6	2.0
4	3.52	2.3	0.9	2.7	2.8	0.3
5	2.24	46.4	174.3	73.6	31.3	27.3
6	2.14	91.5	287.7	200.6	70.6	52.3
MUE [meV]		56.2	23.8	7.5	10.2	12.3

5 Fast Analytic Overlap Method

In this chapter, I will focus on the calculation of the off-diagonal elements of the electronic Hamiltonian in the diabatic representation (H_{ab}). The efficient calculation of these elements is an important step towards mixed quantum-classical molecular dynamics providing the quantum mechanical components in the model: the electronic Hamiltonian, the overlap matrix, and the non-adiabatic coupling vector elements. First, I will describe my theoretical work towards an ultra fast yet accurate calculation of overlap matrix elements where the electronic coupling matrix elements are approximated as being proportional to the electronic overlap of the singly occupied molecular orbitals. Here, I will emphasise how the reduction of the basis set affects the accuracy and the computational costs of the calculations. The details of the semi-empirical parameter derivation to approximate the Hamiltonian off-diagonal elements are also discussed. A broad selection of structures are used to fit the parameters using fragment orbital DFT for reference calculations. At the end of the section the derived parameters are tested against independent calculations. The following section discusses the application of the method on heme compounds containing transition metals and tackles the issue of how the method can be used in molecular dynamics. Finally, I present the details of how the overlap method can be used to approximate the non-adiabatic coupling vector (NACV) elements.

Several semi-empirical methods were presented in Chapter 3 but the computational costs of even the fast FODFTB method scale unfavourably with molecule size to be able to use them for non-adiabatic molecular dynamics in large condensed phase systems [48]. An even faster method can be introduced by neglecting all of the

four-electron integrals and using the proportionality between the electronic coupling and the overlap integrals to approximate H_{ab} as

$$H_{ab} = CS_{ab}. \tag{5.1}$$

This ansatz is similar to the idea of Hückel theory [110]. However, while the latter was originally used to describe H_{ab} between atom-centred orbitals of a single molecule here, H_{ab} refers to the electronic coupling between molecular orbitals on different molecules [110]. The relation (5.1) has been tested on donor-acceptor pairs of DNA bases [111], acenes [112], and fullerenes [48], and it was found to give an excellent approximation for charge transport, with a proportionality constant of $C = 14$ eV [48]. It remains unclear, however, if C has to be reparameterised for every single donor-acceptor system or if Eq. (5.1) can be generalised to a large class of OSC materials described by a single value for C.

The main requirement to be able to apply non-adiabatic molecular dynamics on realistic (large) organic semiconducting systems is to be able to calculate the Hamiltonian and overlap matrices in an efficient way. For this purpose, we replace the diabatic state wavefunction by the highest singly occupied molecular orbital (SOMO). Similarly to the FODFT method the wavefunction of the isolated molecule was used for the calculations omitting any kind of polarisation effects of the environment. This means that only one self-consistent field calculation is needed from which the wavefunction is determined. This wavefunction is later reconstructed for every molecule forming the bulk and for every molecular dynamics snapshot.

The key for minimising the computational requirements of calculating the overlap is the choice of an optimal basis set to describe the SOMO. This basis set has to be as small as possible yet give results which are in good accordance with overlap values calculated with much larger basis sets. To this end, the SOMO was expanded in the minimum Slater type valence orbital basis set (STO: $1s$ for H $2s$; $2p$ for C,

N, O; and $3s$, $3p$ for S). For improved computational time, further reduction of the basis set was considered. Since organic semiconductors are almost exclusively π-conjugated molecules and these delocalised π-orbitals usually dominate the SOMO of the molecules, the effect of omitting p_σ and s components has been studied and is presented later. The overlap with these projected orbitals is

$$S_{ab} \approx \bar{S}_{ab} = \langle \phi'^{N}_{A} | \phi'^{N}_{D} \rangle \tag{5.2}$$

where S_{ab} is the overlap of the SOMOs of the donor and the acceptor in the full SCF basis set and $\bar{S}_{ab}$ is the overlap of the SOMOs in the reduced basis set. Eq. (5.2) was calculated using the analytic integral formulae published by Mulliken [113]. With these formulae, the overlap of Slater orbitals with different quantum numbers at different separation can be calculated. This reduced basis set and the integral formulae allow a very fast overlap calculation in terms of atomic orbital overlaps between a relatively small number of orbitals which will be compared to the other methods in Fig 4.5.

The final question was how to parameterise Eq. (5.1) to give the best possible result. For this reason, several reference calculations were done using the DFT method on a training set of π-conjugated donor-acceptor systems. The derived parameters were then tested on π-conjugated molecules outside the training set. I found that Eq. (5.1) with a single parameter C can describe well the electronic coupling of all molecules investigated, but only if the exponents of the minimum STO basis set are properly chosen. This led to a speed-up of approximately 6 orders of magnitude compared to DFT calculations, with little loss of accuracy [114].

5.1 Theory

The overlap and the electronic coupling H_{ab} are calculated between the diabatic electronic wavefunctions for the initial and final electron transfer (ET) states, referred to as $|\psi_a\rangle$ and $|\psi_b\rangle$. If the correlation between the overlap and electronic coupling stands it should be valid for any given geometry of a donor-acceptor pair and for a wide range of π-conjugated donor and acceptor molecules. Depending on the level of theory, calculation of the exact overlap can be computationally demanding: if one wants to include bulk behaviour, the diabatic wavefunctions can be approximated by Kohn–Sham determinants obtained from charge constrained DFT calculations (Refs [68, 74, 115, 116]). Therefore, several approximations were applied to speed up the calculation of S_{ab}. Firstly, similarly to FODFT it is assumed that the ET is mediated by only two orbitals, the SOMO of the isolated reduced donor fragment, $|\phi'^{N}_{D}\rangle$, and the SOMO of the isolated reduced acceptor fragment, $|\phi'^{M}_{A}\rangle$ (notation as in Refs [45] and [68]). The overlap is approximated as the zeroth order component of the Taylor expansion of the Hamiltonian

$$H_{ab} = \langle\psi_a|\hat{H}|\psi_b\rangle \approx \tilde{C}\langle\psi_a|\psi_b\rangle \approx C\langle\phi'^{N}_{D}|\phi'^{M}_{A}\rangle. \tag{5.3}$$

The SOMO, obtained from a quantum chemical calculation on the isolated monomer denoted as $|\phi'^{N}_{D}\rangle$ is projected onto the smaller STO basis set ($|\tilde{\phi}'^{N}_{D}\rangle$).

$$|\phi'^{N}_{D}\rangle \approx |\tilde{\phi}'^{N}_{D}\rangle = \sum_{i}^{n} c_i|\chi_i\rangle \tag{5.4}$$

where c_i is the expansion coefficient of the respective Slater orbitals and n is the total number of Slater orbitals on the acceptor atom, running through all the orbitals of

a given atom and every atom of the acceptor molecule.

$$c_i = \sum_j^n S_{ij}^{-1} \langle \chi_j | \phi'^N_D \rangle \tag{5.5}$$

Here, $S_{ij} = \langle \chi_i | \chi_j \rangle$ is the overlap matrix of the Slater type atomic orbitals. The Slater orbitals are constructed by taking the product of spherical harmonics and a radial function where the radial part is given as

$$R_{n,l}(r) = N_{n,l} r^{n-1} \mathrm{e}^{-\mu_{n,\alpha} r / a_\mathrm{H}}. \tag{5.6}$$

Here $\mu_{n,\alpha}$ is the Slater coefficient that depends on the atom type α, the principal quantum number n and angular quantum number l; and $N_{n,l}$ is a normalisation factor. In Eq. (5.6) the Slater coefficient is normalised with the Bohr radius a_H. To avoid confusion, this work terms the Slater coefficient as $\mu_{n,\alpha}/a_\mathrm{H}$.

Since organic molecules are the main focus of our work and all of the examined systems comprised second row atoms only, the main focus will be on sp^2 C atoms.

The p_i $(i = x, y, z)$ orbitals of each ion are projected onto a locally defined $\{p_{\sigma 1}, p_{\sigma 2}, p_\pi\}$ atomic basis set. The p_π directions are determined by the nearest neighbours of the atom on which it is centred. In the case of sp^2 hybridised carbons, this means three connected atoms. These three neighbours determine a plane and the normal vector of this plane is the chosen p_π direction. Since heteroatoms can participate in the delocalised π system (*e.g.* ethers or pyrrole) in those cases, the plane is determined by the two neighbouring atoms and the heteroatom itself. The SOMO is approximated as

$$|\tilde{\phi}'^N_D\rangle \approx |\bar{\phi}'^N_D\rangle = \sum_i^N c_{p_\pi^i} |p_\pi^i\rangle, \tag{5.7}$$

where

$$c_{p_\pi^i} = \sum_{j=x,y,z} c_{p_j^i} \langle p_\pi^i | p_j^i \rangle. \tag{5.8}$$

In this final step, the orbital is defined by the p_π orbital directions which are defined in the internal coordinate system of the nuclei of the molecule. Therefore, the $C_{p_\pi^i}$ coefficients are invariant with respect to the rigid rotation of the nuclear frame. The steps of the projection are illustrated in Fig. 5.1.

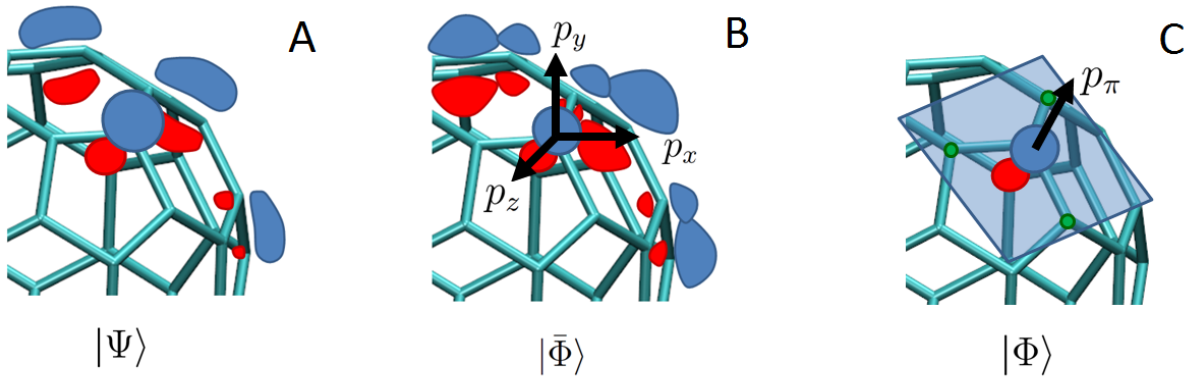

Figure 5.1: This figure illustrates the steps of the projection of the SOMO onto the p_π orbitals of the minimum Slater basis set. Panel A represents the SOMO obtained directly from the SCF calculation. Panel B shows the projected STO orbitals in the Cartesian coordinate system. Panel C shows the projected rotationally invariant orbital definition, where the orbital is expanded by the p_π orbitals (shown on a single C atom).

After the final step of the projection, the orbitals have to be renormalised ,

$$|\bar{\phi}_D^N\rangle = \frac{\bar{\phi'}_D^N}{\sqrt{\langle \bar{\phi'}_D^N | \bar{\phi'}_D^N \rangle}}. \tag{5.9}$$

The overlap with other molecules is calculated with the renormalised coefficient set.

For the overlap calculation, the projected orbitals and the analytical integral formulae provided by Mulliken [113] are used. For a given molecular dimer, the integral is calculated as a sum of atomic overlaps

$$\bar{S}_{ab} = \langle \bar{\phi}_D^N | \bar{\phi}_A^M \rangle = \sum_{i \in D}^{\text{atoms}} \sum_{j \in A}^{\text{atoms}} c_{p_\pi^i} c_{p_\pi^j} \langle p_\pi^i | p_\pi^j \rangle \tag{5.10}$$

To simplify the integrals, a local basis set is defined for each atom pair. The choice of the local basis set is semi-trivial. One of the axes is the vector pointing from one atom to the other (we chose this to be the z axis). The y axis is determined by an arbitrary vector that is orthogonal to the z axis, and the x direction is constructed as the cross product of the other axis vectors. The $\{p_\pi\}$ orbitals of the atoms are projected onto this local basis set

$$|p_\pi^i\rangle = \hat{c}_{x,i}|p_{x_{\text{loc}}}\rangle + \hat{c}_{y,i}|p_{y_{\text{loc}}}\rangle + \hat{c}_{z,i}|p_{z_{\text{loc}}}\rangle. \tag{5.11}$$

The overlap integrals for each atomic pair can be defined as the sum of p_π and p_σ overlaps at different nuclear separations R. The formulae also depend on the Slater coefficients presented in Eq. (5.6) which differ for different quantum numbers and elements [113]. The overlap is then

$$\langle p_\pi^i|p_\pi^j\rangle = (\hat{c}_{x,i}^*\hat{c}_{x,j} + \hat{c}_{y,i}^*\hat{c}_{y,j})S_{p_\pi}(r, \mu_p^i, \mu_p^j) + \hat{c}_{z,i}^*\hat{c}_{z,j}S_{p_\sigma}(R, \mu_p^i, \mu_p^j), \tag{5.12}$$

where μ_p^i and μ_p^j are the Slater decay coefficients of the p orbitals on atoms i and j respectively.

It is easy to see that both the projection and the overlap calculation depend on the Slater coefficients. There are many ways to calculate these coefficients for different elements including the original method of Slater [117] and a more recent approximation by Clementi *et al.* [118]. However since the basis set is small, μ was kept as a parameter which was optimised to maximise the completeness (Eq. (5.9)) of the projection and minimise the error in the electronic coupling calculation.

5.2 Training and test sets for the parameterisation of the overlap method

Firstly, to tackle the issue of the fitted parameters, a sufficiently broad set of molecules had to be chosen. Since the HAB11 database [68] has been already tested with various methods of coupling calculation it proved to be a good starting point. It contains a variety of π-conjugated molecules to calibrate and test the Slater coefficients μ and the conversion factor C.

The positively charged HAB11 set consists of a series of stacked π-conjugated systems which contain heteroatoms: oxygen, nitrogen, and sulphur. These molecules are the building blocks of many semiconducting materials (*e.g.* thiophene for PBTTT [19]), yet small enough for calculation of H_{ab} at high levels of *ab initio* theory. Since there were only a few data points that had SOMO contribution on the heteroatoms these were omitted from the basis set. These molecules would have provided an insufficient basis set for calibrating the Slater coefficients for the heteroatoms. Therefore the set was reduced to the seven molecules which had density on the carbon atoms only. These were ethylene, cyclobutadiene, cyclopentadiene, benzene, pyrrole, furane and thiophene. The configuration was the same for all seven molecules, π-stacking with an enforced mirror plane between the monomers. The couplings were calculated at different stacking distances given by 3.5, 4.0, 4.5 and 5.0 Å. In the following, this data set is referred to as **HAB7**.

The **acenes** data set was used to investigate the size dependence of the π-conjugated system. A series of positively charged polyacenes were used increasing in size from naphthalene to pentacene. The dimer structure was similar to the one applied for the HAB7 set, π-stacked using the same stacking distances.

In order to test the effects of different configurations, a data set of fifteen randomly oriented positively charged **thiophene** dimers was also analysed at different

distances. These configurations tested the effects of different intermolecular orientations.

As the analytic overlap method is less size-limited, larger molecules can also be implemented in the test set. Since the focus in this piece of work is on organic semiconductors, fullerenes are used both for parameter calibration and testing. The set termed **C60** was created by choosing three rotationally different negatively charged C_{60} dimers and calculating the coupling at seven different centre-to-centre distances from 9 to 15 Å (Fig. 5.2), creating a set of twenty-one dimers.

Another set of negatively charged C_{60} molecules consisted of twenty equidistant rotationally different dimers chosen from the $\sim$ 27000 published in Ref [45]. The separation of the dimers was set to 10.1 Å. This data set is termed **C60R**.

A series of dimers from the monoclinic and triclinic PCBM structure were also included for which the coupling values were calculated in the reduced state in an earlier publication [5, 49]. PCBM is about the size limit of our chosen reference method: FODFT. This data set is denoted as **PCBM**.

Another important aspect of these last three data sets is the curvature in the molecular structure. Unlike the other test molecules, C_{60} and PCBM are not flat. The radial component of the HOMO is not symmetric with respect to the surface of the buckyball; the lobe outside the cage is slightly larger than the lobe inside the cage. This implies a non-negligible contribution from the $2s$ orbital on each C atom in addition to p_π.

So far all the data sets represented carbon systems. To expand the applicability the four **imidazole** configurations from HAB11 and a set of five positively charged stacked **porphins** were used to optimise the μ_p value for N.

Furthermore since the data set has been already tested with other methods in Chapter 4 the **HAB7-** set, consisting of negatively charged anthracene, tetracene, pentacene, perylene, perylene-diimide, perfluorinated anthracene, and prophin, is also added to the test sets (See Fig. 4.2), along with the six randomly oriented

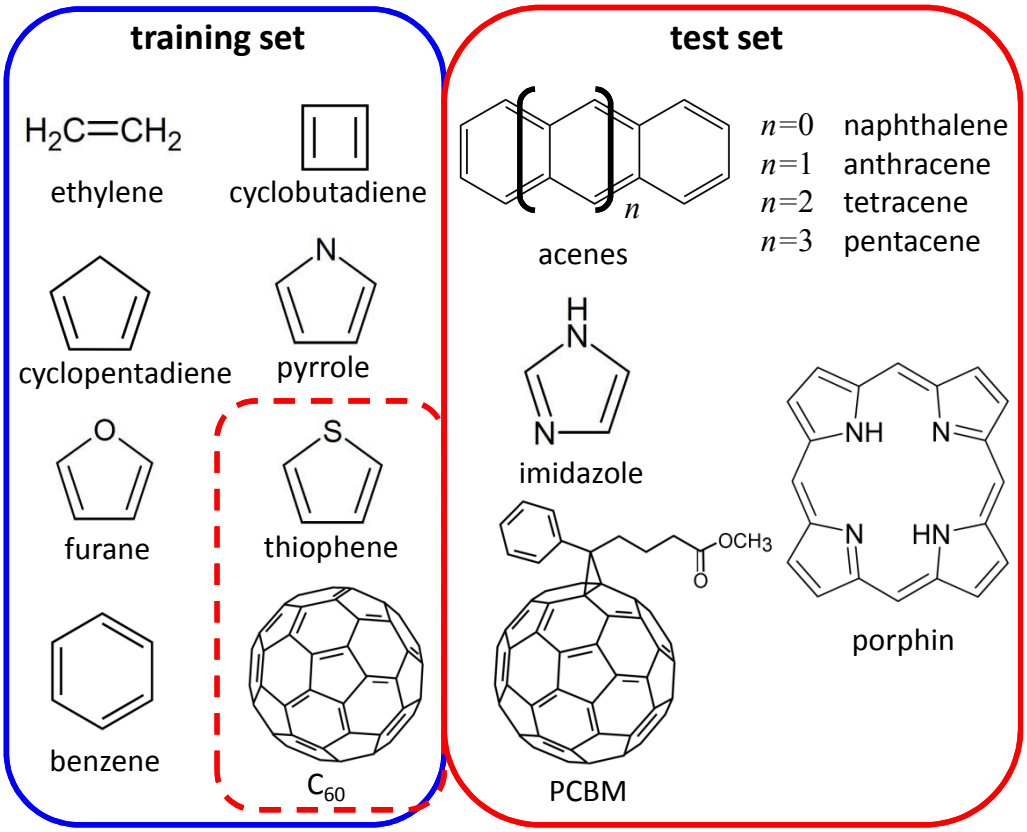

Figure 5.2: The arene, acene and fullerene compounds that were included in our coupling reference calculations. The blue frame marks the training set which was used to obtain the fitted parameters for Eq. (5.1). The red frame marks the test set which were used independently to test the generality of the fitted parameters. In addition, the HAB7- set shown in Fig. 4.2 and the randomly oriented anthracene molecules were also used as test sets.

negatively charged **anthracene** dimers from Chapter 4.

5.3 Computational details for reference coupling calculations and fast overlap method

The reference calculations were done with fragment orbital density functional theory. Although CDFT with 50% exact exchange gave the best results this is not feasible for systems as large as a PCBM dimer.

The simulation details were analogous to the ones presented in Chapter 4 for the

HAB7, the acenes, the tiophenes, and the porphin set. The structures of the HAB7, acenes, and thiophene datasets were taken from Ref. [68]. The C60, C60R, and the PCBM sets were also calculated using the CPMD code with 4 Å vacuum around the isolated dimers but the pseudopotentials were Goedecker–Teter–Hutter (GTH) type dispersion corrected atom centred pseudopotentials and Hockney type Poisson solver permitting a smaller box size. The basis set cut-off was slightly increased to 90 Ry as the GTH pseudopotentials are somewhat harder than the TM potentials used earlier. The convergence criterion for the Kohn–Sham orbitals was that the maximum component of the energy gradient had to be lower than 8.5×10^{-7} a.u. in order to converge the orbitals. The structures were taken from Ref [45] and Ref [49].

The FODFT coupling values were scaled by a factor of 1.3. This correction factor was obtained by comparing the FODFT values to MRCI+Q and NEVPT2 results for oxidised dimers [68], and similar correction factor was derived in the reduced state in Chapter 4. The corrected set is referred to as sFODFT. To make sure that the states were coupled consistently between the different methods, the NEVPT2 spin densities and the FODFT spin densities were compared by visual observation.

Before calculating the reference values, the available accuracy of the FODFT calculations were tested. While the numerical accuracy in the low coupling regime is not an issue for small molecules, where the coupling is in the order of several hundred meV, it becomes more important when C_{60} and PCBM is assessed. For the fullerene molecules the coupling values are lower and strongly depend on the relative orientation of the dimers [45]. The FODFT coupling accuracy is limited by the finite integration grid and the basis set cut-off. Testing several C_{60} dimers, the effect of rotating the entire dimer in the box resulted in a fluctuation in the coupling value of maximum 0.2 meV. This can be reduced by increasing the real space grid of the calculation. However, this increases the computational costs for larger box sizes significantly. Therefore, any data point below 0.2 meV was omitted. The problem likely arises from the pseudopotentials which are generated by creating

a spline fit on a cubic grid. This issue can be also seen in the C60 set. As the separation of the dimers r is increased, the H_{ab} values are expected exponential to decay as in Eq. (4.37), this strengthens the argument that the overlap provides a good approximation for estimating H_{ab} values according to Eq. (5.1). However as shown in Fig. 5.3 for C_{60} at $H_{ab} = 0.1$ meV the lines flatten. Thus the C60 set was reduced to 15 values only.

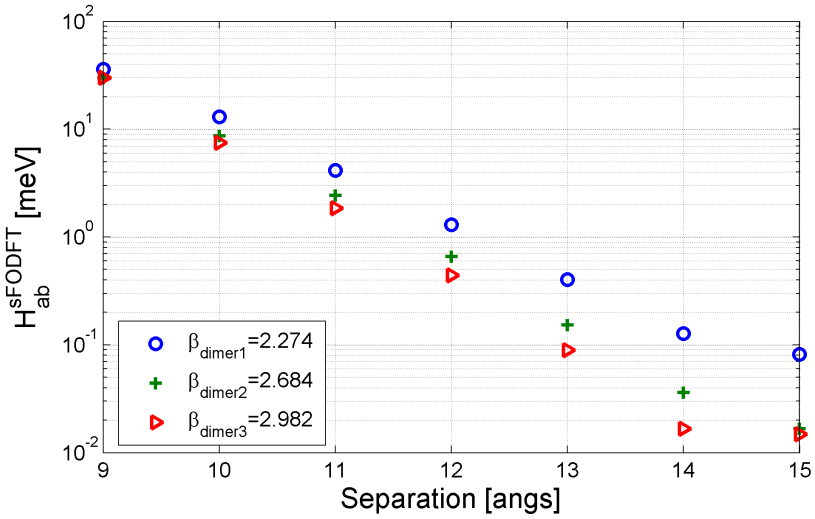

Figure 5.3: The electronic coupling decreases as a function of intermolecular distance r for three rotationally different C_{60} dimers.

Table 5.1: Analysis of the exponential decay constant of the overlap according to Eq. (4.37) and the R^2 value of the fitted lines.

$\beta/2$ [1/Å]	1.491	1.342	1.137
R^2	0.9979	0.9984	0.9995

The SCF calculations were done with the CPMD program package and the projection and overlap calculations were done with a Fortran90 routine I have coded. The plane wave Kohn–Sham orbitals were projected onto the minimum Slater basis set using the properties calculation toolkit of the CPMD program package. The output was read in by a Fortran90 subroutine and using the geometry information the orbital of interest was projected onto the $\{p_\pi\}$ orbitals. Another code reads in the

set of coefficients and the nuclear configuration. The orbitals are reconstructed on the nuclear frame and the Slater integrals are calculated as explained in Section 5.1.

Due to their degenerate SOMOs, benzene and the fullerene derivatives needed extra attention when doing the coupling calculation. The SOMO of C_{60}^{-} is identical to the LUMO of the neutral C_{60}, the orbital is three-fold degenerate and belongs to the T_{1u} irreducible representation of the I_h point group [119]. The excess charge does not break the symmetry significantly. In the Kohn–Sham calculations, the three-fold degeneracy for C_{60} and the 2-fold degeneracy for benzene is preserved to the accuracy of 10 meV. Although the electronic structure of $PCBM^{-}$ is similar to that of C_{60} the orbitals are slightly perturbed by the side chain, resulting in partially lifted degeneracy. The SOMO-LUMO separation is 40 meV and the LUMO LUMO+1 separation is larger than 100 meV. Therefore at room temperature PCBM is only 2-fold degenerate. The orbital coupling was consistent in the benzene, the $PCBM^{-}$ and the C_{60}^{-} cases. During the initialisation step, CPMD consistently localised the excess electron on the first atom in the code which resulted in the HOMO always having the same relative orientation compared to the atomic indices. Most importantly, the SOMO co-rotated with nuclear frame. This means that one set of orbital coefficients obtained for an isolated C_{60} or PCBM molecule was sufficient to describe all dimer configurations of those molecules.

5.4 Results and discussion

This section discusses the generality, accuracy and speed of the overlap method. In the first half, the test set is used to determine whether only one C parameter can be used to determine the H_{ab} for different molecules with Eq. (5.1) or not. In the second half, the focus is on the possible reduction of the basis set to a smaller one consisting of the $\{p_\pi\}$ orbitals only and on the accuracy which can be achieved with

this method. Finally, the computational demand of this method is compared to that of other methods discussed in Chapter 4.

5.4.1 Error calculations and reference calculations

According to Kubas *et al.*, the FODFT H_{ab} values of the HAB11 data set were in good agreement with NEVPT2+GMHT coupling values. The mean unsigned relative error was 37.6%. After applying a linear scaling factor of 1.3 this error went down to 17.6% for all three systems [68].

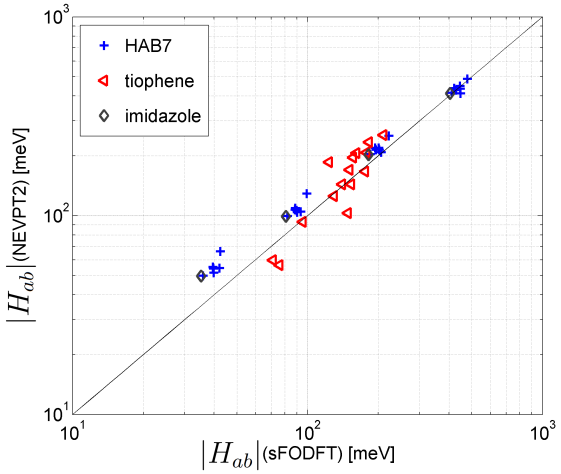

Figure 5.4: The correlation of the NEVPT2+GMHT coupling values with scaled FODFT results for three different data sets: HAB7, thiophene, and imidazole. The correlation is excellent for the stacked cases and slightly worse for the randomly oriented thiophene molecules.

The errors for the HAB7, the thiophene, and the imidazole data sets in Table 5.2 were analysed by calculating the mean relative unsigned error MRUE, the mean unsigned error MUE, and the maximum error MAXERR according to Eq. (4.36) as discussed in Chapter 4.

The results correspond to the trends published in Ref. [68]. As it can be seen the agreement for the HAB7 and the imidazole data sets, where the structures were stacked, was excellent with a mean unsigned relative error of less than 14%. The randomly oriented thiophene structures were less accurate with approximately 27%

Table 5.2: Correlation of the GMHT+NEVPT2 and sFODFT coupling values for HAB7, thiophene, and imidazole. MRUE, MUE, and MAXERR values were calculated according to Eq. (4.36).

set	MRUE [%]	MUE [meV]	MAXERR [meV]
HAB7	13.7	15.7	35.8
thiophene	26.6	48.2	94.4
imidazole	12.9	12.7	15.6

relative error (Fig. 5.4). Since the scaling factor 1.3 always decreased the error, sFODFT values were used as reference H_{ab} values.

5.4.2 Overlap method with DFT orbitals

The next step was to test the validity of Eq. (5.1) on the training and test systems. At first, the coupling values are compared to the real space integrals of the SOMO orbitals obtained by DFT using the full plane wave orbitals without any reduction of the basis set. Then, the proportionality between couplings calculated with FODFT and the projected minimum STO orbitals is discussed. Finally the two overlap values calculated with plane wave DFT orbitals and with projected STO orbitals are compared.

Since the calculated H_{ab} values cover several orders of magnitude ranging from 0.2 to 1000 meV, to represent the entire range the C60 and HAB7 sets were combined into a training set to fit the conversion factor C. It is expected that the MRUE would underestimate the error for small couplings. Therefore, in order to have a fairer assessment for the broad range the root-mean-square error of the logarithm was minimised as

$$\mathrm{ERMSLE} = \exp\left(\sqrt{\frac{1}{N}\sum_{i=1}^{N}\left(\ln\left|\frac{H_{ab}^{\mathrm{ref}}}{H_{ab}^{\mathrm{calc}}}\right|\right)_i^2}\right) \tag{5.13}$$

where H_{ab}^{ref} is the sFODFT coupling value and H_{ab}^{calc} was calculated as $H_{ab}^{\mathrm{calc}} = CS_{ab}$.

The maximum error was defined as

$$\mathrm{MAXUL} = \exp\left(\max\left(\ln\left|\frac{H_{ab}^{\mathrm{ref}}}{H_{ab}^{\mathrm{calc}}}\right|\right)\right). \tag{5.14}$$

The optimimum linear scaling factor obtained by minimising Eq. (5.13) was $C =$

Table 5.3: Errors of the calculated H_{ab} values using Eq. (5.1) with full SCF basis set compared to the sFODFT H_{ab} values. ERMSLE values give a rough estimate of the factor of the error therefore there are no units presented.

set	ERMSLE	MAXUL
training set	1.6	3.7
acenes	1.5	1.9
thiophene	1.7	2.5
C60R	1.8	8.2
PCBM	1.8	3.9
porphin	1.8	2.7
imidazole	1.4	1.7
HAB7-	1.5	2.7
anthracene	2.3	4.3

3.498 eV. The correlation was very good in the higher coupling regime but the errors became somewhat larger at the sub-meV level. However, it can be seen in Fig. 5.5 that despite the wide variety of molecules and the different errors, the different compounds matched the same line.

5.4.3 Projection on the STO basis set

The main question discussed in this section is whether the good correlation between the coupling and the overlap can be retained when the overlap S_{ab} calculated with the DFT orbitals is replaced by the overlap between the projected orbitals, $\bar{S}_{ab}$ as in Eq. (5.10).

Using the minimum STO basis set introduces data loss, therefore the effect on the orbital had to be assessed. In order to maximise the completeness of the projection, the Slater coefficient that described the $2p$ orbital of carbon μ_{2p}^{C} in the

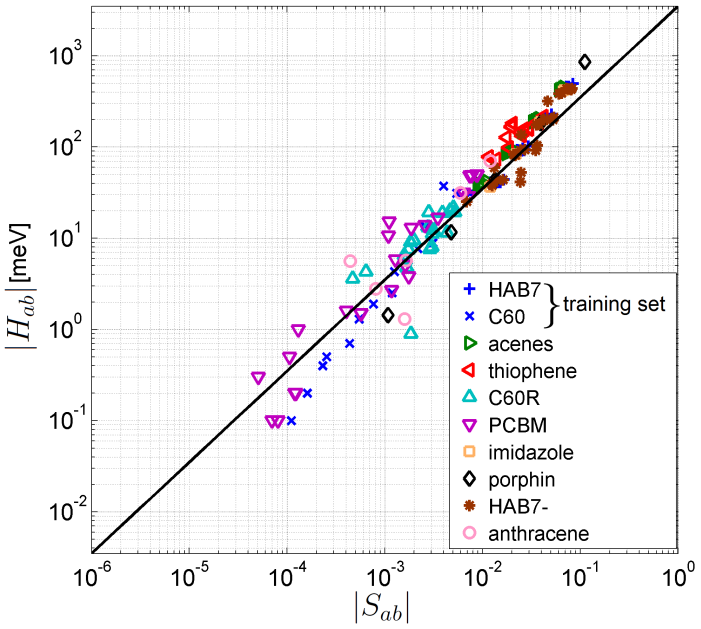

Figure 5.5: The correlation of the full SCF SOMO orbital overlaps with the scaled sFODFT coupling values. Using a different error definition to fit the line such as MURE would have resulted in a steeper line as the higher coupling values would have been included with a more significant weight.

CPMD code was optimised. In the original version of the code, $\mu_{2p}^{\mathrm{C}} = 1.5679$ bohr^{-1} was used which was calculated using the effective nuclear charges by Clementi [118]. However, for C_{60} the Slater coefficient that maximised the completeness was $\mu_{2p}^{\mathrm{C}} = 1.3125$ bohr^{-1}. This value produced more completeness for the molecules of the HAB7 set, though the μ_{2p}^{C} dependence was much weaker in this case [Table 5.4]. A similar analysis was performed for the nitrogen: the optimum Slater coefficient value was $\mu_{2p}^{\mathrm{N}} = 1.7$ bohr^{-1}. The effect of a larger Slater basis set on the complete-

Table 5.4: Different μ_{2p}^{C} values for the projection give different completeness (See Eq. (5.9)). The completeness of the monomers of the HAB7 set were averaged. The HAB7 set was not very sensitive tox changes in the Slater coefficient, but the C60 set had stronger μ dependency.

μ_p^C [bohr^{-1}]	1.0	1.1	1.2	1.3	1.4	1.5	1.6
$\|\|\tilde{\phi'}^N\|\|$ C_{60}	0.939	0.960	0.972	0.977	0.975	0.967	0.956
$\|\|\tilde{\phi'}^N\|\|$ HAB7	-	-	-	0.978	-	-	0.975

ness was also tested. For this, the $\{3s, 3p\}$ and $\{4s, 4p\}$ basis functions were added

to the minimum Slater basis set. The coefficients for carbon on these additional basis functions were in general two orders of magnitude smaller than the $\{2s, 2p\}$ coefficients, and the completeness did not change significantly.

Secondly, the effect of further projection to the $\{p_\pi\}$ basis set had to be determined. For the HAB7, acenes, imidazole and porphin data sets, the projected coefficients on the s orbitals and on the p orbitals perpendicular to the p_π-direction were < 0.001. However, both PCBM and C_{60} had some densities on the s orbitals, although even the largest s coefficient (0.015) was an order of magnitude smaller than the largest p coefficient (0.280). To test the effect of the s orbitals on the norm calculation, the basis set was increased to $\{s, p_\pi\}$. In this case, the projected orbital in Eq. (5.7) took the form of

$$|\tilde{\phi}'^N_D\rangle \approx |\bar{\phi}^N_D\rangle = \sum_i^N c_{s^i}|s^i\rangle + c_{p^i_\pi}|p^i_\pi\rangle. \tag{5.15}$$

The overlap instead of Eq. (5.10) was calculated as

$$\bar{S}_{ab} = \sum_{i\in D}^{\text{atoms}} \sum_{j\in A}^{\text{atoms}} c^*_{s^i} c_{s^j} \langle s^i|s^j\rangle + c^*_{p^i_\pi} c_{p^j_\pi} \langle p^i_\pi|p^j_\pi\rangle + c^*_{p^i_\pi} c_{s^j} \langle p^i_\pi|s^j\rangle + c^*_{s^i} c_{p^j_\pi} \langle s^i|p^j_\pi\rangle, \tag{5.16}$$

where the integrals in Eq. (5.12) became

$$\langle p^i_\pi|p^j_\pi\rangle = (\hat{c}^*_{x,i}\hat{c}_{x,j} + \hat{c}^*_{y,i}\hat{c}_{y,j}) S_{p_\pi}(R, \mu^i_p, \mu^j_p) + \hat{c}^*_{z,i}\hat{c}_{z,j} S_{p_\sigma}(R, \mu^i_p, \mu^j_p), \tag{5.17a}$$

$$\langle p^i_\pi|s^j\rangle = \hat{c}^*_{z,i} S_{p_\sigma - s}(R, \mu^i_p, \mu^j_s), \tag{5.17b}$$

$$\langle s^i|p^j_\pi\rangle = \hat{c}_{z,j} S_{s-p_\sigma}(R, \mu^i_s, \mu^j_p), \tag{5.17c}$$

$$\langle s^i|s^j\rangle = S_{s-s}(R, \mu^i_s, \mu^j_s). \tag{5.17d}$$

As shown in Table 5.5, adding the s orbitals only changed the completeness slightly.

Table 5.5: Orbital norms calculated with the analytic overlap program using SCF orbitals projected on the minimum STO basis set. The calculations marked with ^{s} included the s orbitals too while the unmarked overlap values only contain the p_π orbitals orthogonal to the plane of conjugation. $\langle||\tilde{\phi'}^N_D||\rangle$ refers to the mean of the norm while $\sigma\left(||\tilde{\phi'}^N_D||\right)$ is the standard deviation. The molecules of the HAB7 and acenes data set were unaffected by the inclusion as the s coefficients were 0.

set	$\langle\|\|\tilde{\phi'}^N_D\|\|\rangle$	$\sigma\left(\|\|\tilde{\phi'}^N_D\|\|\right)$
HAB7	0.988	0.0025
acenes	0.991	0.0004
C_{60}, PCBM	0.987	0.0224
C^s_{60}, PCBM^s	0.991	0.0224

5.4.4 Overlap method with the STO basis set

As was shown in the previous section, a very good completeness can be achieved with the STO basis set. However, the question is how this affects the overlap. It is easy to see that a Slater coefficient which gives good completeness might capture well the electronic structure closer to the nuclei, but that part of the orbital has little effect on the overlap, unlike the exponential tail of the STO basis functions. The aim was to derive a correlation plot similar to Fig. 5.5 between the electronic couplings calculated with FODFT and the analytical overlap integrals calculated with the minimum STO basis set. The same training set was used for this fit and similarly the ERMSLE of the logarithm was minimised (See Eq. (5.13)), however in this case the Slater coefficient was optimised as well to improve the fit.

$$H_{ab} = \bar{C}\bar{S}_{ab}(\mu) \tag{5.18}$$

where $\bar{S}_{ab}$ is the overlap calculated with the SOMO orbitals expanded in the $\{p_\pi\}$ basis set (See Eq. (5.10)). The best fit was $\mu^{\mathrm{C}}_{2p} = 1.0$ bohr^{-1} with the conversion factor $\bar{C} = 1.819$ eV (Table 5.6). This Slater coefficient is much smaller than the aforementioned Clementi–Raimondi value of 1.5679 bohr^{-1} It is worth noting that the $\bar{C}$ parameter is very sensitive to the small changes in μ. This is the reason why the

optimum $\bar{C}$ value is much smaller than other published values [48, 111]. The reason behind the small decay coefficient could be that at our typical interatomic distances (3 to 8 Å) this decay coefficient represents the orbital shape better.

Table 5.6: Different μ_{2p}^{C} values around the best fitted μ_{2p}^{C} and the conversion factor $\bar{C}$ which approximates best the sFODFT coupling values according to Eq. (5.18). Relative and logarithmic errors calculated according to Eq. (4.36) and Eq. (5.13) respectively.

μ_p^{C} [bohr^{-1}]	ERMSLE	MRUE [%]	$\bar{C}$ [meV]	R^2
0.90	1.58	39	1095	0.97
0.95	1.48	32	1418	0.98
1.00	1.45	30	1819	0.98
1.10	1.63	91	3295	0.97

Including the s orbital in the SOMO of C_{60} had a negligible effect on the accuracy of the integral (Table 5.7).

Table 5.7: Different μ_{2s}^{C} values and the corresponding ERMSLE values on the training set comparing approximate coupling values calculated with Eq. (5.18) to sFODFT reference values. The effect of the s orbitals is much smaller compared to the p orbitals. The value of the conversion factor was not affected by the larger basis set. All values are in bohr^{-1}.

μ_p^C \ μ_s^C	0.90	1.00	1.10	1.70
1.0	1.45	1.43	1.45	1.45

The Slater coefficient μ_{2p}^{N} was optimised using the porphin and imidazole sets. The ERMSLE was minimised by varying the μ_{2p}^{N} value, keeping the conversion factor as 1819 meV. The optimisation resulted in $\mu_{2p}^{\mathrm{N}} = 1.5$ bohr^{-1}.

The analytical coupling values for all the other sets were calculated with these μ and $\bar{C}$ parameters as shown in Fig. 5.6 and a similar error analysis to the one in section 5.4.2 was performed in Table 5.8.

Using μ_p^{C}=1.0 bohr^{-1}, the analytically calculated $\bar{S}_{ab}$ values were plotted against the full real space plane wave integral S_{ab} values. One can clearly see the effect of the reduced Slater coefficient in Fig. 5.7: the slope on the logarithmic plot is roughly 0.76. This value corresponds well to the ratio between the Slater coefficient used for

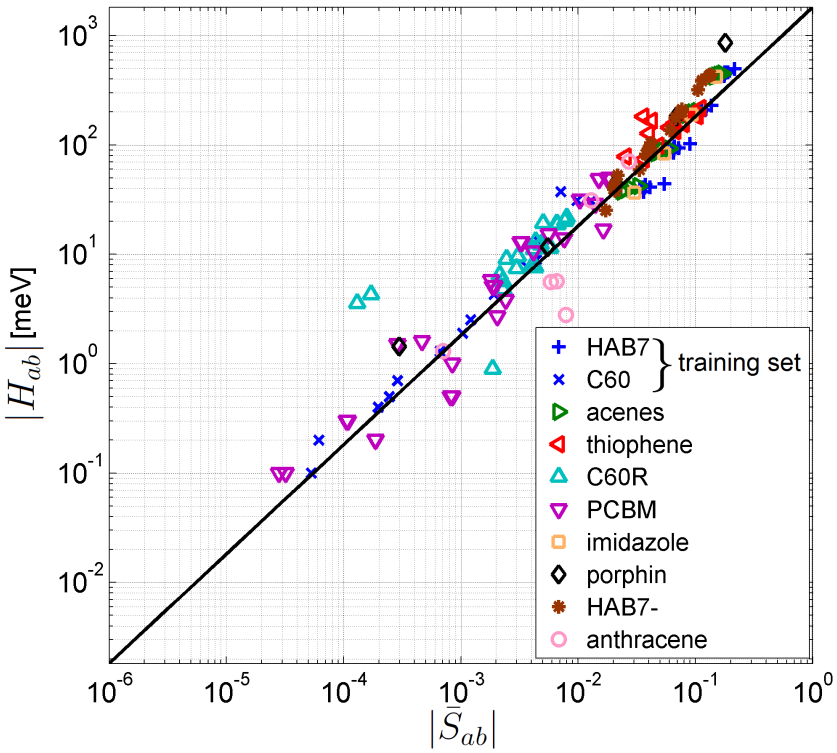

Figure 5.6: The correlation of analytically calculated orbital overlaps using the p_π orbitals from the minimum STO basis set with the scaled sFODFT coupling values.

Table 5.8: The errors of the analytically calculated $\bar{H}_{ab}$ values compared to the sFODFT H_{ab} values. ERMSLE and MAXUL values give a rough estimate of the factor of the error therefore these values are unitless and were calculated according to Eq. (5.13) and Eq. (5.14).

set	ERMSLE	MAXUL
training set	1.4	2.9
acenes	1.3	1.6
thiophene	1.5	2.8
C60R	2.7	15.7
PCBM	1.8	3.0
porphin	1.9	2.6
imidazole	1.4	1.5
HAB7-	1.5	1.9
anthracene	2.2	5.1

the overlap calculation (1.000 bohr^{-1}) and the Slater coefficient used for the orbital projection (1.3125 bohr^{-1}). It is important to point out that the thiophene and the randomly oriented C60R set matches the fitted line better on the S_{ab} vs. $\bar{S}_{ab}$ plot

than on the H_{ab} vs. $\bar{S}_{ab}$ plot. This means that the loss of accuracy in the case of the non-stacked structures is arising from the approximation of Eq. (5.1) rather than the reduced basis set.

In this case, the STO basis set gave relatively small errors and for certain systems

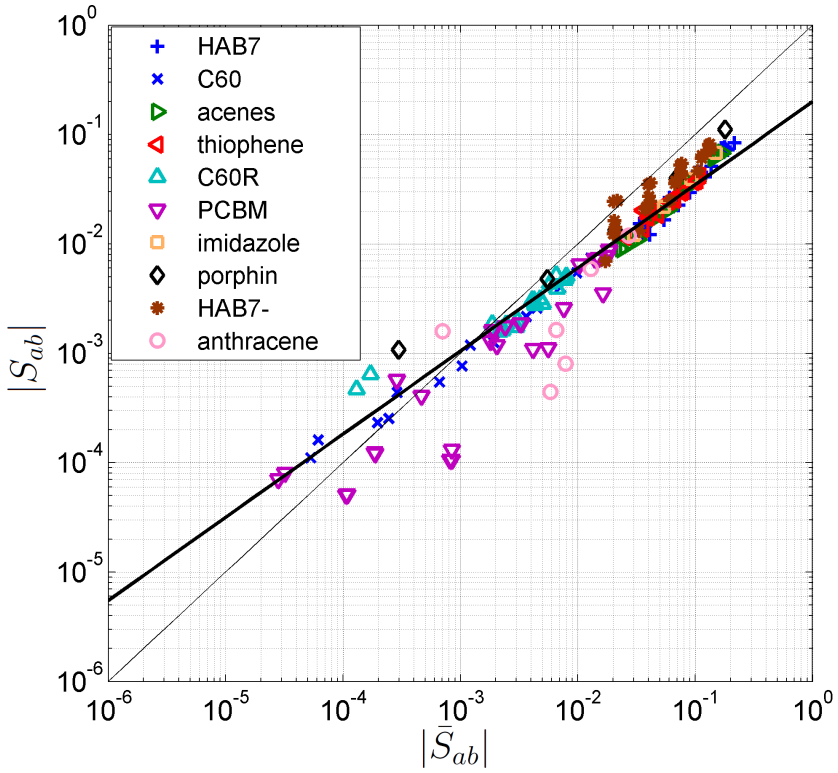

Figure 5.7: The correlation of analytically calculated orbital overlaps in the minimum STO basis set with the full plane wave basis set overlap values for different molecules.

even smaller errors than the full plane wave overlap calculations. This is due to the additional optimised parameter, the Slater coefficient.

The side chain has an important role in the packing order of PCBM but its electronic role in the charge transport is negligible. The butyric acid methyl ester chain consists of sp^3 carbons and while the non-bonding electron pair of the oxygen might have some small effects on the transport the SOMO orbital is mostly on the C_{60} cage and has a negligible contribution from the elements of the side chain. Therefore, in order to speed up the coupling calculations, the side chains are often

ignored [120]. However, in the monoclinic case there were three dimers where the phenyl group had a non-negligible role in mediating the coupling. In all three cases, the centre to centre distance of the C_{60} cage was rather large (around 12 to 13 Å) but the phenyl-groups were in a position where they were stacked with one another or with the C_{60} cage proving to be non-negligible in those special cases (Table 5.9).

Table 5.9: Overlap values in the full SCF plane wave and the reduced minimum STO basis set for PCBM with and without including the phenyl group for different configurations, denoted as S_{ab}, $\bar{S}_{ab}$ and $\bar{S}'_{ab}$ respectively. It can be seen that for the configuration with no stacking the effect is negligible but for those where there is phenyl stacking the effect is significant.

dimer	H_{ab} [meV]	S_{ab}	$\bar{S}'_{ab}$	$\bar{S}_{ab}$
phenyl-C_{60} stacking	1.0	1.3×10^{-4}	5.0×10^{-5}	8.4×10^{-4}
phenyl-C_{60} stacking	1.6	4.1×10^{-4}	5.1×10^{-5}	4.6×10^{-4}
phenyl-phenyl stacking	0.5	1.1×10^{-4}	2.5×10^{-5}	8.1×10^{-4}
no stacking	1.5	5.7×10^{-4}	2.9×10^{-4}	2.9×10^{-4}

In order to account for those special cases, all coupling calculations were performed including the C_{60} cage and the phenyl group but omitting the butyric acid side chains for every PCBM dimer.

5.4.5 Speed-up of coupling calculations

The main benefit of the fast overlap method compared to higher level methods is the speed of the calculations. The estimated coupling values are in good agreement with the reference values. By using this approximation, it is possible to investigate H_{ab} in systems that are large enough to represent the static and dynamic disorder in organic semiconductors. This way the couplings can be calculated on the fly during non-adiabatic molecular dynamics simulations. Coupling analysis also helps to decide which transport model can be applied on a given system.

The example of the $\sim$ 27000 C_{60} coupling values from Ref. [45] illustrates well how much faster the calculations are done with the analytical overlap program: while the FODFT calculations took approximately 2 months on 512 cores, the fast overlap

program calculates these values in 87 seconds on a single node. This is excluding the SCF step calculating and projecting the SOMO orbital on a single minimised C_{60} molecule which takes 20 minutes on 512 cores. As expected, the fast overlap method scales better with time than any other method discussed in Chapter 4 as can be seen in Fig. 5.8.

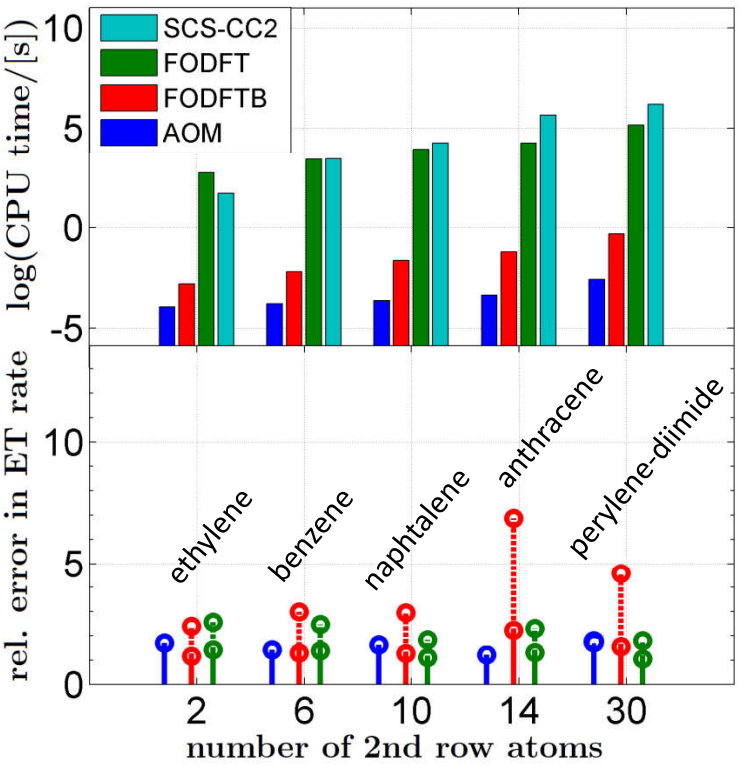

Figure 5.8: CPU time of different coupling calculation methods for different molecules and the error compared to the GMHT with SCS-CC2 reference values. The colour coded stems refer to the mean unsigned relative error Eq. (4.36); the solid stems show the scaled errors using the uniform scaling factors from Table 4.2; while the dashed stems show the actual relative error of different methods. The analytic overlap method is abbreviated as AOM on this plot.

It is worth mentioning that the comparison was done for the p_π-only overlap calculations. While s orbitals had non-zero contribution to the SOMO of C_{60} and PCBM sets their effect on the overlap was negligible. However, as the complexity of the formulae increased a significant overhead appeared in the calculation increasing the calculation of the coupling for a single C_{60} dimer from 0.003 s to 0.03 s.

5.4.6 Conclusions of the overlap method

It was demonstrated in this section that the linear relation of Eq (5.1) gives a good approximation to electronic coupling matrix elements between π-conjugated organic molecules in the range relevant to electron transport in the condensed phase (5 to 500 meV). A linear relation has been derived for single donor-acceptor pairs before, but here it is shown that a very diverse set of donor-acceptor pairs including stacked acenes, arenes with S, N, and O heteroatoms, and buckyballs can be described with a single proportionality constant. Most importantly, this linear correlation is retained or can be even improved if the overlap is calculated in terms of a minimum STO basis set with optimised Slater decay coefficients. Gaussian type orbitals would have been alternative method to use the analytic overlap method however using minimum STO basis set in combination with the projection to the p_π orbitals saves memory by using a single basis function per atom. While the integral formula is in general more complicated for slater type orbitals then it is for GTO the atoms which contribute the most to the couplings are mostly C atoms and for the same atom type the analytic integral formula is considerably simple [113].

This also provides a tool to estimate electronic couplings analytically, leading to speed-ups of around 6 orders of magnitude compared to standard DFT calculations for molecules typically used in molecular OSCs. Together with a fast estimator for site energies using for example polarisable or non-polarisable force fields, this scheme provides the basis for a fast yet reasonably accurate estimation of the electronic Hamiltonian that can be used in NAMD simulations of charge transport in OSC materials.

5.5 Analysis of heme systems with the overlap method

An extensive study was presented on the analytic overlap method in the previous section but the influence of thermal fluctuations on electronic couplings was not discussed. As the method is only fast if we have a set of coefficients obtained from SCF calculation, this can be an issue when the AOM is used in molecular dynamics simulations. Since during MD the molecules are not rigid, obtaining a set of coefficients for every molecule in every snapshot could introduce a significant overhead. In this section, the effects of thermal fluctuations on H_{ab} are discussed on various heme systems. An idealised set of coefficients were obtained from the minimised structure and were tested against FODFT results using the AOM on a molecular dynamics trajectory of three different heme systems.

5.5.1 Structures

Molecular dynamics trajectories of two deca-heme systems extracted from multi-heme cytochromes MtrC and its homologue MtrF were used for these calculations. MtrC can be found in the outer membrane of *Schewanella oneidensis*. *S. oneidensis* is an example of a dissimilatory metal reducing bacteria: in anaerobic environments they use extracellular insoluble transition metal oxides as terminal electron acceptors in their respiratory chain, such as manganese oxide [79]. Finally, the small tetra-heme cytochrome STC is investigated, which also functions as ET protein in *S. oneidensis* [121]. The three heme systems can be seen in Fig. 5.9.

Structures for MtrF, MtrC and STC were taken from molecular dynamics trajectories reported in Refs. [79], [80] and [122], respectively.

From each trajectory, 25 snapshots were extracted, separated by 1 ns. The hemes were extracted according to the methodology discussed in Ref. [79] including the axial

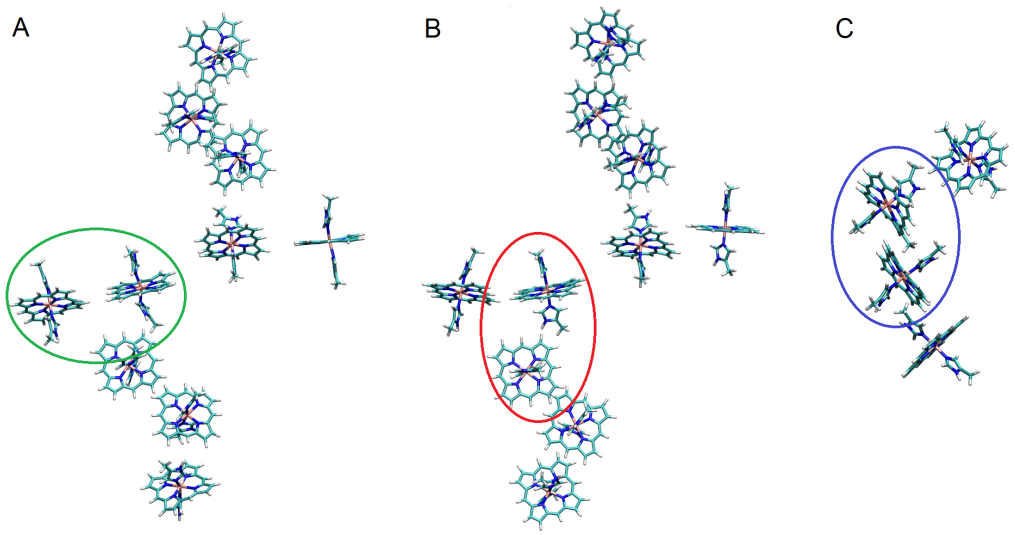

Figure 5.9: Multi-heme systems extracted from MtrF (Panel A), MtrC (Panel B), and STC (Panel C) protein SCF minimisation of the protein structure deposited in the data base. The environment of the multi-heme structure is not visible on the panel and did not participate in the electron structure calculations but was involved in the molecular dynamic simulation. The molecular dynamics calculations were done on the entire protein structure in water. For the coupling calculations the prophirin rings were extracted from these trajectories as in [79]. The blue circle denotes a stacked dimer structure. The red circle shows a T-shaped structure and the green circle is around a coplanar structure.

histidines but excluding all substituents of the porphin ring. The dimer structures were analysed according to stacking structure, Fe-to-Fe interatomic distance, and edge-to-edge distance. The edge-to-edge distance was calculated by identifying the nearest π-conjugated carbon atoms of the two porphin rings. For the MtrF and the MtrC, eight heme pairs were identified for both structures for which the couplings were expected to be non-negligible. For the STC structure, three such pairs were found.

Three types of stacking are distinguished for these dimers: stacked, T-shaped, and coplanar. The type of stacking is in most cases reflected in the Fe-to-Fe and edge-to-edge distance ranges as can be seen in Table 5.10.

Table 5.10: Average Fe-to-Fe and edge-to-edge distance of the different types of heme dimers. The edge-to-edge distance was calculated using the smallest distance between the carbon atoms of the porphyrin rings. The numbers in the brackets show the maximum deviation from the average values for each stacking type.

	stacked	T-shaped	coplanar
$d_{\text{edge-edge}}$ [Å]	4.44(±1.4)	5.85(±0.56)	6.62(±1.45)
$d_{\text{Fe-Fe}}$ [Å]	10.49(±1.65)	11.76(±0.86)	13.75(±1.25)

5.5.2 Simulation details

Similarly to the previous section, the reference calculations were done with FODFT. The FODFT results for MtrF were taken from the publication Ref. [79]. The FODFT calculations for MtrC and STC were done analogously to Ref. [79], using PBE functional with a 130 Ry basis set cut-off and GTH type pseudopotential replacing the core electrons. The convergence criterion for the electronic gradient was 1×10^{-6} a.u. The box size for the isolated system calculations was identified by centring every dimer in the minimal possible box with a minimum of 4 Å of vacuum between the box wall and the outermost atoms of the molecules, and the longest minimal dimensions were chosen. Therefore, all calculations were done in the same box size with at least 4 Å of vacuum around the molecules. Thus, the MtrC FODFT calculations were done in a 32.2Å × 20.7Å × 20.5Å orthorhombic box and the STC box size was 32.3Å × 20.5Å × 20.5Å, also orthorhombic. All FODFT coupling values were multiplied with a c_{corr} polarisation correction factor, 1.7, derived in Ref. [79]; these results are referred to as cFODFT.

The convergence of the coupling matrix elements with respect to the reciprocal space plane wave cut-off (which is the basis set in plane wave calculations) was investigated for two configurations of a heme pair of MtrC. The results are summarised in Table 5.11. At 110 Ry, the absolute error for the smallest and largest H_{ab} were 0.1 and 0.3 meV respectively, relative to 130 Ry.

Analytic overlap method coupling results for porphin were discussed in the pre-

Table 5.11: cFODFT coupling values as a function of the plane wave basis set for assessing an optimal and sufficient basis set. Both couplings are from MtrC. Structure A is a coplanar dimer and structure B is a stacked dimer.

basis set cut-off [Ry]	H_{ab} A [meV]	H_{ab} B [meV]
150	0.10	2.12
130	0.11	2.03
110	0.24	2.32
100	0.27	2.64
90	0.55	2.77
80	1.30	3.87
70	1.68	4.09

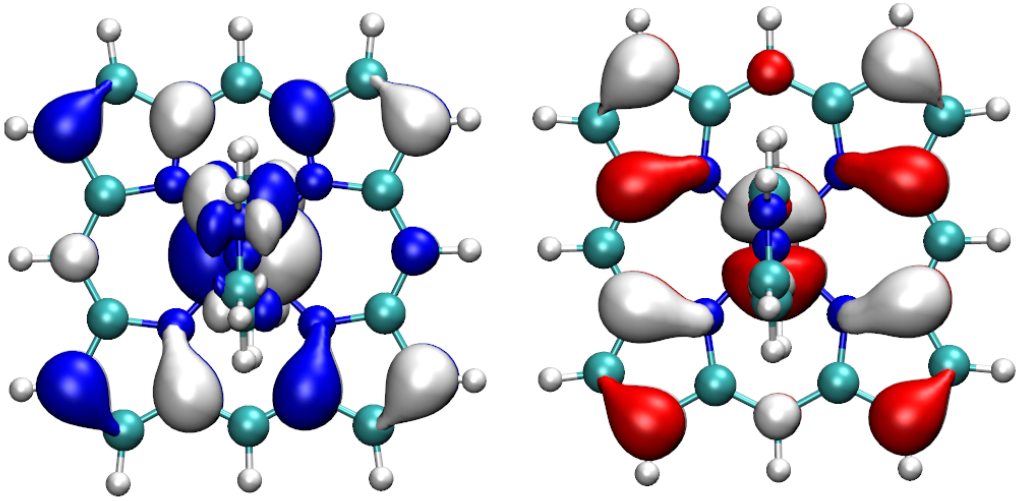

Figure 5.10: The SOMO and SOMO-1 orbitals on the perfect heme. They were identified by the orientation of the d orbital: the SOMO and the SOMO-1 always contain d_{xz} and d_{yz} where the direction z is along the axis formed by the histidine molecules.

vious section, but the heme molecules contain an iron core. In fact, the SOMO of the heme has a significant lobe on the Fe atom. If the SOMO is projected on the minimum STO basis set the completeness is 0.89, which is smaller than in the porphin case where the completeness was 0.96. If the Fe atom is omitted the projection results in a 0.3 completeness. Omitting the contribution of the Fe atom, the orbitals obtained for the AOM were normalised to $||\bar{\phi}^N||^2 = 0.3$. The Slater coefficients were $\mu_{2p}^C = 1.0$ bohr^{-1} and $\mu_{2p}^N = 1.5$ bohr^{-1}. The contribution from the s orbitals were negligible and, therefore omitted. The orbital expansion coefficients are obtained

from the SCF minimised idealised heme structure shown in Figure 5.10.

The expansion Eq. (5.4) can be generalised to include d orbitals, however this could result in a loss of computational speed while the precision may not be improved significantly. In this section, the analytic overlap method is tested against FODFT values for the three proteins, where the contribution of the d orbitals is omitted. This was motivated by the fact that in these systems the smallest Fe-to-Fe distance is larger than 9.4 Å and the $3d$ Clementi–Raimondi coefficient is 3.7 bohr^{-1} for Fe. This is more than twice as much as the C $2p$ coefficient by Clementi [118]. Therefore, the overlap of the Fe-d orbitals of one porphyrine molecule with any atom of the other porphyrine is expected to be negligibly small.

Another issue arises from the degeneracy of the hemes. Fig. 5.10 depicts the SCF minimised heme molecules and the two-fold degenerate SOMO and SOMO-1. During the calculations, the orbitals were identified by the contribution on the d_{xz} and d_{yz} orbitals where the z direction was along the axis determined by the histidine molecules. However, during the MD the nuclear frame distorts and the degenerate orbitals mix. Degenerate systems were presented in the previous section as well: for benzene and C_{60} one orbital was chosen and was consistently used in the calculations. In this case, the degeneracy cannot be circumvented as during molecular dynamics each state is equally likely to be occupied and the states can mix due to dynamic effects.

In order to overcome this issue, instead of comparing the couplings individually like in the case of benzene and C_{60}, the root-mean-square averages are compared. According to Newton [123], if the coupling is not too strong an effective coupling can be defined using the root-mean-square average of the possible coupling values.

$$\text{RMS}(H_{ab}) = \frac{1}{\sqrt{N}_{\{\phi\}}} \sqrt{\sum_{i,j\in\{\phi\}} H_{ij}^2}; \qquad \{\phi\} = \{\text{SOMO}, \text{SOMO}-1\}. \tag{5.19}$$

All four possible coupling values are calculated for every snapshot of every dimer

with cFODFT and same is done with AOM couplings. Then, the four coupling values are root-mean-square averaged according to Eq. (5.19) for both methods. These averaged H_{ab} and $\bar{S}_{ab}$ values are compared.

The degeneracy also affects the accuracy of the cFODFT calculations. The maximum fluctuation for the same configuration was found to be 0.5 meV in the coupling depending on the diagonalisation method when the Kohn–Sham energies were calculated according to Lánczos or Davidson and based on the initial state. This is possibly due to the slight fluctuations in how the SOMO and SOMO-1 mixes for heme dimers.

5.5.3 Results and discussion

Fig 5.11 depicts the correlation between the analytic overlap and the FODFT coupling values. For all three proteins the RMS(H_{ab}) and RMS($\bar{S}_{ab}$) showed a much wider spread than for the systems presented in Section 5.1. The three types of stackings are clearly distinguishable with the exception of one T-shaped heme pair in the STC system which showed high couplings, both with the AOM and the FODFT method, resulting in coupling and overlap values which are closer to the lower end of the stacked values. It can be seen that most of the coplanar values were below the accuracy of the cFODFT method, here the correlation curve flattens. On the other hand, it seems that there is a large spread even for values above 0.5 meV. This is particularly prominent for the stacked values where similar overlap values seem to expand over two orders of magnitude.

On panel B, of Fig. 5.11, the three different systems can be seen: STC showed the largest coupling values while MtrF and MtrC showed similar coupling ranges (MtrC having higher values than MtrF with cFODFT but similar overlap values with AOM). The fitting method to derive a proportionality constant was the same as in Section 5.1 by minimising the ERMSLE according to Eq. (5.13). The results can be seen in Table 5.12 for the different heme systems and in Table 5.13 for all systems.

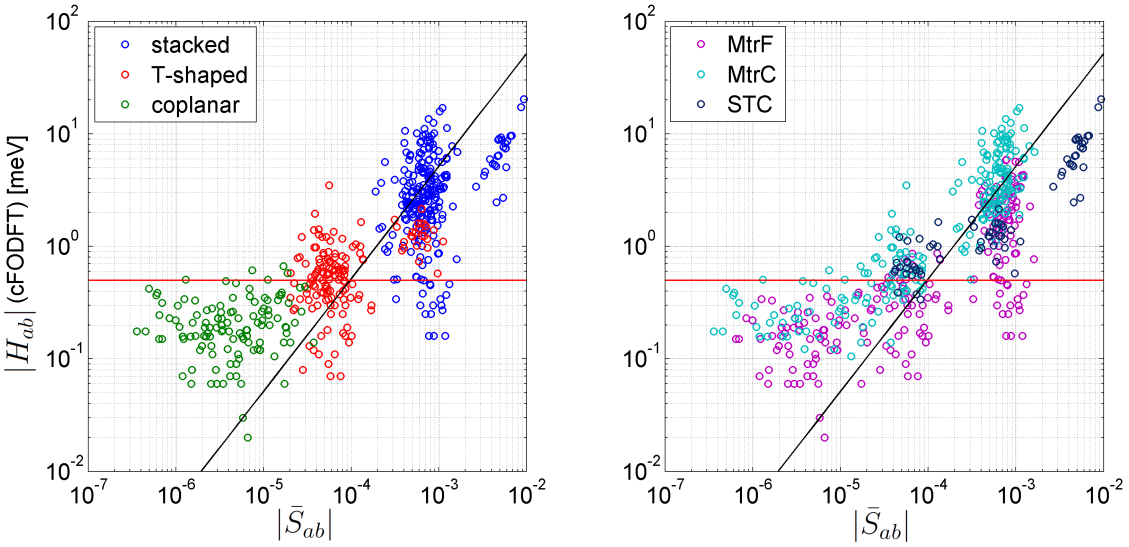

Figure 5.11: On panel A, the correlation between electronic coupling and analytic overlap values can be seen for the three different stacking types for MtrF, MtrC , and STC. On panel B, the same correlation can be seen for the three different multi-heme systems. The black line depicts the best fit. The red line marks the accuracy of the cFODFT results (0.5 meV). There is a significant variation in the coupling values even within the different stacking types.

Table 5.12: Proportionality constants for different cFODFT coupling and AOM overlap correlations for the different stacking types on their own and combined with other stacking types.

	MtrF		MtrC		STC	
	$\bar{C}$ [meV]	ERMSLE	$\bar{C}$ [meV]	ERMSLE	$\bar{C}$ [meV]	ERMSLE
stacked	2760	1.83	6308	1.80	1327	1.41
stacked+T	3252	2.06	7801	2.06	3019	2.67
all	3870	1.75	8152	2.15	3019	2.67

The constant of proportion $\bar{C}$ varies a lot for the heme systems depending on the geometry of the dimers, which makes it more difficult to find a single conversion factor to describe all dimers. The fitted values correspond to our observation: the smaller the couplings, the more likely that the analytic overlap method underestimates the values. As a consequence, if the smaller coupling values are included in the fit the correlation coefficient $\bar{C}$ becomes larger. It is interesting to note that for the STC stacked system where the couplings were the largest, the correlation coefficient

1327 meV is relatively close to the derived correlation factor in Section 5.1 for the arenes, acenes and fullerenes. The difference is significant for the MtrF and the MtrC systems: although the two systems have a similar structure the MtrC coupling values were higher than the MtrF ones by a factor of two.

Table 5.13: Proportionality constants for different cFODFT coupling and AOM overlap correlations including MtrF, MtrC, and STC in one fit. For some of the fits certain values were omitted based on the stacking type.

	Total	
	$\bar{C}$ [meV]	ERMSLE
stacked	3968	2.20
stacked+T	4890	2.48
all	5089	2.67

The large errors are probably partly due to the fact that the coupling values are rather small, very close to the accuracy of cFODFT. This does not explain the wide spread for the stacked values. In this form, the method is not best suited to deal with heme structures. The issue probably arises from the idealised heme coefficients being used to describe varied heme structures. Hemes are less rigid than the structures presented in Section 5.1 as the rotation of the axial histidine molecules have a significant effect on the orbital shape. This means that the SOMO and SOMO-1 cannot be described solely as a linear combination the SOMO and SOMO-1 of the idealised heme structure. An example of an MD snapshot orbital can be seen in Fig. 5.12, which shows an MD snapshot heme and the obtained SOMO and SOMO-1 orbitals with DFT. Although the d_{xz} and d_{yz} orbitals can still be identified, the SOMO on the porphyrine ring has a very different shape from the one presented in Fig 5.10. The resulting wavefunction fluctuation has a significant effect on the couplings therefore the idealised structures used for $\bar{S}_{ab}$ do not give a good approximation. In fact, even the distance dependence seems to show a better correlation.

The distance dependence of the coupling was analysed with cFODFT just like in

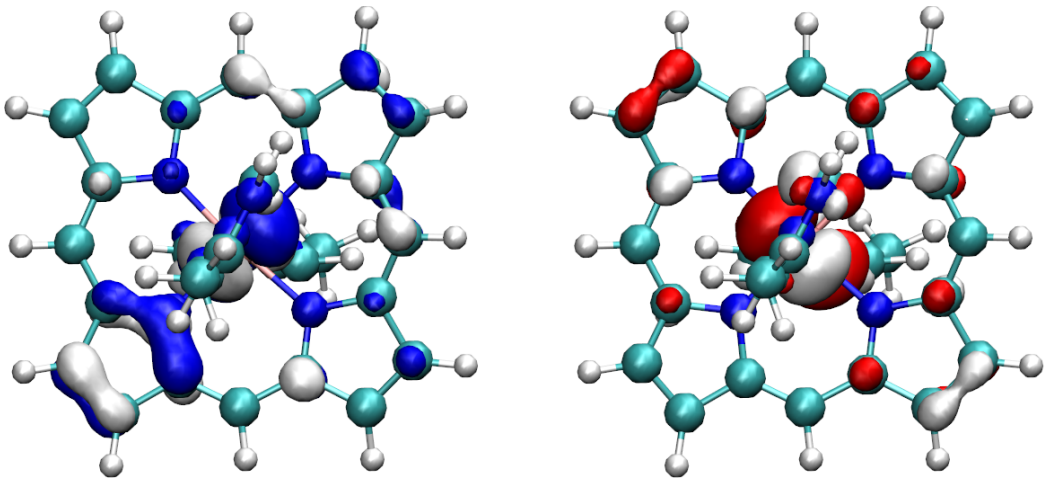

Figure 5.12: The SOMO and SOMO-1 orbitals of a heme taken from an MD snapshot. Just like in the perfect heme case the orbitals were identified by the orientation of the d orbital: the SOMO and the SOMO-1 always contain d_{xz} and d_{yz} where the direction z is always along the axis formed by the histidine molecules. However, it is worth noting that the nodal structure on the porhyrin ring is quite different from the one presented in Fig. 5.10 which probably has a significant effect on the overlap.

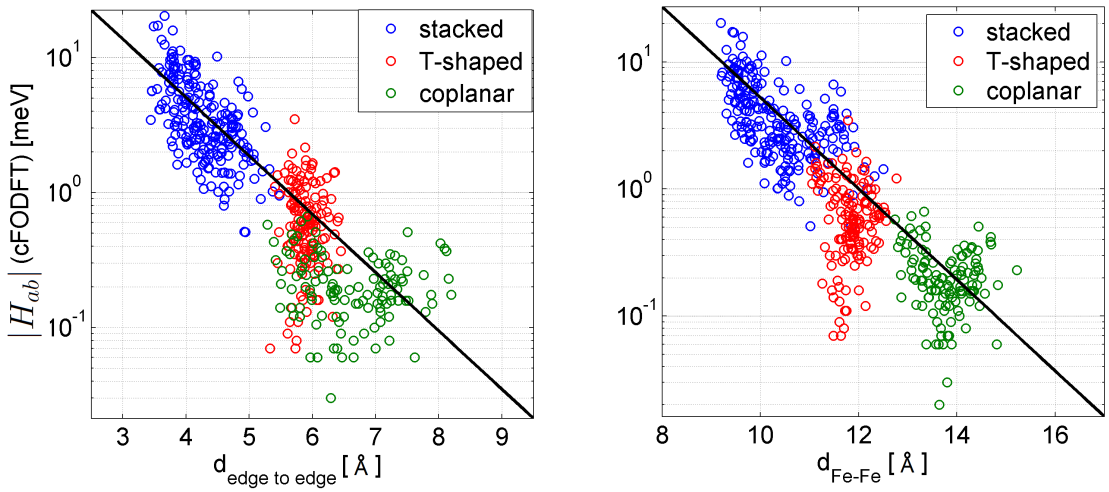

Figure 5.13: On panel A, the correlation between the cFODFT coupling and the edge-to-edge distance can be seen. On panel B, the correlation between cFODFT electronic coupling and the iron to iron distance can be seen for the three different stacking types.

Chapter 4. The β parameter was derived by fitting the following expression to the edge-to-edge and coupling values,

$$H_{ab}(d_{\text{edge}-\text{edge}}) = A \cdot \exp\left(-\frac{\beta}{2} \cdot (d_{\text{edge}-\text{edge}} - d_0)\right) \tag{5.20}$$

Table 5.14: Exponential decay as a function of edge-to-edge distance for cFODFT coupling values. To reduce errors the coupling values were binned together. The bins were 0.5 Å wide. The fit was made to different selections: stacked stands for stacked only, stacked+T is fitted to the joint group of stacked+T-shaped; and all includes every stack type, stacked, T-shaped, and coplanar.

	MtrF		MtrC		STC		Total	
	β [Å^{-1}]	R^2	β [Å^{-1}]	R^2	β [Å^{-1}]	R^2	β [Å^{-1}]	R^2
stacked	1.62	0.971	2.04	0.997	3.24	0.995	2.22	0.985
stacked+T	1.66	0.975	1.82	0.992	2.24	0.988	1.80	0.989
all	1.66	0.975	1.86	0.992	2.24	0.988	1.82	0.991

where d_0 is the van der Waals distance 3.6 Å. Such an expression expects that the overlap between the two SOMOs dominate the coupling values and as a consequence it shows an exponential decay. This value is of course modulated by the nodal structure of the heme SOMOs. The coupling values were binned together for every 0.5 meV interval and the coupling values were averaged. Since the small coupling values were neglected, the β parameters are different for the MtrF from those reported in Ref. [79] for the stacked only fit the results were 1.62 Å^{-1} whereas the reported value was 2.25 Å^{-1}. The decrease in the β parameter is clearly due to the exclusion of small stacked values. Despite the fact that the coplanar values had to be eliminated and the bin size was slightly different, the overall fit was quite similar to the the one reported in Ref. [79]: β=1.66 Å^{-1} as opposed to β=1.65 Å^{-1}.

The difference between the β values for the three systems is very prominent when only stacked pairs are included but less so when T-shaped couplings are included in the fit. For MtrC, the fit to all values resulted in a β value of 1.86 Å^{-1}, which is larger than the same fit for MtrF (1.66 Å^{-1}) but lower than the STC value (2.24 Å^{-1}). It seems that the fit becomes steeper for higher coupling values as MtrF had the lowest stacked values while STC had the highest ones. This is also true for MtrC and STC for different coupling types: stacked only fits are the steepest and stacked + T-shaped fits are less steep, except for MtrF where the difference is very small. Since very few coplanar values were above 0.5 meV they had a very small effect on

Table 5.15: Exponential decay as a function of Fe-Fe distance for cFODFT couplings. To reduce errors the coupling values were binned together. The bins were 0.5 Å wide. The fit was done including all stacking types for all three proteins.

	MtrF		MtrC		STC		Total	
	β [Å^{-1}]	R^2	β [Å^{-1}]	R^2	β [Å^{-1}]	R^2	β [Å^{-1}]	R^2
$\text{FODFT}_{\text{all}}$	1.55	0.89	1.41	0.95	1.77	0.97	1.48	0.97

the couplings. Of all the systems, MtrF showed the most consistent β parameter for both stacked and stacked+T-shaped pairs.

The exponential decay for the cFODFT was also evaluated for the Fe-Fe distance. Similarly to the edge-to-edge distance case, the values were binned together for every 0.5 Å. In this case, only the entire set was considered, the results are shown in Table 5.15. Omitting the low couplings resulted in slightly higher β values for MtrF than reported in Ref. [79], 1.55 Å^{-1} instead of 1.3 Å^{-1}. MtrC had a slightly lower β parameter than MtrF and just like in the edge-to-edge case STC showed the highest β value. The R^2 values were slightly lower than in the edge-to-edge case for all proteins, but that is expected as the edge-to-edge distance has a more significant effect on the coupling values.

5.5.4 Conclusions on the applicability of the analytic overlap method on multi-heme systems

The analytic overlap method offers a fast tool to evaluate the coupling values for heme systems which can be used to determine the charge mobility in such systems either by using Marcus theory or non-adiabatic molecular dynamics calculations. The speed-up for heme systems is even more significant than for the previously discussed organic systems, as the transition metals often slow down the wavefunction convergence. Furthermore, the analytic overlap can be calculated at no additional overhead from the d orbitals which may be omitted from the calculations. However, the results have a few caveats. There were many coupling values which were be-

low the precision of cFODFT which makes their estimation difficult. Also while the ERMSLEs of the heme systems were almost comparable to those reported in Section 5.1 the spread of the RMS(H_{ab}) vs. RMS($\bar{S}_{ab}$) was much wider. In general, the errors were larger when smaller couplings were also included. In dense systems, such as organic semiconductors, where the mobility is dominated by the largest coupling values the inaccuracy in calculating small couplings is not a serious issue, but it can be a significant problem in proteins where the smallest coupling values can act as bottleneck.

Most of this inaccuracy comes from the fact that the idealised heme structures are used for the overlap calculation which does not necessarily describe well the MD snapshots where the large fluctuations of the heme structure alters the SOMO and SOMO-1 pairs. If the method is to be used to calculate coupling values the results can be improved if instead of one set of STO expansion coefficients a handful of them are used which were obtained for a set of sample structures. Then, a random MD snapshot can be fitted to the most appropriate element of the sample using a more tailored coefficient set instead of one-set-fits-all. It would also be interesting to see how FODFT and FODFTB values compare in this case however it maybe difficult to converge the same orbital with FODFTB [124].

5.6 Non-adiabatic coupling vector element calculations with the fast overlap code

The overlap method can be applied to address another element in the non-adiabatic transport model. As was shown in Chapter 3 in Eq. (3.23), in order to propagate the excess electron in the system, the Hamiltonian matrix elements H_{kj} and the non-adiabatic coupling elements $\langle\phi_k|\frac{\mathrm{d}\phi_j}{\mathrm{d}t}\rangle$ have to be calculated. While the former has been addressed extensively in this chapter, the latter is more difficult to calculate. In this section, a possible approximation of the non-adiabatic coupling is presented

using the analytic overlap method.

Applying the chain rule, the non-adiabatic coupling can be expressed as a dot product of the nuclear velocity vector $\dot{\mathbf{R}}$ and the non-adiabatic coupling vector $\langle\phi_k|\nabla_{\mathbf{R}}\phi_j\rangle$,

$$\langle\phi_k|\frac{\mathrm{d}\phi_j}{\mathrm{d}t}\rangle = \dot{\mathbf{R}}\cdot\langle\phi_k|\nabla_{\mathbf{R}}\phi_j\rangle. \tag{5.21}$$

In order to calculate the non-adiabatic coupling elements, the nuclear velocity can be obtained from the molecular dynamics while the non-adiabatic coupling vector (NACV) can be expressed using a finite difference method:

$$\langle\phi_k|\nabla_{\mathbf{R}}\phi_j\rangle \approx \langle\phi_k(\mathbf{R})|\frac{\phi_j(\mathbf{R}+\delta\mathbf{R})-\phi_j(\mathbf{R})}{\delta\mathbf{R}}\rangle \tag{5.22a}$$

$$\langle\phi_k|\nabla_{\mathbf{R}}\phi_j\rangle \approx \frac{\langle\phi_k(\mathbf{R})|\phi_j(\mathbf{R}+\delta\mathbf{R})\rangle}{\delta\mathbf{R}} - \frac{\langle\phi_k(\mathbf{R})|\phi_j(\mathbf{R})\rangle}{\delta\mathbf{R}} \tag{5.22b}$$

$$\langle\phi_k|\nabla_{\mathbf{R}}\phi_j\rangle \approx \frac{S_{\mathbf{R},\mathbf{R}+\delta\mathbf{R}} - S_{\mathbf{R},\mathbf{R}}}{\delta\mathbf{R}} \tag{5.22c}$$

where $\phi_j(\mathbf{R}+\delta\mathbf{R})$ is the wavefunction where the excess electron is localised on site j and the nuclear structure is distorted by $\delta\mathbf{R}$. This 2-point scheme approximates the non-adiabatic coupling vector to be proportionate to the difference between the overlap of one distorted and one undistorted molecule and two undistorted molecules.

5.6.1 Assumptions of the NACV calculation with AOM

As the finite difference model yielded a solution that is a linear combination of overlaps, the fast overlap method can provide a framework to calculate the NACVs. However, considering the computational challenges of the NACV calculation and the limitation of the fast overlap method, it is crucial to understand the approximations made here.

In a donor-acceptor system where the donor has N atoms and the acceptor has M atoms the NACVs $\langle\phi_k|\nabla_{\mathbf{R}}\phi_j\rangle$ and $\langle\phi_j|\nabla_{\mathbf{R}}\phi_k\rangle$ have a total number of $3M+3N$

components, including all atoms of the acceptor and the donor in all three possible directions. Using Eq. (5.22c), this means that $3 \times (N + M) + 1$ overlap calculations are performed including $S_{\mathbf{R},\mathbf{R}}$.

Like in the preceding chapters, non-orthogonal localised states give an intuitive framework to understand the components of the expression but the reference wavefunction has to be derived from an SCF calculation. Using fragment orbital based methods to obtain the coefficients avoids polarisation effects and reduces the number of wavefunctions to be calculated. For example, the wavefunction in state k (approximated as SOMO of the donor) is unchanged when the distortion $\delta\mathbf{R}$ only happens to the nuclear structure of the acceptor molecule and vice versa. This means that the undistorted wavefunctions on the acceptor and the donor, denoted as $\phi_A(\mathbf{R})$ and $\phi_D(\mathbf{R})$ respectively, are the same in each calculation. As a consequence, the number of localised wavefunctions which have to be calculated is $3 \times (N + M) + 2$. In the AOM case, the SOMO is projected onto the STO basis set. Following the steps of the S_{ab} calculation in Section 5.1, the $\phi_j(\mathbf{R} + \delta\mathbf{R})$ can be obtained by performing an SCF calculation followed by a Kohn–Sham diagonalisation for every $3 \times (N + M) + 2$ structure. However, this would create a serious overhead which would reduce the advantage gained from replacing FODFT with AOM and would make it impossible to be used in non-adiabatic molecular dynamics simulations.

To avoid the orbital calculation overhead, the following assumptions were applied: since $\delta\mathbf{R}$ is small so is the change in the orbital coefficients and the main difference comes from the fact that the centre of the orbital is displaced. Hence, the same coefficients are used which were derived from the undistorted structure. These coefficients are normalised for the distorted structure and the overlap between the distorted and undistorted molecule is calculated for each component of the NACV. The algorithm performs the following steps:

- Calculate the overlap between the undistorted structures of the donor and acceptor molecules $S_{DA} \equiv S_{\mathbf{R},\mathbf{R}}$

- Define $\delta\mathbf{R}_{i,r}$ where $i = 1 \ldots N + M$ and $r = x, y, z$
- Distort atom i of the molecule in direction r structure $(\mathbf{R} + \delta\mathbf{R}_{i,r})$.
- Reconstruct orbital on distorted molecule using the coefficients of the undistorted molecule c.
- Renormalise coefficients on distorted molecule $c \longrightarrow c'_{i,r}$.
- Calculate overlap between distorted donor molecule and undistorted acceptor molecule $(S_{\mathbf{R},\mathbf{R}+\delta\mathbf{R}_{i,r}})$.
- Calculate relevant NACV elements according to Eq. (5.22c).
- Loop over all atoms of the dimer in all directions (every possible value of i and r).

This way the $3\times(N+M)$ NACV components can be calculated without obtaining the orbital for each distorted structure, as long as the approximations hold.

5.6.2 Validation

Clearly, the overlap method for NACV calculation is only useful if the assumptions with respect to the wavefunctions provide a good approximation to higher level solutions. An SCF comparison can be used to assess the effects of the orbital relaxation. Polarisation between the monomers was omitted here as well and, to be consistent with the previous sections, FODFT benchmarking was chosen with simulation details identical to those in Section 4.3.

For testing purposes parallelly stacked ethylenes were used at 3.5 Å, 4.5 Å, and 5.0 Å stacking distance. Since $2 \times 3 \times N$ calculations have to be performed a smaller system is a better choice, as the computational requirements are lower. The symmetric configuration also allowed us to check whether the program reproduces the symmetry of the system. Furthermore, since the errors of the AOM have been tested

against FODFT ($\bar{S}_{ab} > 10^{-4}$ for compounds containing second row atoms only) and the accuracy of FODFT was also tested I had to choose a system which has large NACV elements. It is expected that in large π-conjugated molecules the NACV elements are smaller than in smaller molecules as the effects of the distortions are evened out by the large conjugation length. For example, if the NACVs are calculated for a C_{60} dimer using AOM it is easy to see that the results fulfill the qualitative expectations: the closer the atoms are to the interface of the two buckyballs the larger the NACV elements are. On the other hand, for such a large molecule even the largest NACV component ($\sim 10^{-3}\text{Å}^{-1}$) is smaller than the accuracy of this approximation ($\sim 10^{-2}\text{Å}^{-1} \approx 10^{-4}/0.01[\text{Å}]$). As an ethylene molecule is much smaller than a C_{60}, the distortion of a single ionic position causes more significant changes in the overlap. Hence, the NACV components of an ethylene dimer are large enough to compare the FODFT and AOM results.

First of all, a robustness test for both methods was performed with respect to $\delta\mathbf{R}$. The FODFT NACV values are independent of the magnitude of $\delta\mathbf{R}$ in a broad range. Reference calculations were performed on the largest coupling value. To this end, a series of different δR values were applied ranging from 10^{-2} to 10^{-4} Å beyond which the accuracy of the overlap values would have meant loss of digits in the NACV values. The data is consistent in the range observed with both FODFT and the AOM and the results can be seen in Table 5.16.

Table 5.16: NACV component calculation robustness with FODFT and analytic overlap method as a function of different δR values for the finite difference method as in Eq. (5.22).

δR [Å]	10^{-2}	10^{-3}	10^{-4}
FODFT NACV (C_x) [Å^{-1}]	0.0601	0.0606	0.0605
AOM NACV (C_x) [Å^{-1}]	0.0390	0.0396	0.0397

For testing purposes, a $\delta R = 10^{-2}$ Å was chosen with both methods. All possible NACV elements were calculated and compared at three different dimer separations,

3.5, 4.5, and 5.0 Å taking into account the symmetry of the system. The arrangement of the molecules is depicted in Fig. 5.14. Three different methods were used to

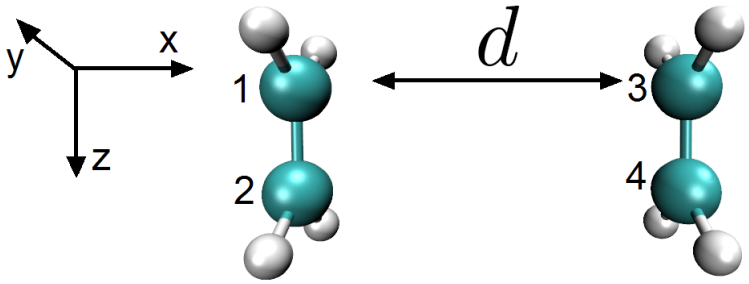

Figure 5.14: The parallelly stacked symmetric ethylene dimer system used as a test system for NACV calculation. The intermolecular distance d was set to 3.5 Å, 4.5 Å and 5.0 Å. The symmetry of the dimer system was reflected in the NACV components

calculate the non-adiabatic coupling vector elements. In the reference method, every step was done using FODFT: the wavefunctions were relaxed on the distorted structure and the overlap was calculated using the SCF plane wave wavefunction without projecting it onto the STO basis set. In the hybrid method, the orbitals were relaxed on the distorted structure with FODFT and then projected onto the p_π orbitals; the overlap was calculated with the analytic overlap method. This method included the relaxation on the distorted structure but the overlap was calculated with the reduced basis set. In the AOM case, the orbital is not relaxed: the molecule is distorted and the orbital is normalised on the distorted structure; the NACV is calculated according to the algorithm in Subsection 5.6.1.

Table 5.17 contains the results for ethylene NACV at different distances. In this configuration, everything is aligned; the most prominent effect on the coupling is coming from the modified centre-to-centre distance between the atoms. Therefore, the largest components of the NACVs are expected to be the C_x values. This proved to be true with all three methods. Although the hybrid method is expected to be more accurate than the purely AOM results, the AOM gives slightly better results for larger distances, while the hybrid method gives better results at the van der Waals

distance (3.5 Å). Of course this does not mean that AOM is a better approach; this effect is more likely due to error cancellation. The x components had a MRUE of 26% and MAXERR of 0.02 Å^{-1} with the hybrid method, and 19% MRUE and 0.03Å^{-1} MAXERR with AOM. The AOM error was strongly distance dependent and gave the best approximation at 4.5 Å with less than 3% error. Basically, the results are very good with both methods. The effects of the orbital relaxation is negligible. C_y values are not indicated in any of the cases as they are well below the accuracy of the method (0.01 Å^{-1}) even at 3.5 Å distance.

The C_z components showed a much larger deviation from the FODFT results with relative errors of 82% for the hybrid method and 92% for the AOM. The results are an order of magnitude off from the FODFT method with both approximate methods. In the z direction, the hybrid method gives consistently better results than the AOM at all distances. This means that in this case, the differences partially arise from the relaxation of the orbital on the distorted structure. However, as the hybrid method does not fully account for the change even when s orbitals are included in the overlap, there is another underlying effect. A possible explanation is that since these values are small, this might be the limit of accuracy with which the FODFT results can be reproduced, the effects of the distortion in the z direction cannot be well projected onto the minimum STO basis set.

As expected, the contribution of the H atoms were all below the precision of the presented methods, therefore they are not discussed. It is worth noting however, that in the FODFT approximation displacing the H atoms slightly alters the shape of the SOMO causing the NACV components to be non-zero. In the AOM algorithm, the orbital is not SCF optimised and since only the p_π orbitals are taken into account the H atoms do not contribute explicitly to the overlap (not even when s orbitals are taken into account). On the other hand, the positions of the H atoms have an implicit effect on the orbital shape as their displacement can alter the p_π directions on the C

Table 5.17: NACV calculations with three different methods at different dimer separations on a perfectly stacked ethylene dimer. In the case of the reference FODFT method, the wavefunction is relaxed on the distorted structure and the overlap is calculated between the full orbitals. The hybrid method relaxes wavefunctions which are projected onto the minimum STO basis set and calculates the overlap analytically. The AOM uses the undistorted STO coefficients and calculates the overlap analytically. The results are calculated at different distances. The letters refer to the type of atom and the direction of the NACV element.

separation	method	$C_{x,1} = C_{x,2}$	$C_{z,1} \approx -C_{z,2}$
3.5 Å	Ref. (FODFT)[Å^{-1}]	6.01×10^{-2}	3.95×10^{-2}
	Hybrid[Å^{-1}]	4.14×10^{-2}	5.77×10^{-3}
	AOM [Å^{-1}]	3.43×10^{-2}	3.14×10^{-3}
4.5 Å	Ref. (FODFT)[Å^{-1}]	2.18×10^{-2}	2.00×10^{-2}
	Hybrid[Å^{-1}]	1.69×10^{-2}	3.80×10^{-3}
	AOM [Å^{-1}]	2.13×10^{-2}	1.19×10^{-3}
5.0 Å	Ref. (FODFT)[Å^{-1}]	1.30×10^{-2}	1.36×10^{-2}
	Hybrid[Å^{-1}]	9.80×10^{-3}	2.65×10^{-3}
	AOM [Å^{-1}]	1.45×10^{-2}	1.42×10^{-3}

atoms. Consequently, by moving the H atoms in the plane of the conjugation (y and z directions in this configuration), the p_π directions on the C atoms are unchanged and therefore the overlap as well, resulting in 0.00 H_y and H_z components. This is true for all NACV elements when the AOM code is used on a compound which have atoms which do not participate in the π-conjugation.

5.6.3 Conclusion of NACV calculation with the AOM

It was shown how the analytic overlap method can be used to approximate the non-adiabatic coupling vector elements for π-conjugated systems using the example of the ethylene dimer for which the NACV values were fairly accurate. Since all other conjugate systems are larger the absolute error in NACV calculations is expected to decrease. It was also demonstrated that the results are more accurate in the stacking direction but are consistently underestimated along the bond direction by an order of magnitude which is expected to be due to the limited STO basis set.

This, however, might not be such a significant issue as the accuracy of the derived NACV elements can be measured best by analysing their effect on the non-adiabatic molecular dynamics simulations. Most of the times, the effect of NACV is negligible but they gain importance at the crossing of the diabatic surface. Off-diagonal forces can also be derived from the NACVs as

$$\nabla H_{kj} \approx \bar{C} \cdot \nabla \bar{S}_{kj} = \bar{C} \cdot (\langle \phi_j | \nabla_{\mathbf{R}} \phi_k \rangle^* + \langle \phi_k | \nabla_{\mathbf{R}} \phi_j \rangle) \tag{5.23}$$

In this case, the two directions are not equal. In the x direction both components are pointing in the direction of the other monomer pushing them together, while in the z direction the off-diagonal forces point towards one another along the bond. These derived off-diagonal forces are around 1.3×10^{-3} a.u. along the bond which is two orders of magnitude smaller than the C=C spring constant, therefore the effects are negligible. The NACV component along the covalent bond is expected to be even smaller for molecules larger than ethylene. Therefore, it is expected that the error made for this component will not have a significant effect in non-adiabatic molecular dynamics runs.

5.7 Further speed-up

The fast analytic overlap method also introduces another opportunity to make the scheme linearly scaling with molecule size through the introduction of a cut-off for the calculation of atomic orbital pair overlaps. This can improve the speed-up for larger molecules. There are two options: the cut-off can be distance dependent; in this case the overlap is calculated only between atoms of the acceptor an the donor which are not further than a certain $r^{\max}$ distance. Another way is to calculate the overlap between those atoms for which the atomic overlap is expected to be larger than the threshold $s_{ab}^{\min}$ and all other components of the atomic overlap matrix is set

to 0. The benefits of the first method is rather trivial. The second method, termed here as minimum atomic overlap method, becomes very useful if AOM is used within NAMD simulations. During dynamics, the overlap and NACV values are changing slowly compared to the time resolution. For the minimum atomic overlap method an atomic neighbour list can be created for each molecular dimer which tells which atom pairs fulfill the criterion $s_{ab} > s_{ab}^{\min}$. This list can be updated once the nuclear motion is significant enough to make changes to the overlap. The two methods are expected to be in general rather similar as the atomic overlap is strongly dependent on the interatomic distance. The minimum interatomic overlap method becomes useful when the molecules have a complex nodal structure. In this case, it could be that although two atoms are close to one another but the overlap is negligible because the orbitals of those atoms hardly contribute to the SOMO. In this case, while the overlap is still calculated in the minimum interatomic distance method in the minimum atomic overlap method these calculations are set to 0.

In terms of computational time, the cut-off makes no difference for small systems but larger molecules such as C_{60} benefit from it significantly. This implementation uses the minimal inter-atomic overlap criterion method. The effects of a reduced atomic overlap calculation can be seen in Table 5.18.

For atomic overlap cut-offs greater than 10^{-6} increasing amount of NACV elements became exactly zero. Despite this, there is no significant change in the value of the largest component which is dominated by the larger atomic overlap values. The cut-off can be applied generously for C_{60}, as expected the coupling values are affected mostly by the atomic overlaps of a few atoms closest to the interface of the monomers. The accuracy of the smaller coupling value was preserved better than the larger one. When the atomic overlap cut-off is set to 10^{-2} the overlap and all NACV components become 0.

Table 5.18: Different atomic overlap cut-offs, and their effect on the overlap calculation accuracy and computational time demonstrated on two C_{60} dimers one with a large overlap value, and another one with a small one.

$s_{ab}^{\min}$	$\bar{S}_{ab}$	CPU time [s]	NACV [$\mathring{A}^{-1}$]	CPU time [s]
		high coupling C_{60}		
none	7.029×10^{-3}	0.00257	1.91×10^{-3}	0.1645
10^{-8}	7.029×10^{-3}	0.00161	1.92×10^{-3}	0.1398
10^{-6}	7.051×10^{-3}	0.00077	1.92×10^{-3}	0.1066
10^{-5}	6.859×10^{-3}	0.00040	1.92×10^{-3}	0.0776
10^{-4}	7.642×10^{-3}	0.00018	1.92×10^{-3}	0.0478
10^{-3}	2.661×10^{-3}	0.00010	2.92×10^{-3}	0.0375
		low coupling C_{60}		
none	1.930×10^{-5}	0.00270	1.83×10^{-3}	0.1579
10^{-8}	1.931×10^{-5}	0.00149	1.83×10^{-3}	0.1258
10^{-6}	1.940×10^{-5}	0.00074	1.83×10^{-3}	0.1045
10^{-5}	9.741×10^{-6}	0.00040	1.82×10^{-3}	0.0771
10^{-4}	1.576×10^{-5}	0.00017	1.67×10^{-3}	0.0458
10^{-3}	1.727×10^{-5}	0.00011	1.58×10^{-3}	0.0413

5.8 Conclusion

It was demonstrated in this chapter that the electronic coupling matrix elements between π-conjugated organic molecules scale approximately linearly with the overlap between the singly occupied molecular orbitals in the range relevant to electron transport in the condensed phase (5 to 500 meV). It was also shown that a single proportionality constant can describe a broad set of molecules, and the accuracy is retained when the basis set is replaced with the minimum STO basis set with optimised Slater decay coefficients.

This also provides a tool to estimate electronic couplings analytically, leading to speed-ups of approximately six orders of magnitude compared to standard DFT calculations for molecules typically used in molecular OSCs. The analytic overlap

method can also be used to estimate off-diagonal elements of the Hamiltonian in NAMD simulations of charge transport where further speed-up is possible when atomic overlap cut-off is used.

The analytic overlap method offers a fast option for evaluating the coupling values which can be used to determine the charge transport using Marcus theory as well. This was demonstrated on a set of heme systems where the effect of molecular dynamics was also taken into account. The convenience of omitting the d orbitals and using the optimised coefficients offers a reasonable approximation for the coupling values and saves computational time. Here, the main issue is the magnitude of the H_{ab} values. Heme systems often have coupling values less than 1 meV which makes them prone to error with the AOM. Furthermore, hemes are non-rigid molecules. In particular, the rotation of the histidine molecules has a very low energy barrier. This causes large fluctuations in the orbitals which make the overlap deviate significantly from the values calculated with the idealised orbital coefficients. These two effects can lead to large errors in charge transport modelling as in proteins electron transfer is often dominated by the smallest coupling, which acts as a bottleneck for the process. Although in its current form the model may not be ideal for calculating rates in non-adiabatic molecular dynamics, it is possible to adapt the model to tackle the issue by defining multiple coefficient sets based on a set of reference molecular conformations of hemes. Molecular dynamics snapshots of heme molecules can be fitted to these reference sets by minimising the root-mean-square distance between the molecules and finding the best fit. The orbital coefficients of the best fitting reference molecules can be used on the MD snapshot hemes.

The analytic overlap method can also be used to approximate the non-adiabatic coupling vector elements for π-conjugated systems. This was demonstrated on the ethylene dimer. The NACV component pointing from one molecule to the other could be reproduced well compared to FODFT reference calculations. Although the results were not so good along the bonds, this is not an issue as the nuclear forces

arising from the off-diagonals of the Hamiltonian are two orders of magnitude smaller than the nuclear forces in the same direction. Since all other conjugated systems are larger than an ethylene molecule the absolute value of the NACV components are smaller. Therefore, the absolute error in the off-diagonal forces is expected to be even smaller for OSC molecules.

6 Kinetic Monte Carlo simulations for charge carrier hopping

In Chapter 3, the various parameters required to simulate charge transport in organic systems were discussed and Chapters 4 and 5 were focusing on the calculation of the electronic coupling matrix elements and the non-adiabatic coupling vector elements in different systems with various methods.

As mentioned in Chapter 2, the role of dynamic disorder in organic semiconductors can be very significant. This is especially true for fullerene crystals as discussed in Refs. [45, 49]. Chapter 5 discussed the applicability of the analytic overlap method in heme systems which were extracted from molecular dynamics trajectories. For these systems a few issues arose from the small coupling values and the orbital fluctuations due to intramolecular deformations. However, the relatively limited movements of the heme systems did not cause a significant change in the individual couplings over time, and the magnitude of the coupling fluctuations remained small throughout the trajectory [79].

As discussed previously, localised transport is not applicable in many organic systems. In some cases, this is due to the fact that the energy barrier between the two states disappears and the charge carrier no longer forms localised polarons. In other cases, the partial delocalisation is due to dynamic effects, as the molecular motion affects the couplings and can create clusters of delocalised states.

Non-adiabatic molecular dynamics provides a tool which allows charge transport simulation in those systems which are partially delocalised. However, in those systems where localised transport is applicable, rate equation-based charge transport

models provide a faster solution. To this end, understanding the timescales of different parameters which contribute to the transport is crucial for developing better models. This chapter presents the application of the analytic overlap method in a localised transport model where a rate equation is used to determine the charge transport (the basic theoretical underpinnings of which were discussed in Chapter 3). It goes on to present a practical implementation to obtain mobility values by using the rate equation in combination with a kinetic Monte Carlo program. The first half of the chapter presents the details of the implementation in particular, the calculation of various components of the rate equation such as the electronic coupling matrix element, the reorganisation energy, and the nuclear tunneling frequency. The second half of this chapter discusses the dynamic effects in organic systems and the separation of time scales of different parameters relevant to localised transport.

6.1 Implementation

As mentioned in Chapter 3, rate equation based transport can be described as Markovian process. This means that between each hop the electron thermalises and the system has no memory. Therefore the hop from state (site) i to state (site) $i+1$ only depends on state (site) i and has no memory of state (site) $i-1$. Electron hopping from site to site is a discrete Markovian process as the possible states are countable. The time evolution of such systems can be described with the master equation

$$\frac{d\mathbf{P}}{dt} = A(t)\mathbf{P}(t) \tag{6.1}$$

where $\mathbf{P}$ is the time dependent probability vector of the electron being in a given state and A is the connection matrix depending on time depndent rate constants. Monte Carlo models also offer a solution. The kinetic Monte Carlo code presented here uses the generalised rate expression, Eq (3.16) from Ref [45], which interpo-

lates between non-adiabatic and adiabatic charge transfer expressions. This rate expression requires the electronic coupling matrix element between the molecules of interest, the reorganisation energy, the free energy difference between the hopping sites, and the effective nuclear frequency along the reaction coordinate. The electronic coupling matrix elements are calculated using the analytic overlap method code described in Chapter 5 which is called by the kinetic Monte Carlo code I have written.

The electron is propagated using the Borz–Kalos–Leibowitz algorithm which is a no-rejection Monte Carlo algorithm. This algorithm requires two random numbers per hop [125, 126]. The first random number drawn, $r_1 \in (0, 1]$, determines the residence time at the current site i before it hops to the an adjacent site with the equation

$$t_{\text{stay}} = -\frac{1}{k_i} \ln(r_1). \tag{6.2}$$

where $k_i = \sum_j k_{ij}$ is the sum of the hopping rates between site i and its nearest neighbours. A second random number $r_2 \in (0, 1]$ is generated to determine the hopping direction. The interval $(0, 1]$ is divided into n intervals, where n is the number of neighbours for given site, and the size of these intervals is proportional to the magnitude of the hopping rates to each neighbouring site. The region which contains r_2 indicates the hopping direction. After each hopping step the system time is updated by t_{stay} and the displacement of the electron is updated by the displacement vector between the new site and the previous site. Periodic boundary conditions are applied to avoid finite size effects. Each KMC trajectory is terminated when the system time reaches a given maximum simulation time which is specified in the input file. The final displacement compared to the initial site and the system time are dumped into separate output files. To ensure ergodicity, the initial site for each trajectory is randomly chosen according to uniform distribution, assuming that the injected electron has a much higher energy than any of the sites. Although

the code itself does not perform molecular dynamics it can be used to study the dynamics in the system by loading trajectories obtained from molecular dynamics done with other packages such as AMBER or NAMD.

6.1.1 Rate calculation

To support this model, a suitable rate expression had to be used. For the rate calculation, the generalised rate expression Eq. (3.16) is used, of which the non-adiabatic (3.12) and the adiabatic (3.13) rate are limits in special cases

$$k = \kappa_{\mathrm{el}} \nu_n \Gamma \exp(-(\Delta A^{\dagger}/k_{\mathrm{B}}T))) \tag{6.3}$$

In order to calculate the rates, the activation free energy, the electronic coupling elements, the reorganisation energy, and the effective nuclear frequency have to be obtained for this model system.

Reorganisation energy

The reorganisation energy was calculated according to Marcus and consists of an inner-sphere contribution λ_{i} and an outer-sphere contribution λ_{o} [42],

$$\lambda = \lambda_{\mathrm{i}} + \lambda_{\mathrm{o}} \tag{6.4}$$

The inner sphere contribution is calculated using the four-point scheme

$$\lambda_i = (E_{\mathrm{C}}(\mathbf{R}_{\mathrm{N}}) + E_{\mathrm{N}}(\mathbf{R}_{\mathrm{C}}) - (E_{\mathrm{C}}(\mathbf{R}_{\mathrm{C}} + E_{\mathrm{N}}(\mathbf{R}_{\mathrm{N}})) \tag{6.5}$$

The terms in the sum come from four single point SCF energy calculations with simulation details analogous to the ones presented for fullerenes in Section 5.3. The optimised charged ($\mathbf{R}_{\mathrm{C}}$) and neutral ($\mathbf{R}_{\mathrm{N}}$) configurations were the same as the ones presented in Table 6.1. E_{C} refers to single point calculation for a charged molecule

and E_{N} refers to a neutral single point calculation. This is only calculated for one pair of SCF minimised molecules, it is expected that the inner sphere contribution does not change substantially throughout the charge transport process at finite temperatures. The outer-sphere contribution was estimated with the Marcus formula taking into account the effect of the polarisability of the surrounding molecules

$$\lambda_{\mathrm{o}} = (\Delta q)^2 \left(\frac{1}{\varepsilon_{\mathrm{op}}} - \frac{1}{\varepsilon_{\mathrm{s}}} \right) \left(\frac{1}{r} - \frac{1}{R} \right), \tag{6.6}$$

where $r = 5.02$ Å is the van der Waals radius of the C_{60} cage. $\varepsilon_{\mathrm{op}}$ and ε_{s} are optical and static experimental dielectric constants [127, 128], R is the intermolecular distance and Δq is the charge difference. The polarisable sphere model works well for the C_{60} molecules but it can introduce errors for elongated molecules such as pentacene. Therefore, the outer-sphere contribution is optional in the code.

Free energy calculation

The free energy values were obtained from molecular dynamics calculation. To be comparable with the DFT results, the molecular dynamics force field parameters were altered to reproduce the charged and neutral bond lengths of C_{60} in Table 6.1 and the λ_i value obtained by DFT according to Eq. (6.5). The MD simulation is done in an NVT ensemble where all molecules are neutral. Then, using this neutral trajectory, the energies are evaluated again by making each molecule charged, simulating that the electron is in a given configuration during the entire trajectory but with an unchanged geometry, and thus obtaining the vertical energy difference between the charged and the neutral state ΔE.

$$\Delta E_i = E_{\mathrm{C},i}(\mathbf{R}_{\mathrm{N}}) - E_{\mathrm{N}}(\mathbf{R}_{\mathrm{N}}) \tag{6.7}$$

where $E_{\mathrm{C},i}$ is the energy value for a given snapshot when the electron is located on site i and $\mathbf{R}_{\mathrm{N}}$ refers to the nuclear coordinates of the entire neutral trajectory.

The free energy calculation can be obtained by using the Landau free energy term [41]. However, since there are no solvents included the expected energy landscape has rather sharp peaks. The free energy is calculated as the thermal average of the obtained vertical energy differences for a given site i.

$$\Delta A_i = -k_{\mathrm{B}}T \log \left(\sum_i \exp \left(\Delta E_i / k_{\mathrm{B}}T \right) \right) \tag{6.8}$$

Since the reorganisation energy values are fairly uniform and small in small molecule organic semiconductors the free energy difference between two sites can be calculated as

$$\Delta A_{ij} = \Delta A_i - \Delta A_j \tag{6.9}$$

Of course, for identical molecular sites within the crystal, $\Delta A_{ij} = 0$. The energy in the condensed phase is expected to be dominated by the intramolecular terms as the polarisation effect of the surroundings is expected to be less significant in organic semiconductors than in solutions [79].

Coupling calculation

Given the number of coupling calculations one has to perform for a molecular dynamics trajectory, the analytic overlap method can be used to approximate the H_{ab} values. As was shown on the example of the heme system, the coupling values obtained with the SCF minimised ionic structure provided a reasonable approximation for coupling values in molecular dynamics trajectories as long as the coupling values are sufficiently large. For C_{60}, the couplings for the nearest neighbours are expected to range between 1 to 100 meV. Furthermore, crystalline C_{60} is a dense system in which the charge transport is dominated by the largest coupling values. Since AOM was tested on the fullerene system and can tackle the large number number of calculations it is going to be used in this model with the linear scaling factor for Eq. (5.1) obtained in Chapter 5 of $C = 1819$ meV.

In order to address orbital degeneracy, the level of degeneracy can be specified in the input file and the overlap values are averaged according to Eq. (5.19) [123].

Effective nuclear frequency

The effective nuclear frequency along the reaction coordinate can also be obtained by analysing the time dependence of the vertical energy gap. This is done by understanding that in the diabatic representation, the charge transition happens when the vertical energy gap vanishes [129]. Using linear response theory, the effective nuclear frequency can be obtained by taking the weighted average of the spectral density function of the vertical energy gap calculated in the classical MD [41],

$$2\pi\nu_n = \frac{\int_0^\infty \omega \frac{J(\omega)}{\omega} \mathrm{d}\omega}{\int_0^\infty \frac{J(\omega)}{\omega} \mathrm{d}\omega} \tag{6.10}$$

where $J(\omega)/\omega$ is the spectral density function calculated as

$$J(\omega) = \frac{\omega}{2k_\mathrm{B}T} \int_0^\infty c(t) \cos(\omega t) \mathrm{d}t \tag{6.11}$$

where $c(t)$ is the time-correlation function of the vertical energy gap difference between two sites ΔE_{ij}

$$c(t) = \langle \Delta E_{ij}(0) \Delta E_{ij}(t) \rangle \tag{6.12}$$

Eq. (6.12) describes time-dependent behaviour of the system on the diabatic potential energy surface and is used here to understand how often the system gets close to the transition point ($\Delta E_{ij} = 0$). In the case of small molecule organic semiconductors, this is expected to be dominated by the intramolecular vibrations which show up as sharp peaks on the energy spectrum and the spectral density function.

As mentioned in Chapter 3, the localised transport model is only applicable if the activation free energy is positive, and therefore there is a finite energy barrier

between the two localised states. To this end, it can be easily seen in Eq. (3.16) that the localised charge transport can only be used if the coupling is smaller than 3/8 of the reorganisation energy. In order to avoid issues arising from negative activation energy, in this implementation $\Delta A^{\dagger}$ is set to zero when it would be otherwise negative.

6.1.2 Calculating the charge carrier mobility

Three methods are presented in this chapter to calculate the charge carrier mobility μ and are compared for the systems to assess the accuracy of the calculations.

Analytical derivation of μ

The first method does not actually rely on Monte Carlo results. The obtained rates are used to approximate the drift velocity as the average of the sum of the rates k_{nm} multiplied by the corresponding translation vector $\mathbf{r}_{nm}$ as in Ref. [45]. In a unit cell consisting of N molecules, this can be averaged for the unique sites

$$\mathbf{v}_{\text{drift}} = \frac{1}{N} \sum_{n=1}^{N} \sum_{m} k_{nm} \mathbf{r}_{nm} \tag{6.13}$$

where m sums over the possible neighbours of site n . In order to obtain the mobility matrix, the derivative of each velocity component of $\mathbf{v}_{\text{drift}}$, $\mathrm{v}_{\text{drift},i}$, $i = x, y, z$ is taken with respect to the electronic field $\mathbf{E}$ in direction j, E_j, $j = x, y, z$ the mobility is then

$$\mu_{ij} = \frac{\partial \mathrm{v}_{\text{drift},i}}{\partial E_j} = \frac{\partial \left(\frac{1}{N} \sum_n \sum_m k_{nm} \mathbf{r}_{nm} \right)_i}{\partial E_j} \qquad i, j = x, y, z \tag{6.14}$$

Here, the external field is assumed to be small enough so it does not have a significant effect on the dynamics. Therefore, $\mathbf{r}_{nm}$ is independent of the external field $\mathbf{E}$. Thus, the drift velocity only depends on the external field as specified in rate equation Eq. (3.16), where the potential energy difference between two sites in the presence

of external field is

$$\Delta A = -q_e \mathbf{E} \cdot \mathbf{r} + \Delta A_s \tag{6.15}$$

where ΔA_s is the static free energy difference between the two sites. Inserting the rate expression Eq. (3.16) into Eq. (6.14) and evaluating the derivative with respect to E_j gives

$$\mu_{ij} = \frac{1}{N} \sum_n \sum_m r_{nm,i} \frac{\partial k_{nm}}{\partial E_j} = \frac{1}{N} \sum_n \sum_m \frac{D_{ijnm} k_{nm}}{k_\mathrm{B} T} \tag{6.16}$$

where k_B is the Boltzmann constant, T is the temperature, and D_{ijnm} is given by

$$D_{ijnm} = \frac{e r_{nm,i} r_{nm,j}}{2} \left[\left(1 + \left(\frac{2H_{nm}}{\lambda - e E_j r_{nm,j}} \right)^2 \right)^{-1/2} - \frac{e E_j r_{nm,j}}{\lambda} \right] \tag{6.17}$$

In order to obtain mobility values according to this approximation, the knowledge of every coupling value, displacement, and site energy value in the system is required. However, as this mobility value does not depend on the kinetic Monte Carlo results, it can be used to assess if the kinetic Monte Carlo results have converged as long as the system size is reasonable.

Mobility values from Einstein relation

One way to calculate the mobility using the kinetic Monte Carlo results is through exploiting the Einstein relation,

$$\mu = \frac{qD}{k_\mathrm{B} T} \tag{6.18}$$

This is valid when the hopping process is well described by a diffusion process, *i.e.* the medium is isotropic for a given direction (in the positive and negative directions) and the hops are stochastic. The KMC results can be used to obtain the diffusion coefficient D. In the three dimensional case, the probability density of the localised charge movement is

$$P(\mathbf{R}, t) = C(\det(\mathbf{D})) \exp(-\frac{\mathbf{R}^T \mathbf{D}^{-1} \mathbf{R}}{4t}). \tag{6.19}$$

where $C(\det(D))$ is a normalisation factor, $\mathbf{R}$ is the displacement vector, t is time and $\mathbf{D}$ is the diffusion tensor. $\mathbf{D}$ can be determined by taking the slope of the mean square displacement of the particle as a function of time t. In the three dimensional case, this is obtained by taking the covariance matrix of the displacement as

$$\langle (R_i - \langle R_i \rangle)(R_j - \langle R_j \rangle) \rangle = \mathrm{cov}(R_{ij}) = 2D_{ij}t, \tag{6.20}$$

where $i, j = x, y, z$. Thus, the mobility tensor can be calculated as

$$\mu_{ij} = \frac{q\mathrm{cov}(R_{ij})}{k_\mathrm{B}T2t}. \tag{6.21}$$

It is worth noting that this approximation can only be used if the R^2 values are sufficiently large when the components of $\mathrm{cov}(R_{ij})$ are plotted as the function of t.

Mobility values from numerical derivative

By definition, the mobility can be obtained as the derivative of the drift velocity with respect to the external field,

$$\mu_{ij} = \frac{\partial \mathbf{v}_\mathrm{drift}}{\partial \mathbf{E}} = \frac{\mathrm{v}^j_\mathrm{drift}(\mathbf{E} + \delta E\mathbf{i}) - \mathrm{v}^j_\mathrm{drift}(\mathbf{E} - \delta E\mathbf{i})}{2\delta E} \qquad i, j = x, y, z \tag{6.22}$$

where $\mathbf{i}$ and $\mathbf{j}$ are unit vectors in the directions x, y, and z.

6.2 Validation

The KMC code was tested with a single perfectly aligned crystalline C_{60} system to assess the convergence criteria. The fcc crystal had a lattice constant of 14.01 Å and each site was equivalent with zero potential energy difference. Every molecule was rotationally equivalent; the co-rotating internal coordinate system of the buckyballs was aligned with the external coordinate system. The maximum hopping distance

and thus the cut-off for the rate calculation was 12 Å which included the nearest neighbours only.

The convergence of the electronic mobilities in the test system was validated with respect to the number of KMC trajectories, temperature, and overlap conversion factor. The electron mobilities were calculated with all three different methods where applicable: Einstein relation for Brownian motion Eq. (6.18), analytical derivative of the drift velocity according to Eq. (6.16), and numerical derivative of the drift velocity with respect to the external field as in Eq. (6.22).

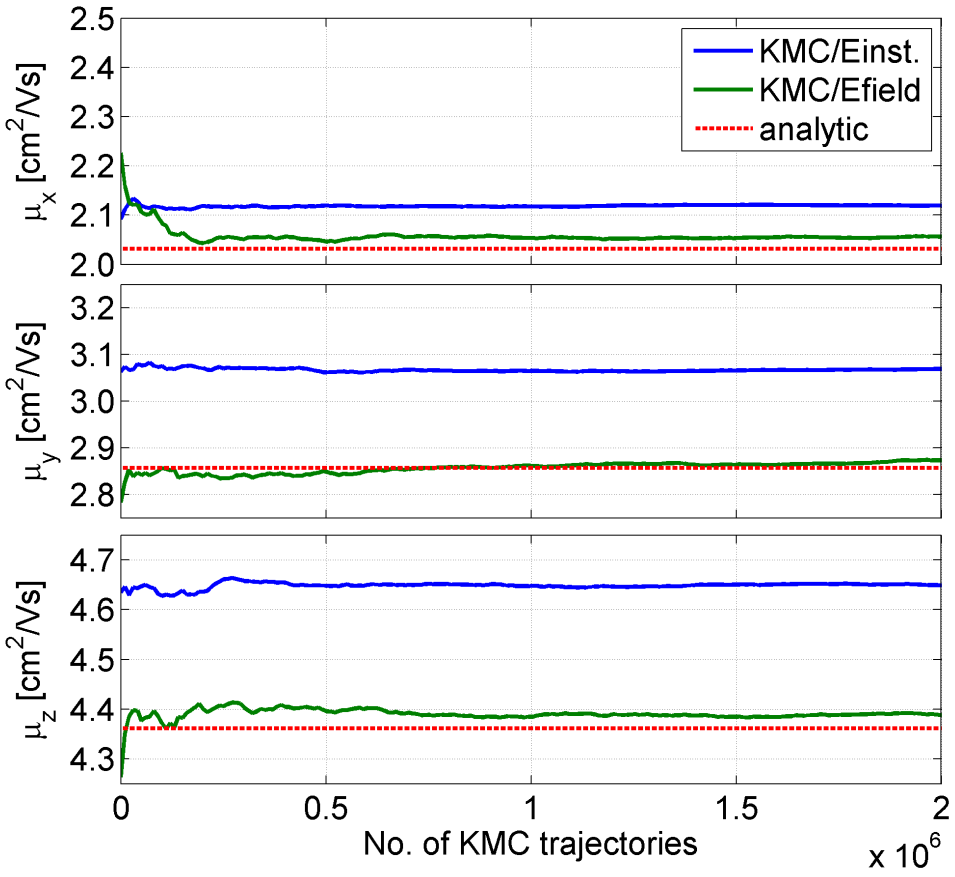

Figure 6.1: Convergence of the mobility values calculated with the finite difference method as in Eq. (6.22) and Eq. (6.18) to the analytically obtained mobility value as a function of the number of Monte Carlo trajectories. The results start to converge at around 5×10^5 trajectories. Using more KMC trajectories changes the mobility values by less than 0.05 cm^2/Vs. It can be seen here that the Einstein mobility values are slightly overestimating the numerical and analytical derivative results and the effect is stronger for larger couplings.

The results of the KMC code were compared to the analytic results obtained from Eq. (6.16). The simulation showed that 5×10^5 individual KMC trajectories for a single snapshot are enough to reach convergence to the accuracy of 0.05 cm^2/Vs both with the finite difference method and the Einstein relation, as can be seen in Fig. 6.1. The code was less sensitive to the simulation time t. Convergence was obtained even when the simulation time was so short that only a few events happened. Furthermore, even at short simulation times of $t = 10^{-12}$ s the $\langle x^2 \rangle$ vs. t plot was a straight line with $R^2 = 0.9997$ which started to deviate from the straight line at shorter simulation times.

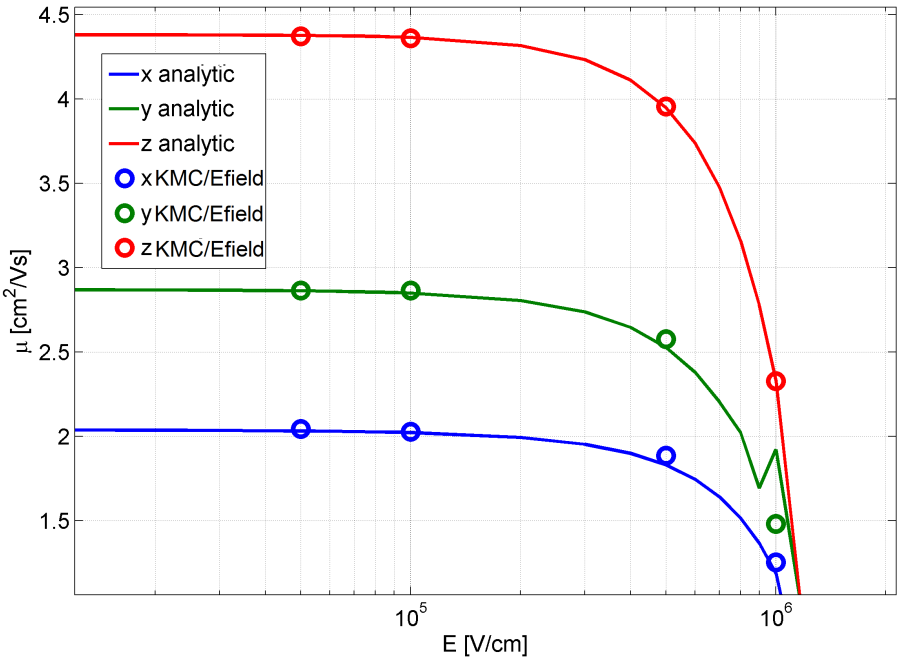

Figure 6.2: External electric field dependency of the electron mobility with different offsets using $\delta E = 10^4$ V/cm. The mobility was evaluated with the analytic derivative method (Eq. (6.16)) and the numerical derivative method as well (Eq. (6.22)). The E-field dependence of the mobilities show constant mobilities at relatively low fields which starts to change around 2×10^5 V/cm. The model breaks down above 10^6 V/cm.

For the numerical derivative formula Eq. (6.22), δE was chosen as 10^4 V/cm. Smaller δE values resulted in more numerical noise in the drift velocity while this

value was well within the linear **E** dependence regime of the mobility. The external field dependence of the mobility was also tested for the test system. It can be seen in Fig. 6.2 that the mobility values were constant with respect to the external field up to 2×10^5 V/cm, whereas, at 10^6 V/cm external field the approximation breaks down.

Although this section does not include dynamics, an approximate temperature dependence was also calculated with the single snapshot. In Fig. 6.3, it can be seen that the three methods give similar results. However, the Einstein method slightly overestimates the values for large couplings, possibly due to the fact at higher mobilities the medium is not satisfying the diffusion criteria mentioned above.

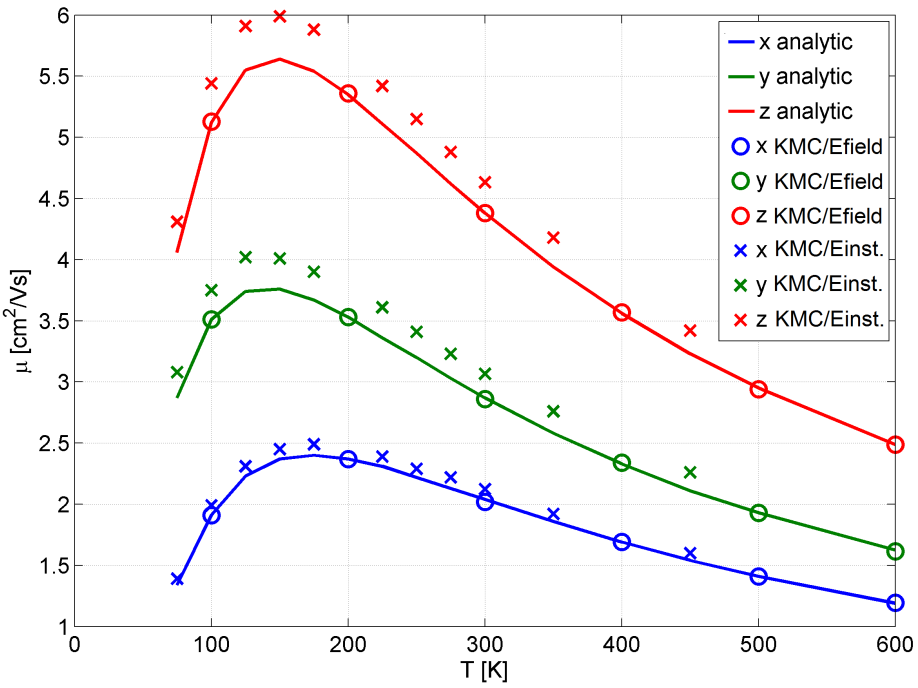

Figure 6.3: Temperature dependence of the charge mobility in a perfectly aligned FCC C_{60} structure. The mobility values are calculated with three different methods of assessing the coupling values: Einstein mobility calculation Eq. (6.18), numerical derivative formula Eq. (6.22), and the analytical mobility Eq. (6.16).

6.3 Simulation details

The system discussed here is the FCC C_{60} which has been studied experimentally [130] and theoretically before [33, 45]. Nelson *et al.* also looked at amorphous phases of C_{60} by simulating physical vapour deposition [30]. As mentioned in the introduction, crystalline C_{60} goes through two phase transitions which affects the mobility. While at room temperature the C_{60} molecules are rotationally independent with a correlation time of 12 ps, at 255 K they lose independent rotation in one direction which makes the structure simple cubic with 4 molecules per unit cell [21]. Below 100 K there is free rotation only in one direction. This phase transition is likely to affect the charge transport: while the mobility is expected to be isotropic at room temperature it is probably anisotropic for lower temperatures.

6.3.1 Molecular dynamics trajectories

Molecular dynamics is used to understand dynamic disorder modulating the coupling values in Eq. (5.1) and to estimate the effective nuclear frequency according to Eq. (6.10). The MD trajectories were obtained with the Amber program package using the forcefield obtained from Ref. [48] in our group. The dynamics were done in an NVT ensemble at 100 K, 300 K, and 500 K with a lattice constant of 14.01 Å. Two trajectories were obtained to analyse the C_{60} system. Firstly, a 1 ns trajectory was obtained with a 1 ps sampling frequency so that there are plenty of rotationally different snapshots. However, the sampling frequency meant that this would not capture the entire energy spectrum as the vertical energy gap changes on the fs time scale. Therefore, another NVT MD trajectory was taken with the same parameters but this was 100 ps in length and 5 fs in resolution. All molecules in the system were neutral throughout the trajectories following a classical path.

6.3.2 Coupling calculation

The electronic coupling calculations were done with the analytic overlap method with the scaling factor of 1819 meV. The reference orbitals were obtained by taking the Kohn–Sham orbitals of a single point DFT calculation using the PBE functional and Goedecker–Teter–Hutter type dispersion corrected atom centred pseudo-potentials to replace the core electrons [131]. The calculations were done with the CPMD code in a plane wave basis set with a basis set cut-off of 90 Ry [105].

It is also an important question how the charge affects the nuclear configuration of the molecule. In the heme case, the ionic structure for the idealised heme molecule was obtained from DFT calculations with the neutral structure (Fe^{2+}) and the dimers were extracted from a MD trajectory where both molecules had 0.5 e charge. As C_{60} molecules are larger and more rigid, it is expected that configurational changes due to the excess charge will be less significant. In the C_{60} case, for the MD calculation the neutral molecules were used and the SCF calculation happened on the SCF optimised charged C_{60}^{-}. The DFT optimisation of the isolated C_{60}^{-} slightly alters the geometry compared to the neutral one. The structural differences were analysed by comparing the two bond types present in C_{60}. Here, they are referred to as $L_{\mathrm{hex-hex}}$ if the bond is between two hexagon rings and $L_{\mathrm{hex-pent}}$ if the bond is between a hexagon ring and a pentagon ring (Fig. 6.4 and Table 6.1). $\mathbf{R}_C$ denotes the geometry optimised with an excess charge and $\mathbf{R}_N$ is the neutral optimised nuclear configuration. The deformation of the bond lengths was small but consistent. The overall effect of the excess charge is a slight stretch of the carbon frame in one direction.

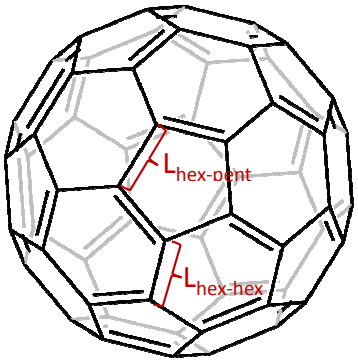

Figure 6.4: The two bond types present in C_{60}. Although both bonds are between sp^2 carbons they differ in length and binding energy.

Table 6.1: Configurational change in the isolated C_{60} due to excess charge expressed in the change of the bond length of the two bond types present in C_{60}. $\mathbf{R}_C$ denotes the geometry optimised with an excess charge; $\mathbf{R}_N$ is the neutral optimised nuclear configuration. The overall effect is a slightly elongated buckyball in one direction.

	$L_{\mathrm{hex-pent}}$ [Å]	$L_{\mathrm{hex-hex}}$ [Å]
$\mathbf{R}_N$	1.452	1.398
$\mathbf{R}_C$	1.449	1.402

The SOMO of C_{60}^- is three-fold degenerate and it belongs to the T_{1u} irreducible representation of the I_h point group [119]. The Kohn–Sham calculations showed that the energy difference between the SOMO, LUMO and LUMO+1 is less than 10 meV. In the calculations, the 3-fold degeneracy of C_{60} was taken into account according to Ref. [123]. LUMO and LUMO+1 were also obtained from the SCF calculation and projected onto the p_π orbitals analogously to the SOMO. The root-mean-square average of the 9 possible H_{ab} values were calculated by coupling every possible orbital permutation. [123].

$$\mathrm{RMS}(H_{ab}) = \frac{1}{\sqrt{N}_{\{\phi\}}} \sqrt{\sum_{i,j\in\{\phi\}} H_{ij}^2} \qquad \{\phi\} = \{\mathrm{SOMO}, \mathrm{LUMO}, \mathrm{LUMO}+1\}. \quad (6.23)$$

6.4 Results & discussion

In order to assess the H_{ab} probability distribution, a large neighbour distance cut-off of 15 Å was chosen. At 300 K the distributions clearly show the difference between the second and first nearest neighbours. By integrating the peaks on the probability distribution plot Fig. 6.5 separately, the first sharp peak gives 0.333 corresponding to the six second nearest neighbours (at 14.01 Å) which were within the cut-off distance, and the rest gives 0.666 which corresponds to the twelve nearest neighbours. The average coupling for the nearest neighbours was $\langle H_{ab} \rangle_{1\text{st}} = 16.4$ meV with a maximum of $\max(H_{ab}) = 37.0$ meV . The second peak showed an average coupling of $\langle H_{ab} \rangle_{2\text{nd}} = 0.1$ meV. The H_{ab} values are so small for the second nearest neighbours that ignoring them does not affect the mobility values. The peak of the distribution for nearest neighbours is around 15.07 meV. While the average coupling from AOM is very close to the values obtained from FODFT by Oberhofer *et al.* (14 meV) the maximum value is only half of the maximum value with FODFT (68 meV in Ref [45]). This is due to the averaging over the degenerate states which was carried out for the AOM couplings but not for the FODFT couplings. As discussed previously in Chapters 4 and 5, the relative rotational orientation has a significant role in the magnitude of the coupling for π-conjugated systems. This is especially true for large molecules such as C_{60} which has a complex nodal structure (see Fig. 2.3). Due to this effect, the 9 possible coupling values are strongly anti-correlated by the orthogonality of the orbitals. If one orbital pair gives a very high coupling, some of the couplings due to the inclusion of orthogonal orbitals give a lower coupling, thereby reducing the mean coupling value. Therefore, the averaging has a very pronounced effect in evening out the coupling values. As a consequence, the peak representing the nearest neighbours is rather narrow (Fig. 6.5).

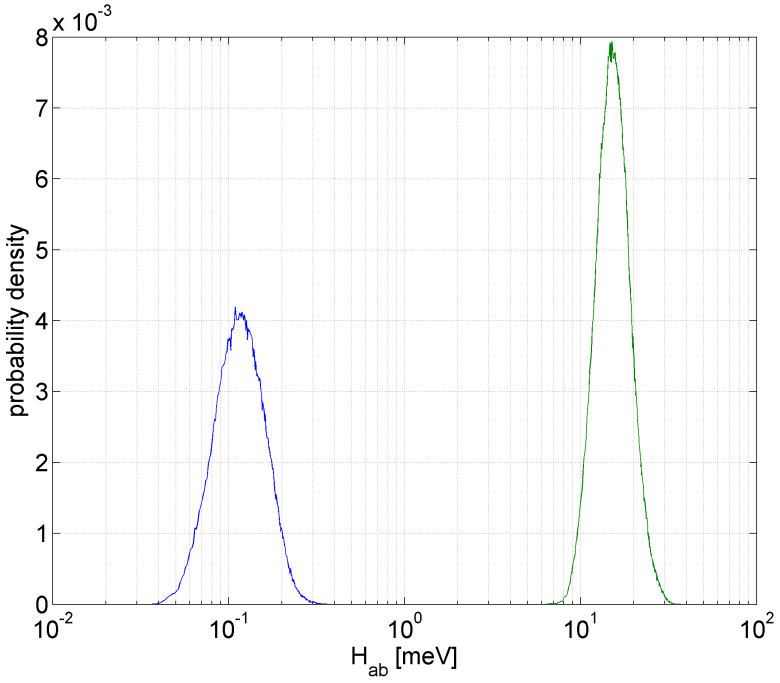

Figure 6.5: Distribution of the electronic coupling values for FCC C_{60} crystal at 300 K for a 1 ns trajectory. The neighbour distance cut-off was 15 Å including nearest and second nearest neighbours. The RMS averaging of the coupling values according to Eq. (6.23) resulted in relatively narrow peaks.

It is interesting to compare the effect of the dynamics on the coupling values as well. In Fig 6.6, the temperature dependency of the H_{ab} values can be seen along the different directions. It is known from experiment that crystalline C_{60} goes through phase transition at 255 K where the degree of rotational freedom reduces to two therefore the system is not completely isotropic anymore. This is reflected by the coupling distribution. At 500 K, the coupling distribution is very similar to the 300 K case: the maximum coupling was 36.4 meV, the mean was 16.63 meV while the maximum of the distribution was at 15 meV. Meanwhile at 100 K, the effect of the phase transition becomes obvious: the spread of the coupling values is wider ranging between 3.8 meV and 47.9 meV and the distribution is not smooth anymore. More importantly the anisotropy can be visualised by plotting the H_{ab} values along the lattice directions (Fig 6.6).

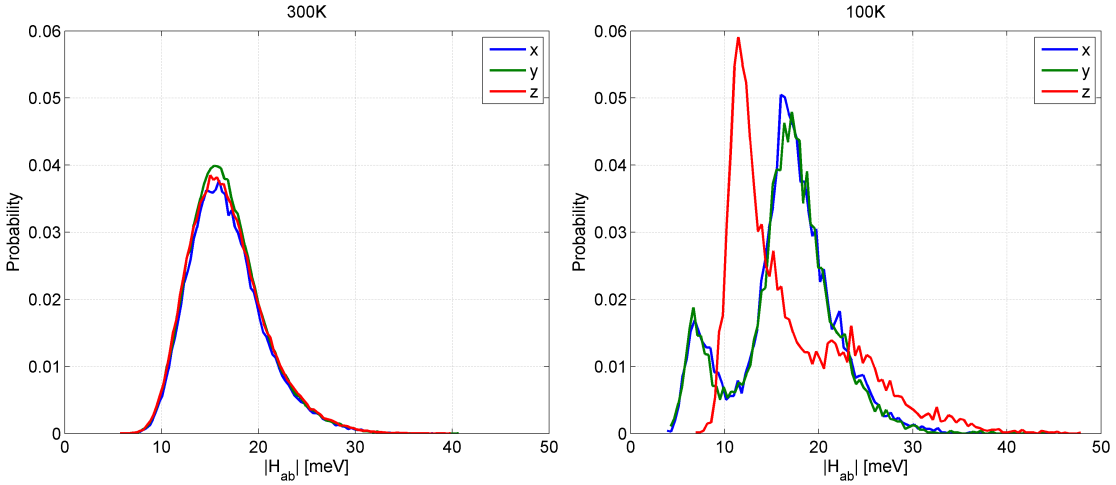

Figure 6.6: Distribution of the electronic coupling values for FCC C_{60} crystal at different temperatures for a 1 ns trajectory along the three axes for the nearest neighbours only. The 300 K trajectory on Panel A shows an isotropic distribution of coupling values while the 100 K trajectory has distinct peaks and in the z direction the distribution differs from the almost identical x and y directions. This is due to the phase transition in the crystalline C_{60} below 100K which prevents free rotation of the molecules. Such coupling distribution indicates that while at 300 K the mobility tensor is expected to be isotropic at 100 K this may not be true.

The inner-sphere contribution of the reorganisation energy λ_{i}, according to Eq. (6.5), was 105.33 meV and the outer-sphere contribution, according to Eq. (6.6), was around 38 meV. It is important to note that in this approximation the maximum H_{ab} value is 37 meV which although comparable to the reorganisation energy (143 meV) is less than 3/8 λ therefore the localised transport approximation does not break down in this case. This is due to the aforementioned smoothing effect of the RMS averaging. In fact, if the H_{ab} values are compared without averaging it can be seen that the maximum value goes up to 73 meV while the average value is 13 meV and the distribution can be approximated with half a Gaussian around 0 (Fig 6.7). This means that if averaging is not applied some of the coupling values are too high to assume localisation and the approximation breaks down.

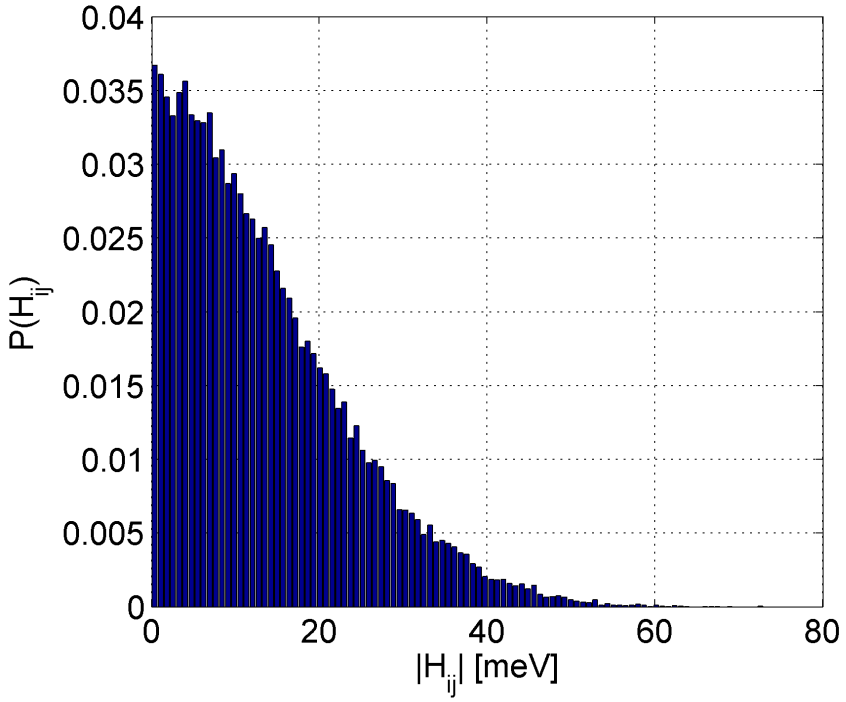

Figure 6.7: Distribution of the H_{ij} values in FCC C_{60} crystal at 300 K for a 100 ps trajectory when no RMS averaging is applied to the coupling values. The mean is 13 meV while the maximum coupling is 73 meV.

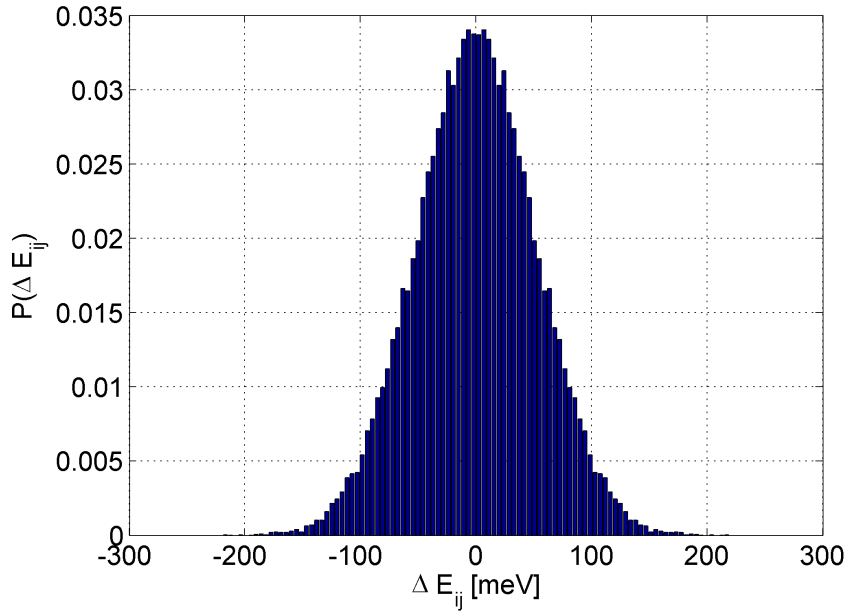

Figure 6.8: Distribution of the site energy difference for FCC C_{60} crystal at 300 K for a 100 ps trajectory. The energy peaks form a Gaussian with a mean of 0 meV and a standard deviation of 52.3 meV.

The site energy difference between the sites showed a Gaussian distribution with a mean of 0 and the standard deviation of 52.3 meV (Fig 6.8). The effective frequency obtained from the spectral density function according to Eq. (6.10) is 1624 cm^{-1}, this was obtained by using the vertical energy gap obtained for 100 ps long MD trajectory. The site energy differences are rather large compared to the H_{ab} values and are quite likely to dominate the Franck–Condon factor if the instantaneous values are used. This is elaborated in the next section where the different time scales are analysed.

6.4.1 Time scales

It was discussed how the different values on which the rates depend can be calculated. However, it is worth paying close attention to which values are averaged and which values are instantaneous in the formula. This can be achieved by comparing the time scales of the rate, the electronic coupling matrix elements, and the site energy difference. To this end, the Fourier transforms of the coupling values and ΔE_{ij} are compared to the distribution of rates in the system.

The Fourier transform of the H_{ab} values reveals that the change in the coupling values are dominated by low frequency components (Fig. 6.9). This is due to the importance of relative orientation for molecules with a complex nodal structure such as C_{60} therefore the change in coupling values is dominated by the rotation of the buckyballs.

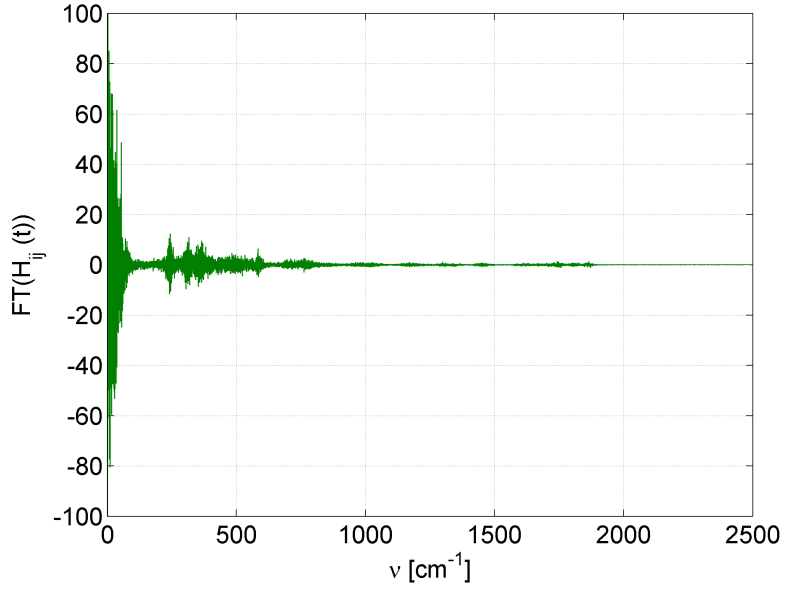

Figure 6.9: Discrete cosine transform of the electronic coupling for a dimer in a FCC C_{60} crystal at 300 K for a 100 ps trajectory. The spectrum is dominated by slowly changing parameters. This corresponds to our expectations that in the case of C_{60} the rotation has the most significant effect on the coupling.

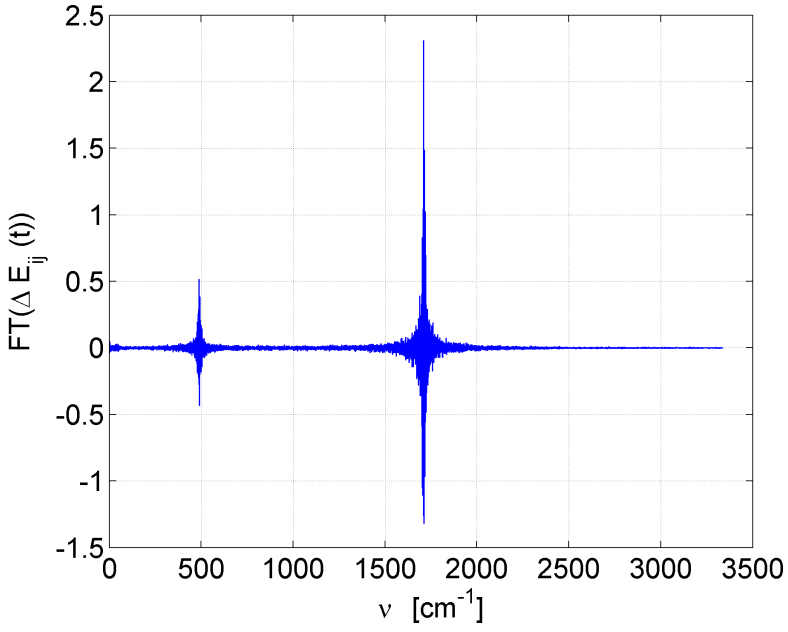

Figure 6.10: Discrete cosine transform of the site energy difference for a dimer in a FCC C_{60} crystal at 300 K for a 100 ps trajectory. The lower peak at 487 cm^{-1} corresponds to the breathing mode of the C_{60} cage. The higher frequency term is comparable to the frequency of a carbon double bond stretch.

As expected, the Fourier transform of the ΔE_{ij} values shows sharp peaks which are incidentally similar to those obtained for the spectral density function (Fig. 6.10). The sharp peak at 1710 cm^{-1} is comparable to the typical C=C stretch frequencies measured in IR spectroscopy. The lower peak at 487 cm^{-1} corresponds to the breathing mode in C_{60} [132].

The varied combined spectra of the H_{ab} values and the site energy difference poses the question of what kind of averaging should be used. The expected hopping rates for a given system are in the order of 1 to 10 THz. This does not include the range of the high frequency intramolecular term dominating ΔE_{ij}, but there is an expected overlap between the range of the fast changing components of the H_{ij} values and the rates.

In theory, one should average the high frequency components of the energy while keeping the low frequency components instantaneous. This would require an iterative Fourier transformation solution. However, it is expected that the averaged and not averaged mobilities do not give very different results therefore the rates are calculated with two algorithms. In the first version, the rate is calculated with the instantaneous coupling values and the averaged site energies $k = k(\Delta A_{ij}, H_{ab}, \mathbf{r})$. The kinetic Monte Carlo algorithm is run on all snapshots and the mobility is averaged over all configurations of the MD trajectory. In the second version, the site energy differences and electronic couplings are averaged over the trajectory. Then the averaged values are used for the calculation of a single set of hopping rates for which the mobility is obtained using KMC. In this case the rates are calculated as $k = k(\Delta A_{ij}, \langle H_{ab} \rangle, \langle \mathbf{r} \rangle)$. Hence, the two versions differ in the way the average over the configurations is taken. In addition, the rates are calculated with a third formula as well, in order to demonstrate how it affects the rates if the instantaneous energy values are used. In this case, the rates are calculated as $k = k(\Delta E_{ij}, H_{ab}, \mathbf{r})$.

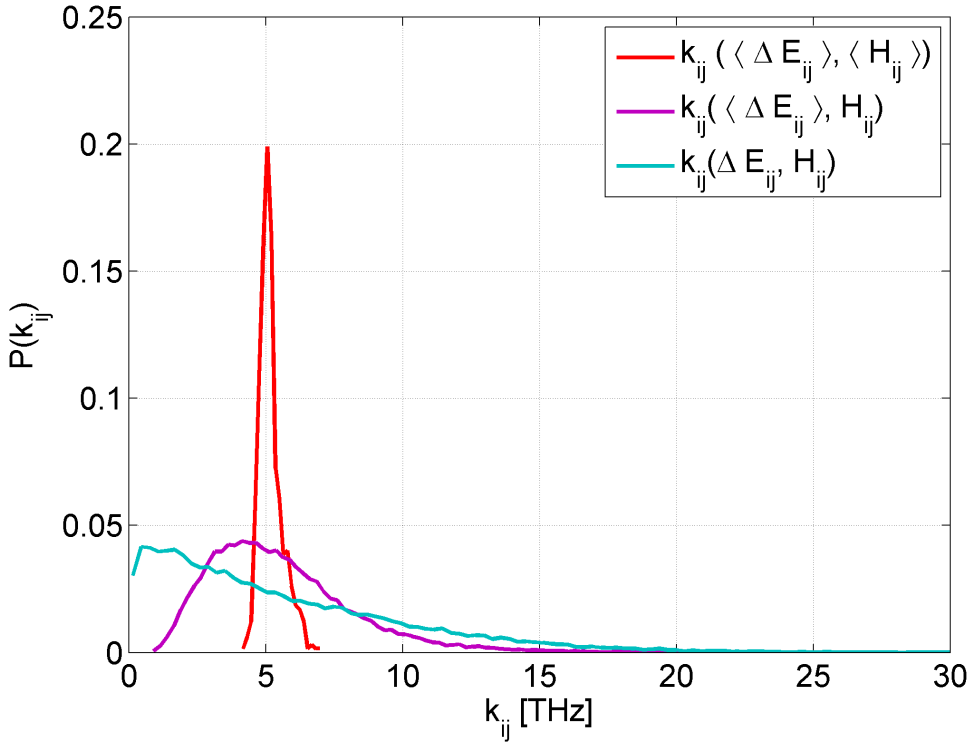

Figure 6.11: The probability distribution of the hopping rate with three different types of parameter averaging. As it can be seen the instantaneous site energy difference has a strong effect on the rate distribution, while the averaged H_{ab} values create a sharp rate distribution.

The instantaneous rates are strongly affected by the high frequency high amplitude ΔE_{ij} values (Fig. 6.11). However, the large fluctuations are due to the high frequency energy term which changes much faster than the hopping rate and it is right to assume that the averaged energy representation gives a more physical picture. Since the time evolution of the coupling values and the charge hopping seem to happen on the same time scale the mobility values are calculated with the rates according to $\langle k \rangle = k(\Delta A_{ij}, \langle H_{ij} \rangle)$ and $k = k(\Delta A_{ij}, H_{ij})$ (Fig. 6.12) and the mobilities with $\langle k \rangle = k(\Delta E_{ij}, H_{ij})$ are only calculated for 300 K.

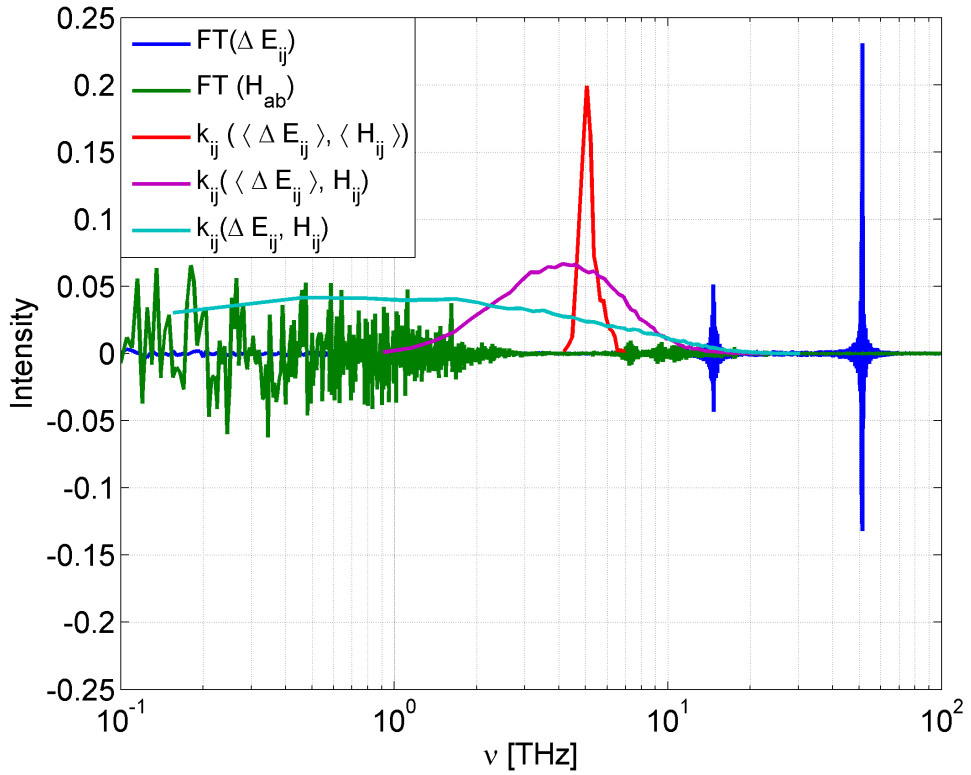

Figure 6.12: The probability distribution of the hopping rate compared to the Fourier transform of the site energy difference and the Fourier transform of the electronic coupling values. It can be seen that rates are in general slower than the site energy difference changes, while the difference is not so straightforward for the coupling timescales.

The mobility values calculated for the systems can be seen in Tables 6.2 and 6.3.

All eigenvalues of the mobility matrices were the same at high temperatures 300K and 500K. This is due to the free rotation of the molecules, hence the mobility is homogeneous. However, at 100 K the phase transition to non-free rotating crystal becomes obvious from the mobility values where in the z direction the mobility was less than half of that of x and y. This corresponds to the previously shown H_{ij} distribution in Fig. 6.6.

Table 6.2: Mobility values calculated with the different methods at different temperatures. μ_{ana} is calculated with the analytic evaluation method Eq. (6.16), μ_{E} is calculated with the Einstein relation Eq. (6.18), and μ_{nd} is calculated with the numerical derivative formula Eq. (6.22). At 300 K and 500 K the material was isotropic: all three mobility values were the same. All mobility values are in cm^2/Vs.

	$\langle k \rangle = k(\Delta A_{ij}, \langle H_{ij} \rangle)$		
T [K]	μ_{E}	μ_{ana}	μ_{nd}
300K	3.97	3.85	3.90
500K	2.66	2.69	2.74
	$k = k(\Delta A_{ij}, H_{ij})$		
	μ_{E}	μ_{ana}	μ_{nd}
300K	3.79	3.66	3.65
500K	2.57	2.56	2.46
	$k = k(\Delta E_{ij}, H_{ij})$		
	μ_{E}	μ_{ana}	μ_{nd}
300K	1.96	1.81	1.76

Table 6.3: Mobility values calculated with the different methods at 100 K. μ_{E} is calculated with the Einstein relation Eq. (6.18), and μ_{nd} is calculated with the numerical derivative formula Eq. (6.22). All mobility values are in cm^2/Vs.

	$\langle k \rangle = k(\Delta A_{ij}, \langle H_{ij} \rangle)$	
direction	μ_{E}	μ_{nd}
x	5.31	5.13
y	5.27	5.17
z	2.30	2.20
	$k = k(\Delta A_{ij}, H_{ij})$	
	μ_{E}	μ_{nd}
x	5.22	5.02
y	5.22	4.86
z	2.31	2.20

6.5 Conclusion

In this chapter, the analytic overlap method was used in combination with kinetic Monte Carlo simulations and molecular dynamics. It has been shown that the analytic overlap method can be used to calculate coupling matrix elements for large systems containing multiple dimers and that the method can be used to assess long trajectories on the timescale relevant to the dynamic disorder. It was also shown that

the mean of the electronic coupling values calculated for the molecular dynamics is very similar to that obtained by Oberhofer *et al.* using explicit electronic structure (FODFT) calculations [45] however the results seem to overestimate the experimental values obtained for FCC C_{60} of around $0.5(\pm 0.2)$ cm^2/Vs at room temperature [130]. In this approximation, the maximum of the coupling values remained small enough compared to the reorganisation energy that there was a finite energy barrier between the two states. However this is due to the smoothing effect of the averaged coupling values. Newton *et al.* recommends the root-mean-square averaging of couplings over degenerate orbitals for coupling values that are relatively similar. This was not an issue for the hemes in Ref. [79] where the coupling values between the monomers were similar but the range proved to be much broader in the C_{60} case. It is also important that if the averaging is not included, the coupling values occasionally become so large that the localised transport theory is not valid anymore. Therefore, C_{60} systems are better described by other methods where there is no assumptions of charge localisation and the degeneracy is included differently. For example, in the case of non-adiabatic molecular dynamics the degenerate states are part of the basis set of localised diabatic states. Using surface hopping on such a system would show that the charge does not remain on a single site but spreads over multiple sites and instead of discrete hops the excess charge would propagate in the system as a wave packet while the nuclear configuration switches from one potential energy surface to the other.

Nevertheless, the KMC study of the averaged coupling gives a good illustrative example of the importance of the dynamic effects and how they should be included in the rate calculation. Furthermore, the dynamic effects also gave an interesting example of how the temperature affects the isotropy of the mobility which gives an interesting tool to study other systems with different dynamic characteristics such as pentacene and rubrene.

7 Conclusion & Outlook

7.1 Conclusion

This work presented some of the main challenges of modelling charge transport in organic semiconductors. In Chapter 3, the most widely used models for discussing charge transport in organic semiconductors were presented including their shortcomings in assuming completely localised or delocalised charge carrier states. Then, two other models were shown which provide a more generic but computationally more intensive solution requiring the accurate and efficient calculation of the electronic coupling matrix elements, the overlap matrix, and the non-adiabatic coupling vector elements. The main focus of this work was to obtain these values to support charge transport modelling in organic semiconductors.

In order to understand the accuracy of the different methods in Chapter 4, various coupling calculation methods were compared for seven π-conjugated negatively charged molecules. The couplings were calculated between perfectly stacked dimers at different separation length. Another set was constructed with randomly oriented anthracene molecules. The reference calculations were performed using a high level *ab initio* SCS-CC2 method in combination with generalised Mulliken–Hush theory. Then the couplings were calculated with charge constrained density functional theory with different exchange correlation functionals, fragment orbital DFT, and fragment orbital density functional tight-binding. Of these methods, CDFT with 50% exact exchange had the smallest relative error compared to the reference values. Decreasing the proportion of exact exchange increased the errors significantly. Slightly faster than CDFT+PBE, FODFT+PBE also matched the reference values better as over-

delocalisation was prevented by the separation of dimers. HSE06 functional yielded very similar results to CDFT/25 (PBE0) therefore, there was no clear advantage of using range separated functional for these systems. FODFT results also had similar errors to CDFT/25. Although FODFTB was the fastest method, the errors were rather large compared to the reference values which is due to the limitations of the minimum basis set applied for these simulations. The relative error improved with all methods when a linear scaling factor was applied to the results. The results also showed that the methods are less accurate for the randomly oriented anthracenes than for the stacked system. This is due to the complicated nodal system of anthracene molecules.

Since CDFT with 50% exact exchange proved to be the best approach for both reduced and oxidised example molecules [68] it is expected to be transferable to other π-conjugated systems. Of the methods presented here only FODFTB is fast enough to be used in combination with non-adiabatic molecular dynamics but the errors are comparatively large which can cause issues in systems where the couplings fluctuate around values which suggest localised or delocalised transport. This motivated the development of an alternative method which not only provides the coupling matrix elements but also the overlap and the non-adiabatic coupling vectors.

The ultrafast and accurate semi-empirical analytic overlap method approximates the intermolecular electronic coupling between π-conjugated organic molecules as a linear function of the overlap between the SOMO of the donor and acceptor molecules. The approximation was tested in the range relevant to electron transport in the condensed phase (5 to 500 meV). It was also shown that a single proportionality constant is suitable to describe a broad set of molecules including arenes with heteroatoms, acenes and fullerenes. The accuracy also holds if the basis set is replaced with the minimum STO basis set with optimised Slater decay coefficients.

Furthermore, the analytic overlap method can be used to evaluate coupling values for rate equation based transport models. This was demonstrated on a set of heme

dimers. Here, the effect of molecular dynamics was also taken into account. In order to reduce computational demand, the contribution of the d-orbitals to the overlap values was neglected. The issue partly arose from the magnitude of the H_{ab} values as many of them were below the accuracy of 0.5 meV which was achievable with FODFT for these degenerate systems. More importantly, the issues came from the large fluctuations of the heme structures during molecular dynamics. In its current form, this model may not be best suited for charge transport modelling in biological systems where small couplings act as a bottleneck for the process.

The analytic overlap method can also be used to approximate the non-adiabatic coupling vector elements for π-conjugated systems. The method was benchmarked with FODFT on an ethylene dimer which showed that the NACV components pointing from one molecule to the other could be reproduced well with the AOM. Although the results were less accurate along the bonds, this is unlikely to cause issues as the nuclear forces arising from the off-diagonals of the Hamiltonian are two orders of magnitude smaller than the nuclear forces in the same direction. It is also expected that the absolute errors are smaller for any other π-conjugated system since the NACV elements are smaller in more extended systems.

The main benefit of the developed program is that it allows for an ultrafast estimation of off-diagonal elements. In fact, the speed-up with respect to DFT calculations is six orders of magnitude while the loss in accuracy compared to the benchmark values is within chemical accuracy. These results are very encouraging and set the stage for non-adiabatic molecular dynamics simulation of charge transfer in future work.

The analytic overlap method was also used in combination with kinetic Monte Carlo simulations and molecular dynamics. It was demonstrated that the analytic overlap method can be used to calculate coupling matrix elements for large systems containing multiple dimers and that the method can be used to assess long trajectories on the timescale relevant to the dynamic disorder in organic semiconductors.

In this approximation, the maximum of the coupling values remained small enough compared to the reorganisation energy that there was a finite energy barrier between the two states. However, this is due to the smoothing effect of the averaged coupling values. It is worth noting here that when the averaging is omitted, the AOM couplings obtained for the molecular dynamics trajectories give very similar statistics to the one reported by Oberhofer *et al.* using idealised C_{60} molecules and FODFT in Ref. [45]. This is in stark contrast with the heme values where the correlation between FODFT and AOM was poor. This is due to the fact that C_{60} is much more rigid than a heme and the idealised coefficients give a better approximation for the coupling values. As these non-averaged H_{ab} values are not all compatible with small polaron hopping theory, it is expected that non-adiabatic molecular dynamics gives better results for C_{60} mobilities as it does not assume charge localisation and the degeneracy is included differently. Nevertheless, the KMC study of the averaged coupling serves as an example of the importance of the dynamic effects in organic semiconductors and how the time scales of the hopping rate, the coupling values, and the energy difference affects the mobility. Furthermore, it was also discussed how the temperature affects the isotropy of the mobility, which makes it worthwhile to compare analysis done on other systems such as PCBM to C_{60} results.

7.2 Outlook

Based on the findings of this project there are a number of avenues of further research that can be explored. The series of benchmark calculations discussed charge transport with different methods in the reduced state. A follow-up project has been proposed which assesses donor-bridge-acceptor systems in order to better understand how well different methods can predict mediated charge transport. The first project of the series tackles small non-biological systems, with the eventual aim of building on this to understand the effects in biological systems such as amino acids and DNA

base pairs [109].

The analytic overlap and the non-adiabatic coupling vector calculation code was built partly to support non-adiabatic MD and the first results on a chain of ethylene molecules can be seen in the work of Spencer *et al.* [133]. The same method can be applied to actual organic semiconductor systems such as rubrene and pentacene. It was briefly mentioned in the conclusion section that in its current form the analytic overlap method is not suitable for analysing less rigid molecules such as heme cofactors. However, it is possible to adapt the code by defining a number of coefficient sets obtained for different molecular dynamics snapshots of hemes which form a sample coefficient set. Couplings of an independent molecular dynamics trajectory may be calculated by fitting the molecules to this set by minimising the root-mean-square deviation of the molecules and finding the most appropriate coefficient set to describe the given heme.

Even though the AOM model in its current form is useful for systems with large coupling values, the calculation of small coupling values below 5 meV remains a challenge. This was not unique to the AOM and similar trends were observed when other methods were compared to generalised Mulliken–Hush theory results. We found that with the AOM method the results can be improved for carbon atom and C_{60} results if different Slater coefficients are used for different p integrals depending on whether the alignment is π-type or σ-type, but the transferability of this approach was not tested. In order to be able to efficiently use the model in biological systems, the error value for small couplings has to be reduced. Furthermore, timeliness of the code can be improved further by parallelising the code.

The methods presented here are approximate and it would be very interesting to compare the non-adiabatic dynamics results with the work of Martinez *et al* who used shared memory CPU/GPU architecture to gain significant speed-up for TDDFT and DFT calculation and simulated non-adiabatic dynamics in a multiheme system [134].

Finally, it would also be interesting to compare the KMC results obtained for C_{60} with other non-free rotating molecules and how the different dynamic properties affect the time scales of the energy and the coupling values, as well as the isotropy.

Bibliography

[1] Mihai Irimia-Vladu. "Green" electronics: biodegradable and biocompatible materials and devices for sustainable future. *Chemical Society Reviews*, 43(2):588–610, 2014.

[2] Gerwin H Gelinck, H Edzer a Huitema, Erik van Veenendaal, Eugenio Cantatore, Laurens Schrijnemakers, Jan B P H van der Putten, Tom C T Geuns, Monique Beenhakkers, Jacobus B Giesbers, Bart-Hendrik Huisman, Eduard J Meijer, Estrella Mena Benito, Fred J Touwslager, Albert W Marsman, Bas J E van Rens, and Dago M de Leeuw. Flexible active-matrix displays and shift registers based on solution-processed organic transistors. *Nature materials*, 3(2):106–10, 2004.

[3] K Myny, S Steudel, S Smout, P Vicca, F Furthner, B. Van Der Putten, A. K. Tripathi, G. H. Gelinck, J Genoe, W. Dehaene, and P Heremans. Organic RFID transponder chip with data rate compatible with electronic product coding. *Organic Electronics: physics, materials, applications*, 11(7):1176–1179, 2010.

[4] M. Slawinski, M. Weingarten, M. Heuken, A. Vescan, and H. Kalisch. Investigation of large-area OLED devices with various grid geometries. *Organic Electronics: physics, materials, applications*, 14(10):2387–2391, 2013.

[5] Minze T. Rispens, Auke Meetsma, Roman Rittberger, Christoph J. Brabec, N. Serdar Sariciftci, and Jan C. Hummelen. Influence of the solvent on the crystal structure of PCBM. *Chemical Communications*, (17):2116, August 2003.

[6] A. Shah, J. Meier, A. Buechel, U. Kroll, J. Steinhauser, F. Meillaud, H. Schade, and D. Dominé. Towards very low-cost mass production of thin-film silicon

photovoltaic (PV) solar modules on glass. In *Thin Solid Films*, volume 502, pages 292–299, 2006.

[7] Giuseppe Paternò, Anna J. Warren, Jacob Spencer, Gwyndaf Evans, Victoria García Sakai, Jochen Blumberger, and Franco Cacialli. Micro-focused X-ray diffraction characterization of high-quality [6,6]-phenyl-C61-butyric acid methyl ester single crystals without solvent impurities. *Journal of Materials Chemistry C*, 1(36):5619, August 2013.

[8] Mengmeng Li, Cunbin An, Wojciech Pisula, and Klaus Müllen. Alignment of organic semiconductor microstripes by two-phase dip-coating. *Small*, 10(10):1926–1931, 2014.

[9] Nihat Tugluoglu, Behzad Baris, Hatice Gürel, Serdar Karadeniz, and Ömer Faruk Yüksel. Investigation of optical band gap and device parameters of rubrene thin film prepared using spin coating technique. *Journal of Alloys and Compounds*, 582:696–702, 2014.

[10] Anke Teichler, Jolke Perelaer, and Ulrich S. Schubert. Inkjet printing of organic electronics – comparison of deposition techniques and state-of-the-art developments. *Journal of Materials Chemistry C*, 1(10):1910, 2013.

[11] Jean-Luc Brédas, Joseph E Norton, Jérôme Cornil, and Veaceslav Coropceanu. Molecular understanding of organic solar cells: the challenges. *Accounts of chemical research*, 42(11):1691–9, November 2009.

[12] Bernard Kippelen and Jean-Luc Brédas. Organic photovoltaics. *Energy & Environmental Science*, 2(3):251, March 2009.

[13] Yongbo Yuan, Gaurav Giri, Alexander L. Ayzner, Arjan P. Zoombelt, Stefan C. B. Mannsfeld, Jihua Chen, Dennis Nordlund, Michael F. Toney, Jinsong Huang, and Zhenan Bao. Ultra-high mobility transparent organic thin film

transistors grown by an off-centre spin-coating method. *Nature communications*, 5:3005, January 2014.

[14] Nichole C. Cates, Roman Gysel, Zach Beiley, Chad E. Miller, Michael F. Toney, Martin Heeney, Lain McCulloch, and Michael D. McGehee. Tuning the properties of polymer bulk heterojunction solar cells by adjusting fullerene size to control intercalation. *Nano Letters*, 9(12):4153–4157, December 2009.

[15] Minh Trung Dang, Guillaume Wantz, Habiba Bejbouji, Mathieu Urien, Olivier J. Dautel, Laurence Vignau, and Lionel Hirsch. Polymeric solar cells based on P3HT:PCBM: Role of the casting solvent. *Solar Energy Materials and Solar Cells*, 95(12):3408–3418, 2011.

[16] Y N Li, Prashant Sonar, Leanne Murphy, and Wei Hong. High mobility diketopyrrolopyrrole (DPP)-based organic semiconductor materials for organic thin film transistors and photovoltaics. *Energy & Environmental Science*, 6(6):1684–1710, 2013.

[17] Wei Xie, Kathryn A. McGarry, Feilong Liu, Yanfei Wu, P. Paul Ruden, Christopher J. Douglas, and C. Daniel Frisbie. High-mobility transistors based on single crystals of isotopically substituted rubrene-d28. *Journal of Physical Chemistry C*, 117(22):11522–11529, June 2013.

[18] Ke Zhou, Huanli Dong, Hao-Li Zhang, and Wenping Hu. High performance n-type and ambipolar small organic semiconductors for organic thin film transistors. *Physical Chemistry Chemical Physics*, 16(41):22448–57, 2014.

[19] Tao Liu and Alessandro Troisi. Understanding the Microscopic Origin of the Very High Charge Mobility in PBTTT: Tolerance of Thermal Disorder. *Advanced Functional Materials*, 24(7):925–933, September 2013.

[20] Jui-Fen Chang, Tomo Sakanoue, Yoann Olivier, Takafumi Uemura, Marie-Beatrice Dufourg-Madec, Stephen G. Yeates, Jérôme Cornil, Jun Takeya,

Alessandro Troisi, and Henning Sirringhaus. Hall-Effect Measurements Probing the Degree of Charge-Carrier Delocalization in Solution-Processed Crystalline Molecular Semiconductors. *Physical Review Letters*, 107(6):066601, August 2011.

[21] Paul A. Heiney. Structure, dynamics and ordering transition of solid C60. *Journal of Physics and Chemistry of Solids*, 53(11):1333–1352, 1992.

[22] Thorsten Vehoff, Alessandro Troisi, and Denis Andrienko. Charge Transport in Organic Crystals : Role of Disorder and Topological Connectivity. *Journal of Physical Chemistry C*, 118(8):11702–11708, 2010.

[23] Tao Liu and Alessandro Troisi. What makes fullerene acceptors special as electron acceptors in organic solar cells and how to replace them. *Advanced Materials*, 25(7):1038–1041, February 2013.

[24] C.W. Chang, B.C. Regan, W. Mickelson, R.O. Ritchie, and A. Zettl. Probing structural phase transitions of crystalline C60 via resistivity measurements of metal film overlayers. *Solid State Communications*, 128(9-10):359–363, December 2003.

[25] Lidong Zheng and Yanchun Han. Solvated crystals based on [6,6]-phenyl-C61-butyric acid methyl ester (PCBM) with the hexagonal structure and their phase transformation. *Journal of Physical Chemistry B*, 116(5):1598–1604, February 2012.

[26] Alessandro Troisi. Charge transport in high mobility molecular semiconductors: classical models and new theories. *Chemical Society reviews*, 40(5):2347–58, May 2011.

[27] V. Podzorov, E. Menard, J. a. Rogers, and M. E. Gershenson. Hall effect in the accumulation layers on the surface of organic semiconductors. *Physical Review Letters*, 95(22):226601, November 2005.

[28] Kazuhiro Marumoto, Shin Ichi Kuroda, Taishi Takenobu, and Yoshihiro Iwasa. Spatial extent of wave functions of gate-induced hole carriers in pentacene field-effect devices as investigated by electron spin resonance. *Physical Review Letters*, 97(25):256603, December 2006.

[29] S. Fratini and S. Ciuchi. Bandlike motion and mobility saturation in organic molecular semiconductors. *Physical Review Letters*, 103(26):266601, December 2009.

[30] Joe J. Kwiatkowski, Jarvist M. Frost, and Jenny Nelson. The effect of morphology on electron field-effect mobility in disordered C60 thin films. *Nano Letters*, 9(3):1085–1090, 2009.

[31] Rocco P Fornari and Alessandro Troisi. Theory of charge hopping along a disordered polymer chain. *Physical Chemistry Chemical Physics*, 16(21):9997–10007, January 2014.

[32] T Holstein. Studies of polaron motion. *Annals of Physics*, 8(3):325–342, November 1959.

[33] Alessandro Troisi. Quantum dynamic localization in the Holstein Hamiltonian at finite temperatures. *Physical Review B - Condensed Matter and Materials Physics*, 82(24):245202, December 2010.

[34] Roel S. Sanchez-Carrera, Pavel Paramonov, Graeme M. Day, Veaceslav Coropceanu, and Jean Luc Bredas. Interaction of charge carriers with lattice vibrations in oligoacene crystals from naphthalene to pentacene. *Journal of the American Chemical Society*, 132(41):14437–14446, October 2010.

[35] Henning Sirringhaus, Tomo Sakanoue, and Jui Fen Chang. Charge-transport physics of high-mobility molecular semiconductors. *Physica Status Solidi (B) Basic Research*, 249(9):1655–1676, 2012.

[36] Veaceslav Coropceanu, Jérôme Cornil, Demetrio a. da Silva Filho, Yoann Olivier, Robert Silbey, and Jean Luc Brédas. Charge transport in organic semiconductors. *Chemical Reviews*, 107(4):926–952, April 2007.

[37] Charles Kittel. *Introduction to solid state physics*. John Wiley & Sons, 7 edition, 2005.

[38] Neil W Ashcroft and N David Mermin. *Solid State Physics*, volume 2. Harcourt College Publisher, 1976.

[39] N. Karl. Charge carrier transport in organic semiconductors. In *Synthetic Metals*, volume 133-134, pages 649–657, 2003.

[40] Tomo Sakanoue and Henning Sirringhaus. Band-like temperature dependence of mobility in a solution-processed organic semiconductor. *Nature materials*, 9(9):736–40, September 2010.

[41] Jochen Blumberger. Recent Advances in the Theory and Molecular Simulation of Biological Electron Transfer Reactions. *Chemical Reviews*, 115(20):11191–11238, October 2015.

[42] R. A. Marcus. On the Theory of Oxidation-Reduction Reactions Involving Electron Transfer. I. *The Journal of Chemical Physics*, 24(5):966, December 1956.

[43] T. Holstein. Studies of Polaron Motion Part II. The "Small" Polaron. *Annals of Physics*, 281(1-2):725–773, April 2000.

[44] Abraham Nitzan. *Chemical Dynamics in Condensed Phases: Relaxation, Transfer, and Reactions in Condensed Molecular Systems (Oxford Graduate Texts)*, volume 8. Oxford University Press, 2006.

[45] Harald Oberhofer and Jochen Blumberger. Revisiting electronic couplings and incoherent hopping models for electron transport in crystalline C60 at ambient

temperatures. *Physical Chemistry Chemical Physics*, 14(40):13846, October 2012.

[46] Jenny Nelson, Joe J. Kwiatkowski, James Kirkpatrick, and Jarvist M. Frost. Modeling charge transport in organic photovoltaic materials. *Accounts of Chemical Research*, 42(11):1768–1778, 2009.

[47] Alessandro Troisi. The speed limit for sequential charge hopping in molecular materials. *Organic Electronics: physics, materials, applications*, 12(12):1988–1991, December 2011.

[48] David L. Cheung and Alessandro Troisi. Theoretical study of the organic photovoltaic electron acceptor PCBM : morphology, electronic structure, and charge localization. *The Journal of Physical Chemistry C*, 114(48):20479–20488, December 2010.

[49] Fruzsina Gajdos, Harald Oberhofer, Michel Dupuis, and Jochen Blumberger. On the inapplicability of electron-hopping models for the organic semiconductor phenyl-C61-butyric acid methyl ester (PCBM). *Journal of Physical Chemistry Letters*, 4(6):1012–1017, March 2013.

[50] Lionel Friedman. Electron-phonon interaction in organic molecular crystals. *Physical Review*, 140(5A), 1965.

[51] K. Hannewald, V. M. Stojanović, J. M. T. Schellekens, P. a. Bobbert, G. Kresse, and J. Hafner. Theory of polaron bandwidth narrowing in organic molecular crystals. *Physical Review B*, 69(7):075211, February 2004.

[52] E. Mozafari and S. Stafstrom. Polaron dynamics in a two-dimensional Holstein-Peierls system. *Journal of Chemical Physics*, 138(18):0–7, 2013.

[53] John C. Tully. Mixed quantum-classical dynamics. *Faraday Discussions*, 110(0):407–419, January 1998.

[54] Priya V. Parandekar and John C. Tully. Mixed quantum-classical equilibrium. *Journal of Chemical Physics*, 122(9):094102, March 2005.

[55] Linjun Wang and David Beljonne. Flexible surface hopping approach to model the crossover from hopping to band-like transport in organic crystals. *Journal of Physical Chemistry Letters*, 4(11):1888–1894, June 2013.

[56] Adam Kubas, Fruzsina Gajdos, Alexander Heck, Harald Oberhofer, Marcus Elstner, and Jochen Blumberger. Electronic couplings for molecular charge transfer: benchmarking CDFT, FODFT and FODFTB against high-level ab initio calculations. II. *Physical Chemistry Chemical Physics*, 17(22):14342–14354, 2015.

[57] Seth Difley and Troy Van Voorhis. Exciton/charge-transfer electronic couplings in organic semiconductors. *Journal of Chemical Theory and Computation*, 7(3):594–601, 2011.

[58] Troy Van Voorhis, Tim Kowalczyk, Benjamin Kaduk, Lee-Ping Wang, Chiao-Lun Cheng, and Qin Wu. The diabatic picture of electron transfer, reaction barriers, and molecular dynamics. *Annual review of physical chemistry*, 61:149–70, January 2010.

[59] Robert S. Mulliken. Molecular compounds and their spectra. II. *Journal of the American Chemical Society*, 74(8):811–824, 1952.

[60] Noel S. Hush. Intervalence-Transfer Absorption. Theoretical Considerations and Spectroscopic Data. *Progress in Inorganic Chemistry*, 8:391–444, 1967.

[61] Noel S. Hush. Homogeneous and heterogeneous optical and thermal electron transfer. *Electrochimica Acta*, 13(5):1005–1023, 1968.

[62] Carol Creutz, Marshall D. Newton, and Norman Sutin. Metal-lingad and

metal-metal coupling elements. *Journal of Photochemistry and Photobiology, A: Chemistry*, 82(1-3):47–59, 1994.

[63] R. J. Cave and M. D. Newton. Generalization of the Mulliken-Hush treatment for the calculation of electron transfer matrix elements. *Chemical Physics Letters*, 249(1-2):15–19, January 1996.

[64] Robert J. Cave and Marshall D. Newton. Calculation of electronic coupling matrix elements for ground and excited state electron transfer reactions: Comparison of the generalized Mulliken–Hush and block diagonalization methods. *The Journal of Chemical Physics*, 106(22):9213, 1997.

[65] Peter G. Szalay, Thomas Muller, Gergely Gidofalvi, Hans Lischka, and Ron Shepard. Multiconfiguration self-consistent field and multireference configuration interaction methods and applications. *Chemical Reviews*, 112(1):108–181, January 2012.

[66] C. Angeli, R. Cimiraglia, S. Evangelisti, T. Leininger, and J. P. Malrieu. Introduction of n-electron valence states for multireference perturbation theory. *Journal of Chemical Physics*, 114(23):10252, 2001.

[67] Celestino Angeli, Renzo Cimiraglia, and Jean Paul Malrieu. n-electron valence state perturbation theory: A spinless formulation and an efficient implementation of the strongly contracted and of the partially contracted variants. *Journal of Chemical Physics*, 117(20):9138–9153, 2002.

[68] Adam Kubas, Felix Hoffmann, Alexander Heck, Harald Oberhofer, Marcus Elstner, and Jochen Blumberger. Electronic couplings for molecular charge transfer: Benchmarking CDFT, FODFT, and FODFTB against high-level ab initio calculations. *Journal of Chemical Physics*, 140(10):1–46, December 2014.

[69] Joseph E. Subotnik, Sina Yeganeh, Robert J. Cave, and Mark a. Ratner. Constructing diabatic states from adiabatic states: Extending generalized

Mulliken-Hush to multiple charge centers with Boys localization. *Journal of Chemical Physics*, 129(24):244101, December 2008.

[70] Jieru Zheng, Youn K Kang, Michael J Therien, and David N Beratan. Generalized Mulliken-Hush analysis of electronic coupling interactions in compressed pi-stacked porphyrin-bridge-quinone systems. *Journal of the American Chemical Society*, 127(32):11303–11310, August 2005.

[71] Christoph Lambert, Gilbert Nöll, and Jürgen Schelter. Bridge-mediated hopping or superexchange electron-transfer processes in bis(triarylamine) systems. *Nature materials*, 1(1):69–73, September 2002.

[72] Qin Wu and Troy Van Voorhis. Extracting electron transfer coupling elements from constrained density functional theory. *Journal of Chemical Physics*, 125(16):164105, October 2006.

[73] F. L. Hirshfeld. Bonded-atom fragments for describing molecular charge densities. *Theoretica Chimica Acta*, 44(2):129–138, 1977.

[74] Harald Oberhofer and Jochen Blumberger. Electronic coupling matrix elements from charge constrained density functional theory calculations using a plane wave basis set. *Journal of Chemical Physics*, 133(24):244105, December 2010.

[75] Jan Rezac, Bernard Lévy, Isabelle Demachy, and Aurélien De La Lande. Robust and efficient constrained DFT molecular dynamics approach for biochemical modeling. *Journal of Chemical Theory and Computation*, 8(2):418–427, 2012.

[76] Keith P. McKenna and Jochen Blumberger. Crossover from incoherent to coherent electron tunneling between defects in MgO. *Physical Review B*, 86(24):245110, December 2012.

[77] Jochen Blumberger and Keith P. McKenna. Constrained density functional theory applied to electron tunnelling between defects in MgO. *Physical Chemistry Chemical Physics*, 15(1):2184–96, 2013.

[78] Harald Oberhofer and Jochen Blumberger. Insight into the mechanism of the ru2+-ru3+ electron self-exchange reaction from quantitative rate calculations. *Angewandte Chemie - International Edition*, 49(21):3631–3634, May 2010.

[79] Marian Breuer, Kevin M Rosso, and Jochen Blumberger. Electron flow in multiheme bacterial cytochromes is a balancing act between heme electronic interaction and redox potentials. *Proceedings of the National Academy of Sciences of the United States of America*, 111(2):611–6, January 2014.

[80] Marian Breuer, Kevin M. Rosso, and Jochen Blumberger. Flavin Binding to the Deca-heme Cytochrome MtrC: Insights from Computational Molecular Simulation. *Biophysical Journal*, 109(12):2614–2624, December 2015.

[81] M. Elstner, D. Porezag, G. Jungnickel, J. Elsner, M. Haugk, Th. Frauenheim, S. Suhai, and G. Seifert. Self-consistent-charge density-functional tight-binding method for simulations of complex materials properties. *Physical Review B*, 58(11):7260–7268, September 1998.

[82] Michael Gaus, Qiang Cui, and Marcus Elstner. DFTB3: Extension of the self-consistent-charge density-functional tight-binding method (SCC-DFTB). *Journal of Chemical Theory and Computation*, 7(4):931–948, April 2011.

[83] Pekka Koskinen and Ville Mäkinen. Density-functional tight-binding for beginners. *Computational Materials Science*, 47(1):237–253, 2009.

[84] Michael Gaus, Albrecht Goez, and Marcus Elstner. Parametrization and benchmark of DFTB3 for organic molecules. *Journal of Chemical Theory and Computation*, 9(1):338–354, January 2013.

[85] Tomás Kubar, P Benjamin Woiczikowski, Gianaurelio Cuniberti, and Marcus Elstner. Efficient calculation of charge-transfer matrix elements for hole transfer in DNA. *Journal of Physical Chemistry B*, 112(26):7937–47, July 2008.

[86] Alexander Heck, Paul Benjamin Woiczikowski, Tomas Kubar, Kai Welke, Thomas Niehaus, Bernd Giese, Spiros Skourtis, Marcus Elstner, and Thomas B. Steinbrecher. Fragment orbital based description of charge transfer in peptides including backbone orbitals. *Journal of Physical Chemistry B*, 118(16):4261–4272, 2014.

[87] Mario Wolter, Marcus Elstner, and Tomas Kubar. Charge transport in desolvated DNA. *Journal of Chemical Physics*, 139(12), 2013.

[88] Paul Benjamin Woiczikowski, Thomas Steinbrecher, Tomas Kubar, and Marcus Elstner. Nonadiabatic QM/MM simulations of fast charge transfer in Escherichia coli DNA photolyase. *Journal of Physical Chemistry B*, 115(32):9846–9863, 2011.

[89] John P. Perdew, Kieron Burke, and Matthias Ernzerhof. Generalized Gradient Approximation Made Simple. *Physical Review Letters*, 77(18):3865–3868, October 1996.

[90] D E Woon and T H Dunning. Gaussian-Basis Sets for Use in Correlated Molecular Calculations III. the Atoms Aluminum Through Argon. *Journal of Chemical Physics*, 98(2):1358–1371, 1993.

[91] Timothy J. Lee and Peter R. Taylor. A diagnostic for determining the quality of single-reference electron correlation methods. *International Journal of Quantum Chemistry*, 36(S23):199–207, June 2009.

[92] John P. Perdew. Density-functional approximation for the correlation energy of the inhomogeneous electron gas. *Physical Review B*, 33(12):8822–8824, 1986.

[93] A. D. Becke. Density-functional exchange-energy approximation with correct asymptotic behavior. *Physical Review A*, 38(6):3098–3100, 1988.

[94] K Eichkorn, F Weigend, O Treutler, and Reinhart Ahlrichs. Auxiliary basis sets for main row atoms and transition metals and their use to approximate Coulomb potentials. *Theoretical Chemistry Accounts*, 97(1-4):119–124, 1997.

[95] Florian Weigend and Reinhart Ahlrichs. Balanced basis sets of split valence, triple zeta valence and quadruple zeta valence quality for H to Rn: Design and assessment of accuracy. *Physical Chemistry Chemical Physics*, 7(18):3297–305, 2005.

[96] Karin Eichkorn, Oliver Treutler, Holger Ohm, Marco Haser, and Reinhart Ahlrichs. Auxiliary basis sets to approximate Coulomb potentials. *Chemical Physics Letters*, 240(4):283–289, 1995.

[97] Marek Sierka, Annika Hogekamp, and Reinhart Ahlrichs. Fast evaluation of the Coulomb potential for electron densities using multipole accelerated resolution of identity approximation. *Journal of Chemical Physics*, 118(20):9136–9148, 2003.

[98] R Ahlrichs, S Bäcker, M Ehrig, K Eichkorn, S Elliott, F Haase, M Hoser, H Horn, C Huber, U Huniar, M Kattannek, C Kolmel, M Kollwitz, C Ochsenfeld, H Öhm, A Schäfer, U Schneider, O Treutler, M von Arnim, F Weigend, P Weis, and H Weiss. TURBOMOLE V6.2 2010, a development of University of Karlsruhe and Forschungszentrum Karlsruhe GmbH, 1989-2007, TURBOMOLE GmbH, since 2007; available from http://www.turbomole.com., 2008.

[99] Ove Christiansen, Henrik Koch, and Poul Jorgensen. The second-order approximate coupled cluster singles and doubles model CC2. *Chemical Physics Letters*, 243(5-6):409–418, 1995.

[100] Arnim Hellweg, Sarah a Grün, and Christof Hättig. Benchmarking the performance of spin-component scaled CC2 in ground and electronically excited states. *Physical Chemistry Chemical Physics*, 10(28):4119–4127, 2008.

[101] Jonathan C. Rienstra-Kiracofe, Wesley D. Allen, and Henry F. Schaefer. C2H5+O2 reaction mechanism: High-level ab initio characterizations. *Journal of Physical Chemistry A*, 104(44):9823–9840, 2000.

[102] Stefan Grimme. Improved second-order Møller-Plesset perturbation theory by separate scaling of parallel- and antiparallel-spin pair correlation energies. *Journal of Chemical Physics*, 118(20):9095–9102, 2003.

[103] Florian Weigend, Andreas Kohn, and Christof Hattig. Efficient use of the correlation consistent basis sets in resolution of the identity MP2 calculations. *Journal of Chemical Physics*, 116(8):3175–3183, 2002.

[104] Thom H Dunning Jr. Gaussian basis sets for use in correlated molecular calculations. I. The atoms boron through neon and hydrogen. *Journal of Chemical Physics*, 90(1989):1007, 1989.

[105] Jürg Hutter and Marcella Iannuzzi. CPMD: Car-parrinello molecular dynamics. *Zeitschrift fur Kristallographie*, 220(5-6):549–551, 2005.

[106] N. Troullier and Jose Luriaas Martins. Efficient pseudopotentials for plane-wave calculations. II. Operators for fast iterative diagonalization. *Physical Review B*, 43(11):8861–8869, 1991.

[107] Mark E Tuckerman and Glenn J Martyna. Understanding Modern Molecular Dynamics: Techniques and Applications. *The Journal of Physical Chemistry B*, 104(2):159–178, 2000.

[108] Tomas Kubar, Zoltan Bodrog, Michael Gaus, Christof Köhler, Balint Aradi, Thomas Frauenheim, and Marcus Elstner. Parametrization of the SCC-

DFTB method for halogens. *Journal of Chemical Theory and Computation*, 9(7):2939–2949, 2013.

[109] N. Gillet, L. Berstis, X. Wu, F. Gajdos, A. Heck, A. de la Lande, J Blumberger, and M. Elstner. Electronic Coupling Calculations for Bridge-Mediated Charge Transfer Using CDFT and Effective Hamiltonian approaches at DFT and FODFTB level. *Journal of Chemical Theory and Computation*, 12(10):4793–4805, 2016.

[110] Roald Hoffmann. An Extended Hueckel Theory. I. Hydrocarbons. *The Journal of Chemical Physics*, 39(6):1397, June 1963.

[111] Alessandro Troisi and Giorgio Orlandi. Hole migration in DNA: A theoretical analysis of the role of structural fluctuations. *Journal of Physical Chemistry B*, 106(8):2093–2101, February 2002.

[112] James Kirkpatrick. An approximate method for calculating transfer integrals based on the ZINDO Hamiltonian. *International Journal of Quantum Chemistry*, 108(1):51–56, 2008.

[113] R S Mulliken, C a Rieke, D Orloff, and H Orloff. Formulas and numerical tables for overlap integrals. *Journal of Chemical Physics*, 17(12):1248–1267, December 1949.

[114] Fruzsina Gajdos, Siim Valner, Felix Hoffmann, Jacob Spencer, Marian Breuer, Adam Kubas, Michel Dupuis, and Jochen Blumberger. Ultrafast Estimation of Electronic Couplings for Electron Transfer between π-Conjugated Organic Molecules. *Journal of Chemical Theory and Computation*, 10(10):4653–4660, October 2014.

[115] Aurélien de la Lande and Dennis R. Salahub. Derivation of interpretative models for long range electron transfer from constrained density functional theory. *Journal of Molecular Structure: THEOCHEM*, 943(1):115–120, 2010.

[116] Harald Oberhofer and Jochen Blumberger. Charge constrained density functional molecular dynamics for simulation of condensed phase electron transfer reactions. *The Journal of chemical physics*, 131(6):064101, August 2009.

[117] J. Slater. Atomic Shielding Constants. *Physical Review*, 36(1):57–64, July 1930.

[118] E. Clementi and D. L. Raimondi. Atomic Screening Constants from SCF Functions. *The Journal of Chemical Physics*, 38(11):2686, 1963.

[119] Shachar Klaiman, Evgeniy V. Gromov, and Lorenz S. Cederbaum. Extreme Correlation Effects in the Elusive bound spectrum of C60-. *Journal of Physical Chemistry Letters*, 4(19):3319–3324, 2013.

[120] Roderick C I Mackenzie, Jarvist M Frost, and Jenny Nelson. A numerical study of mobility in thin films of fullerene derivatives. *Journal of Chemical Physics*, 132(6):64904, February 2010.

[121] N L Costa, H K Carlson, J D Coates, R O Louro, and C M Paquete. Heterologous expression and purification of a multiheme cytochrome from a Gram-positive bacterium capable of performing extracellular respiration. *Protein Expression and Purification*, 111:48–52, July 2015.

[122] Xiuyun Jiang and Jochen Blumberger. Electron flow in small tetraheme cytchrome. *paper in preparation.*

[123] Marshall D Newton. Quantum chemical probes of electron-transfer kinetics: the nature of donor-acceptor interactions. *Chemical Reviews*, 91(5):767–792, 1991.

[124] Marcus Lundberg, Yoko Sasakura, Guishan Zheng, and Keiji Morokuma. Case studies of ONIOM(DFT:DFTB) and ONIOM(DFT:DFTB:MM) for enzymes

and enzyme mimics. *Journal of Chemical Theory and Computation*, 6(4):1413–1427, April 2010.

[125] Arthur Voter. *Radiation Effects in Solids*, volume 235 of *NATO Science Series*. Springer Netherlands, Dordrecht, 2007.

[126] A.B. Bortz, M.H. Kalos, and J.L. Lebowitz. A new algorithm for Monte Carlo simulation of Ising spin systems. *Journal of Chemical Physics Physics*, 17(1):10–18, January 1975.

[127] A. F. Hebard, R. C. Haddon, R. M. Fleming, and A. R. Kortan. Deposition and characterization of fullerene films. *Applied Physics Letters*, 59(17):2109, October 1991.

[128] Jeffrey S. Meth, Herman Vanherzeele, and Ying Wang. Dispersion of the third-order optical nonlinearity of C60. A third-harmonic generation study. *Chemical Physics Letters*, 197(1-2):26–31, September 1992.

[129] Arleh Warshel. Dynamics of Reactions in Polar Solvents. Semiclassical Trajectory Studies of Electron-Transfer and Proton-Transfer Reactions. *J. Phys. Chem*, 86:2218–2224, 1982.

[130] E. Frankevich, Y. Maruyama, and H. Ogata. Mobility of charge carriers in vapor-phase grown C60 single crystal. *Chemical Physics Letters*, 214(1):39–44, October 1993.

[131] I-Chun Lin, Maurício Coutinho-Neto, Camille Felsenheimer, O. von Lilienfeld, Ivano Tavernelli, and Ursula Rothlisberger. Library of dispersion-corrected atom-centered potentials for generalized gradient approximation functionals: Elements H, C, N, O, He, Ne, Ar, and Kr. *Physical Review B*, 75(20):205131, May 2007.

[132] Julien Idé, Daniele Fazzi, Mosè Casalegno, Stefano Valdo Meille, and Guido Raos. Electron transport in crystalline PCBM-like fullerene derivatives: a comparative computational study. *Journal of Materials Chemistry C*, 2(35):7313–7325, June 2014.

[133] J. Spencer, F. Gajdos, and J. Blumberger. FOB-SH: Fragment orbital-based surface hopping for charge carrier transport in organic and biological molecules and materials. *The Journal of Chemical Physics*, 145(6):064102, August 2016.

[134] Aaron Sisto, David R. Glowacki, and Todd J. Martinez. Ab initio nonadiabatic dynamics of multichromophore complexes: A scalable graphical-processing-unit-accelerated exciton framework. *Accounts of Chemical Research*, 47(9):2857–2866, 2014.